

High-order harmonic generation with ultra-short pulses from filamentation

Von der Fakultät für Mathematik und Physik
der Gottfried Wilhelm Leibniz Universität Hannover
zur Erlangung des Grades

Doktor der Naturwissenschaften
- Dr. rer. nat. -

genehmigte Dissertation

von
Dipl.-Phys. Daniel Sebastian Steingrube
geboren am 27.06.1982 in Göttingen

2011

Referent: Prof. Dr. U. Morgner
Korreferent: Prof. Dr. M. Lein
Tag der Promotion: 17.06.2011

Kurzfassung

Daniel S. Steingrube

Erzeugung hoher harmonischer Strahlung mit ultrakurzen Pulsen aus einem Filament

Die Messung ultraschneller Prozesse, wie der Dynamik von Elektronenbewegungen, erfordert Lichtimpulse, welche eine kürzere Zeitdauer haben als der Prozess selbst. Die kürzesten heute realisierbaren Lichtpulse mit Dauer im Attosekundenbereich werden mit Hilfe hoher harmonischer Strahlung durch Frequenzkonversion von Femtosekundenpulsen aus Titan-Saphir-Verstärker-Systemen gewonnen. Die Femtosekundenpulse für die Erzeugung hoher harmonischer Strahlung (engl. *high-order harmonic generation*, HHG) dürfen dabei nur wenige optische Zyklen des Feldes unter ihrer Einhüllenden haben, damit ein kontinuierliches Spektrum im extrem-ultravioletten (XUV) Spektralbereich generiert werden kann, welches notwendig für die Herstellung von isolierten Attosekundenpulsen (IAP) ist. Diese Femtosekundenpulse können mit Hilfe von verstärkten Laserpulsen über nicht-lineare Prozesse, wie der Selbstphasenmodulation, realisiert werden, welche sich z.B. bei der Laser-Filamentation ereignen.

In dieser Arbeit werden Untersuchungen an einer semi-infiniten Gaszelle (engl. *semi-infinite gas cell*, SIGC) zur HHG durchgeführt. Der Parameterbereich zur HHG mit optimaler Konversionseffizienz wird identifiziert. Zum tieferen Verständnis der experimentellen Untersuchungen werden Simulationen zur Erzeugung und zur Phasenanpassung hoher harmonischer Strahlung durchgeführt, welche die Messungen gut reproduzieren.

Insbesondere wird die HHG durch ultrakurze Femtosekundenpulse studiert. Dabei werden Pulse mit Dauer von wenigen Femtosekunden zunächst mit Hilfe der Filamentation erzeugt und anschließend zur HHG in eine SIGC fokussiert. Die durch diese Pulse in verschiedenen Gasen erzeugte XUV-Strahlung zeigt ein verbreitertes Spektrum der harmonischen Ordnungen oder weist sogar ein breites kontinuierliches Spektrum auf.

Im letzten Teil dieser Arbeit wird die Pulskompression im Filament und die anschließende Erzeugung hoher harmonischer Strahlung in einem einzigen Aufbau kombiniert. Die SIGC wird verändert, um hohe Drücke und damit die Erzeugung eines Femtosekunden-Filaments zu ermöglichen. Ein Übergang ins Vakuum am Ende der SIGC erlaubt die Auskopplung hoher harmonischer Strahlung, welche an dieser Position durch die komprimierten Pulse direkt im Filament erzeugt wird. Intensitätsspitzen, die während der Laser-Filamentation auftreten und intensiv genug zur HHG sind, werden identifiziert. Eine dieser Intensitätsspitzen weist ein kontinuierliches Harmonischenspektrum auf, welches vielversprechend für die Erzeugung von IAP ist und damit einen neuen Weg zur IAP-Synthese mit einfachen und kompakten Aufbau darstellt.

Schlagworte: ultrakurze Pulse, Filamentation, Erzeugung hoher harmonischer Strahlung, Attosekundenpulserzeugung

Abstract

Daniel S. Steingrube

High-order harmonic generation with ultra-short pulses from filamentation

The measurement of ultra-fast dynamics such as the motion of electrons requires light pulses shorter than the duration of the process itself. The shortest realized light pulses of attosecond duration are obtained via high-order harmonic generation (HHG) by frequency conversion from Titan-Sapphire amplifier laser systems. Therefore, the driver pulses for HHG must only have a few optical cycles under their envelope in order to generate an extreme-ultraviolet (XUV) continuum which is necessary for the generation of isolated attosecond pulses (IAPs). The driver pulses can be generated from amplified laser pulses by nonlinear effects such as self-phase modulation which occur for incidence in laser filamentation.

In the present thesis, investigations on the generation of high-order harmonics in a semi-infinite gas cell (SIGC) are performed. The studies identify optimal conditions for HHG regarding the conversion efficiency. Simulations of generation and phase matching of high-order harmonics are performed which reproduce the measured data and support the understanding of the experimental results.

In particular, the generation of high-order harmonics using ultra-short driver pulses is investigated. These pulses of a few femtosecond duration are produced by pulse compression via filamentation and are focused in a SIGC for HHG. The XUV radiation created by the ultra-short pulses in different gases shows a spectrum of broadened harmonic orders or features even a broad continuous shape.

In the last part, the two steps of ultra-short pulse generation within a filament and the succeeding HHG are combined in a single stage. The SIGC design is changed to allow for a high pressure and thus enables the generation of a femtosecond filament. A transition to vacuum at the end of the SIGC permits to couple out the high-order harmonic radiation which is generated by the compressed pulses at this position directly in the filament. Intensity spikes are identified, which occur during laser filamentation and are intense enough for the production of high-order harmonics. The harmonic spectrum of one of these spikes shows a continuum which is promising for the generation of IAPs. These results suggest a new route to IAP production with a simple and compact setup.

Key words: ultra-short pulses, filamentation, high-order harmonic generation, attosecond pulse generation

Contents

1	Introduction	1
1.1	Motivation for the present work	2
2	Basics	5
2.1	Interaction of light and matter	5
2.1.1	The Kerr effect	6
2.1.2	Optical field ionization	7
2.2	Filamentation	10
2.2.1	Moving focus model	10
2.2.2	Self-guiding model	11
2.2.3	Dynamic spatial replenishment model	12
2.2.4	Filamentation for ultra-short pulse generation	13
2.3	High-order harmonic generation	13
2.3.1	The three-step model	14
2.3.2	The Lewenstein model	16
2.3.3	The atomic phase	19
2.3.4	Attosecond pulse generation	22
2.4	Phase matching of high-order harmonics	23
2.4.1	Phase contributions	26
2.4.2	Coherence length	28
2.4.3	Phase-matching effects	29
2.4.3.1	Coherence properties	32

2.4.4	Geometries	34
3	HHG in a semi-infinite gas cell	37
3.1	Phase-matching experiments	37
3.1.1	Experimental setup	38
3.1.2	Dependence on focus position	40
3.1.3	Pressure dependence	47
3.1.4	Trajectory contributions and coherence properties	49
3.1.5	Spectral splitting, broadening, and blue shift	52
3.2	Harmonic generation from ultra-short pulses	56
3.2.1	Generation of ultra-short pulses using filamentation	56
3.2.2	Spectral broadening of high-order harmonics	58
3.3	Conclusion	61
4	Direct HHG within a filament	63
4.1	The occurrence of intensity spikes in filamentation	64
4.2	Experimental observation of intensity spikes	65
4.2.1	Experimental realization	65
4.2.2	Generation of high-order harmonics by intensity spikes	67
4.2.3	Numerical results	71
4.2.4	Control of the intensity spikes	73
4.3	Conclusion	78
5	Conclusion and outlook	79
 Appendix		
A	Experimental methods	83
A.1	The laser system	83
A.2	Spatially resolved measurement of the coherence time	83

A.3	Single-shot measurements	85
A.4	Analysis of the intensity spikes	85
A.5	Calibration of the absolute chirp	86
B	Calculations	89
B.1	Genetic fitting algorithm	89
B.2	Numerical simulations of harmonic generation in a filament	90
B.3	Peak-power reduction caused by dispersion	91
	Bibliography	93
	Acknowledgments	105
	Curriculum Vitae	107
	Publications	109

CONTENTS

Abbreviations and symbols

Abbreviations

ADK	Ammosov-Delone-Krainov
ATI	above threshold ionization
CCD	charge-coupled device
CEO	carrier-envelope offset
CPA	chirped pulse amplification
DCM	double-chirped mirror
FWHM	full width at half maximum
GDD	group-delay dispersion
HHG	high-order harmonic generation
IAP	isolated attosecond pulse
IR	infrared
MPI	multiphoton ionization
MCP	multi-channel plate
OTBI	over-the-barrier ionization
SAEA	single active electron approximation
SFA	strong-field approximation
SHG	second harmonic generation
SIGC	semi-infinite gas cell
SPIDER	spectral phase interferometry for direct electric field reconstruction
SPM	self-phase modulation
THG	third harmonic generation
XUV	extreme ultra violet

Table 1: Abbreviations.

Mathematical symbols

\vec{A}	vector potential (cf. Sec. 2.3.2)
α	slope of atomic phase ϕ_{at} versus intensity (cf. Eq. (2.27))
β	group delay dispersion
c	speed of light in vacuum
c.c.	complex conjugate
d_x	dipole matrix element (x -component, cf. Eq. (2.22))
ε_0	permittivity of vacuum
e	Euler number ($\exp(1)$)
e	electron charge
\mathcal{E}	electric field
E	slowly varying envelope of the electric field
f	focal length
\mathcal{FT}	Fourier transform
ϕ_{at}	atomic phase (cf. Eq. (2.27))
ϕ_{geo}	geometric phase (cf. Eq. (2.41))
$\Delta\phi_{\text{neu}}$	phase mismatch from dispersion of neutral atoms (cf. Eq. (2.42))
$\Delta\phi_{\text{el}}$	phase mismatch from dispersion of free electrons (cf. Eq. (2.47))
$\Delta\Phi$	complex phase mismatch (cf. Eq. (2.40))
\mathcal{N}	number density
γ	Keldysh parameter (cf. Eq. (2.8))
Γ	Gamma function
i	imaginary number
Im	imaginary part
I	intensity
I_p	ionization potential (cf. Tab. 2.1)
J_0	zero-order Bessel function
\vec{k}	wave vector
$\Delta\vec{k}$	phase-mismatch wave vector (cf. Sec. 2.4.1)
κ_q	absorption coefficient (cf. Eq. (2.45))
L_{abs}	absorption length (cf. Sec. 2.4.2)
L_c	critical length for self focusing (cf. Eq. (2.4))
L_{coh}	coherence (build-up) length (cf. Sec. 2.4.2)
L_{med}	length of the medium (cf. Sec. 2.4.2)
L_{amp}	effective length of the medium (cf. Sec. 2.4.2)
m_e	electron mass
n	refractive index
n_2	nonlinear refractive index (cf. Eq. (2.2))
p	pressure

\vec{p}	canonical impulse (cf. Sec. 2.3.2)
p_s	stationary solution of the canonical impulse (cf. Eq. (2.19))
\mathcal{P}	polarization
P	slowly varying envelope of the polarization
P_{cr}	critical peak power for self focusing (cf. Eq. (2.3))
r	coordinate perpendicular to the propagation direction
r_{el}	classical electron radius (cf. Sec. 2.4.1)
q	harmonic order
Re	real part
S	quasi-classical action (cf. Eq. (2.20))
S_s	stationary solution of the quasi-classical action (cf. Eq. (2.20))
t	time coordinate
T_{coh}	coherence time (cf. Eq. (2.53))
τ	traveling time (cf. Sec. 2.3.1)
τ_d	delay (cf. Sec. 3.1.4)
U_p	ponderomotive potential (cf. Eq. (2.9))
V	fringe-visibility / contrast function $V(\tau_d)$ (cf. Eq. (2.52))
W	ionization rate (cf. Eq. (2.10))
ω	angular frequency (of the fundamental field)
ω_p	plasma frequency (cf. Eq. (2.13))
χ	susceptibility
\ddot{x}	atomic dipole acceleration (cf. Eq. (2.16))
z	coordinate in propagation direction
z_f	focus position (cf. Sec. 3, Fig. 3.2)
z_{R}	Rayleigh length

Table 2: Mathematical symbols.

CONTENTS

Chapter 1

Introduction

Attosecond physics is a mature field in science which has grown over the last two decades with many interesting applications [Kra09, L'H03]. The synthesis of pulses with attosecond duration¹ enables for instance the time-resolved study of electron dynamics using pump-probe schemes [Cav07, Hen01] or exploiting the coherent nature of their generation process [Sta07]. Also proton dynamics and chemical reactions have been studied on an attosecond time scale [Bak06, Li08, Wör10]. Nowadays, a precision down below 6 as is reached [Eck08], and pulses as short as 80 as [Gou08] have been demonstrated.

With the invention of the chirped-pulse amplification (CPA) technique [Str85] high-energy infrared (IR) light pulses in the millijoule regime with pulse durations as short as tens of femtoseconds became available. The peak field strengths of these pulses reaches a magnitude in the order of the atomic Coulomb field, permitting highly non-linear processes beyond the perturbation theory [Pro97, and references therein]. One of these strong-field processes is the high-order harmonic generation (HHG) featuring coherent radiation, which covers a spectrum far into the extreme-ultraviolet (XUV) spectral region. The first experimental observations of high-order harmonics in rare gases, were reported in 1987 by McPherson *et al.* [McP87] and in 1988 by Ferray *et al.* [Fer88]. Since then, HHG was studied with increasing interest in both experimental and theoretical studies [Ago04, Ede04, L'H91, Pro97, and references therein]. In 1993, Corkum [Cor93] provided a first explanation of the HHG process in a semi-classical picture. A quantum mechanical treatment in a strong-field approximation (SFA) followed by Lewenstein *et al.* [Lew94] in 1994. Since high-order harmonic radiation covers a wide bandwidth in the XUV spectral region, it serves as an ideal tool for spectroscopic applications [Goh05, Ita04, L'H03]. Moreover, the coherence properties of the radiation can be exploited for attosecond pulse production

¹1 as = 10^{-18} s

and time-resolved studies [Bak06, Hen01, Li08].

Attosecond pulses The most prominent feature of high-order harmonics is the spectrum covering an ultra-broad range in the XUV spectral region. Due to the coherent nature of the HHG process, the XUV spectrum can be exploited for the synthesis of pulses, which occur on an attosecond time scale [Ago04, Kra09, Scr06, and references therein]. Pulses of this short duration permit the time-resolved investigation of ultra-fast processes taking place on the time scale of electron dynamics in atoms [Bak06, Hen01]. The duration of the produced pulses depends on the bandwidth of the XUV spectrum, which can be exploited for pulse synthesis. However, the harmonic spectrum, which is generated by driver pulses with many cycles under their envelope, exhibits a discrete structure from the individual harmonic orders. This deeply modulated XUV spectrum generates a train of attosecond pulses emitted at every half-cycle of the driving laser pulse. Many applications of attosecond pulses, as the investigation of electron dynamics by pump-probe schemes, require isolated attosecond pulses (IAPs), which occur with the same repetition rate as the driving laser. Therefore, driver pulses must be applied, which only have a few cycles under their envelope [Bra00], generating a continuous harmonic spectrum. The first measurement of IAPs of 650 as duration was reported in 2001 by Hentschel *et al.* [Hen01] followed by a number of groups and applications [Kra09, and references therein].

1.1 Motivation for the present work

The present work comprises three major topics which are motivated in the following. First, the semi-infinite gas cell (SIGC) geometry for HHG is systematically studied on an experimental basis and compared to simulations. Next, this geometry is used for generation of continuous XUV radiation using few-cycle pulses from filamentation. Finally, the two steps of few-cycle pulse production and HHG are combined in a single stage for the generation of continuous XUV spectra directly from a filament.

Different geometries have been employed for the generation of high-order harmonics, among which a gas jet is the most prominent and best studied [Sal97]. As an alternative, the SIGC was introduced in 2001 by Papadogiannis *et al.* [Pap01], which has certain advantages over the gas jet due to the simple and alignment-free setup. Moreover, the SIGC features very high conversion efficiencies [Bri09] and the precise knowledge of the pressure allows for controlled conditions and a good comparison with simulations. The SIGC can be used at very high pressures regardless of the repetition rate of the laser, which is a limitation for a pulsed gas jet geometry. Hence

featuring all these advantages, the generation of high-order harmonics in a SIGC is rarely investigated. In the present thesis, systematic experimental investigations of HHG in a SIGC are performed and compared to numerical simulations for improving the understanding of HHG and the phase matching in this geometry. Optimal conditions for HHG shall be found in the experimental parameter space. Further, coherence properties will be investigated, which are of importance for the generation of attosecond pulses.

A main application of high-order harmonics is the production of IAPs. Therefore, ultra-short driver pulses must be applied for the HHG process. Beside gating techniques for virtual pulse shortening by a temporally confined HHG within a certain time window of the pulse [Alt08, Mas08, San06b, Sol06, Tza07], pulse compression can be obtained by spectral broadening. A common technique for pulse compression is based on the self-phase modulation during propagation in a gas filled hollow-core fiber [Nis97, San06a, Tho09, Wag04]. The gating techniques are highly sensitive to mechanical vibrations and must be carefully stabilized since a nested interferometric setup is applied. The spectral broadening in a hollow-core fiber is limited in the applicable pulse energies due to damages of the mechanical guiding. Both techniques are accompanied by a high experimental effort for the alignment. An alternative route to few-cycle pulse generation was demonstrated in 2004 by Hauri *et al.* [Hau04] using femtosecond filamentation for pulse compression of high-energy pulses. A filament constitutes a self-guided light channel with high intensity over a long propagation distance which goes along with spectral broadening by self-phase modulation [Cou07, and references therein]. Due to the absence of mechanical guiding, the filament is free of alignment and possesses a promising energy scaling [Var09]. The first application of pulses, which were compressed by filamentation, to the generation of high-order harmonics was reported in 1998 by Lange *et al.* [Lan98] up to the 15th order. Zair *et al.* [Zai07] generated harmonics up to the 33rd order showing small spectral broadening due to the short pulse duration of the compressed pulses. A production of a continuous XUV spectrum by filamented pulses, which is required for the synthesis of IAPs, has not been reported at the time of this work, but was demonstrated recently [Lee09, Ste09a]. In the present work, ultra-short pulses from a filament will be applied with the aim to generate ultra-broad XUV spectra as a route to IAP production. Therefore, the SIGC is used at optimized conditions for HHG in different noble gases.

In the last part of the present work, the two steps of ultra-short pulse generation within a filament and the succeeding HHG are combined in a single stage. A recent theoretical study predicts the generation of high-order harmonics by intensity spikes, which occur during femtosecond filamentation in gases [Gaa09]. This theory contradicts established filamentation models assuming a *clamped* intensity around

the ionization threshold [Bra95, Cou07, and references therein]. Since the predicted intensity spikes occur on a sub-pulse of near single-cycle duration, the production of IAPs directly from the filament becomes possible. This combines pulse compression by spectral broadening and harmonic generation within a single stage and a simple setup, reducing experimental complexity for IAP sources. In turn, the generated harmonic radiation acts as a nonlinear probe of the IR intensity within the filament which allows to experimentally validate the theoretical predictions of intensity spikes. In the last part of this thesis, the aim is to experimentally verify the occurrence of intensity spikes in filamentation by the measurement of high-order harmonics which are generated directly within a filament. Therefore, the SIGC design will be modified to sustain atmospheric pressure for the formation of a gas filament by femtosecond pulses. The direct generation of XUV radiation and its properties will be investigated aiming for the synthesis of IAPs from this simple and compact setup.

The thesis is organized in four parts. Chapter 2 introduces into the strong-field physics and describes the theoretical background. Chapter 3 shows the results of the systematic investigation of the SIGC geometry and the application of few-cycle pulses from filamentation. Chapter 4 demonstrates the generation of high-order harmonics directly from a filament. Finally, Chapter 5 summarizes the present work and gives an outlook on future studies.

Chapter 2

Basics

This Chapter describes the basic theoretical aspects of the interaction between light and matter. First, the Kerr effect derived from perturbation theory is introduced (Sec. 2.1.1). Then, ionization (Sec. 2.1.2) and high-order harmonic generation (HHG) beyond the perturbation theory are discussed (Sec. 2.3). Phenomena of HHG stemming from the single-atom response (Sec. 2.3.3) and from propagation effects (Sec. 2.4) are highlighted. Finally, the nonlinear process of filamentation of ultra-short laser pulses is addressed (Sec. 2.2).

2.1 Interaction of light and matter

The influence of a light field $\vec{\mathcal{E}}$ on matter can be modeled by the polarization $\vec{\mathcal{P}} = \underline{\underline{\chi}}\vec{\mathcal{E}}$ where $\underline{\underline{\chi}}$ is the susceptibility of the medium. Throughout the thesis, linearly polarized light is considered, because it is relevant for HHG. Thus, the scalar representation of the field \mathcal{E} and the polarization \mathcal{P} are used in the following. In the linear case for a very weak light field, the susceptibility is independent of the incident field. Already at moderate intensities produced by common laser oscillators, a nonlinear dependency of the susceptibility becomes observable, which can be treated as a perturbation of the linear case. Therefore, the susceptibility is expanded into a Taylor series

$$\chi = \chi_1 + \chi_2\mathcal{E} + \chi_3\mathcal{E}^2 + \dots, \quad (2.1)$$

where χ_1 denotes the linear susceptibility, and χ_i denotes the nonlinear susceptibility of order $i > 1$. Perturbation theory of light-matter interaction explains many nonlinear effects, such as second or third harmonic generation (SHG/THG), self-phase modulation (SPM), self-focusing, and multiphoton ionization (MPI).

2.1.1 The Kerr effect

One important result from perturbation theory is a third order process, inducing an intensity dependent refractive index n_2I in addition to the static refractive index n_0 :

$$n = n_0 + n_2I \quad (2.2)$$

with intensity I . This Kerr effect has some interesting consequences for beam propagation and the temporal evolution of a beam in a nonlinear Kerr medium as discussed below. In argon at atmospheric pressure, n_2 takes a value of about $1.74 \times 10^{-19} \text{ cm}^2/\text{W}$ [Cou08],¹ which is connected to the third order susceptibility via $\chi_3 = 4\varepsilon_0cn_0^2n_2/3$, where ε_0 denotes the vacuum permittivity, and c is the vacuum speed of light [Cou07]. Note that the nonlinear refractive index depends in good approximation linearly on the pressure of the nonlinear medium [Bör10, Mar75]. In the following paragraphs, two implications of the Kerr effect will be discussed: the self-focusing effect, stemming from a spatial variation of the nonlinear index, and the self-phase modulation which has its origin in the temporal index variation.

Self-focusing The spatial intensity profile of a laser beam induces a spatially dependent variation of the refractive index in a nonlinear Kerr medium. Therefore, the refractive index in the beam center is higher than in the wings (if $n_2 > 0$), and an index gradient of a focusing lens is generated in the medium causing the beam to focus. This effect of self-focusing occurs above a critical peak power of the input pulse which is given for a Gaussian beam by [Cou07, Mar75]

$$P_{\text{cr}} = \frac{3.77\pi c^2}{2n_0n_2\omega^2} \quad (2.3)$$

with fundamental angular frequency ω . Above this peak power, the lens induced by the Kerr effect is stronger than the natural diffraction of the laser beam. Note that the factor of 3.77 is valid for a Gaussian beam and varies with the spatial shape of the beam [Cou07]. Assuming a Gaussian beam with a center wavelength of 780 nm in 1 bar argon yields for example a critical power of 5.2 GW. In order to reach such a peak power with a laser pulse of a full-width at half-maximum (FWHM) duration of 35 fs, one would need pulses with energies of about 0.2 mJ. A consequence of self-focusing is a collapse of the beam after a length L_c given by the semi-empirical formula [Mar75]:

$$L_c = \frac{0.367 z_R}{\sqrt{\left(\sqrt{P_{\text{peak}}/P_{\text{cr}}} - 0.852\right)^2 - 0.0219}} \quad (2.4)$$

¹Note that the measured values of n_2 are ranging in literature over an order of magnitude [Bör10].

with the Rayleigh length z_R and the peak power P_{peak} . While Eq. (2.4) is valid for a collimated input beam, a beam focused with effective focal length f collapses at a smaller distance given by [Cou07]

$$L_{c,f} = \left(L_c^{-1} + f^{-1}\right)^{-1}. \quad (2.5)$$

Is is shown below that other nonlinear effects, such as plasma generation, avoids the collapse of a beam, but can lead to the phenomenon of filamentation, cf. Sec. 2.2.

Self-phase modulation Analogous to the induced index variation by the spatial beam profile, the temporal profile of the pulse generates a refractive index which dynamically changes over time. This causes an additional phase term ϕ_{SPM} which changes in time as

$$\Delta\omega = -\frac{\partial\phi_{\text{SPM}}}{\partial t} \propto -n_2\frac{\partial I(t)}{\partial t}. \quad (2.6)$$

This *self-phase modulation* (SPM) in turn, is a source for the generation of new frequencies $\Delta\omega$ around the center frequency ω , as will be discussed below for the case of filamentation.

2.1.2 Optical field ionization

Strong-field processes in atoms occur when the intensity I of a light field reaches the order of magnitude of the atomic potential. The electric field induced by the Coulomb potential can be estimated to $E_a = e/4\pi\epsilon_0x^2 \sim 10^9$ V/cm, where $x \approx 0.1$ nm denotes the typical atomic length scale. In order to reach optical fields at this strength, an intensity in the order of

$$I = \frac{c\epsilon_0}{2} |E_a|^2 \sim 10^{15} \text{ W/cm}^2 \quad (2.7)$$

is necessary. The explanation of the nonlinear response of the medium by the perturbation theory fails in this case, and must be solved in a quantum mechanical treatment (cf. Sec. 2.3).

Strong-field processes are always accompanied by optical field ionization. While at lower intensities the multiphoton ionization (MPI) is dominant, the tunnel ionization becomes more prominent in the strong case. The predominant ionization path can be distinguished by the dimensionless parameter [Kel65]

$$\gamma = \sqrt{I_p/2U_p} \quad (2.8)$$

Gas	xenon	hydrogen	krypton	argon	neon	helium
I_p (eV)	12.1298	13.5984	13.9996	15.7596	21.5645	24.5874

Table 2.1: Ionization potential I_p of selected gases [Mar10].

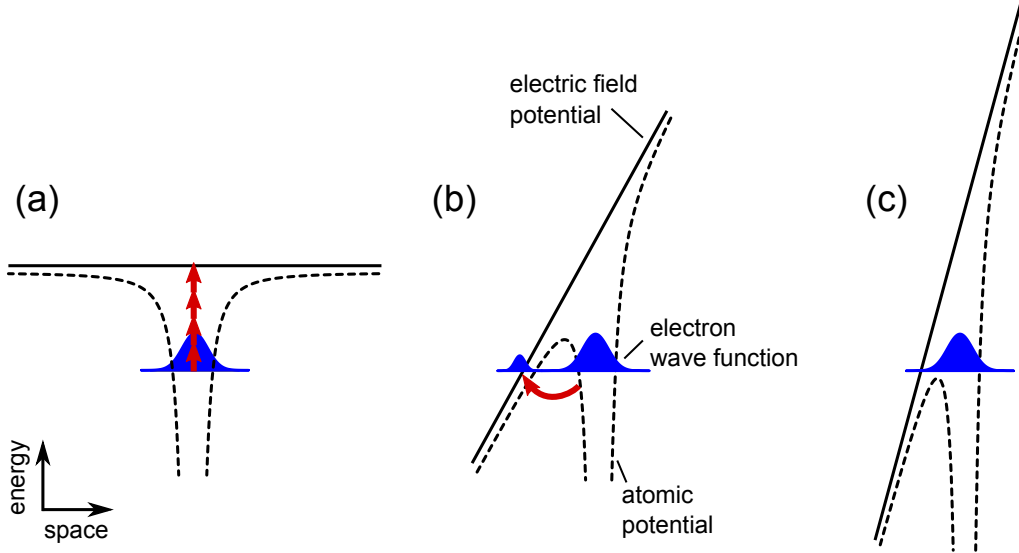


Figure 2.1: Different ionization schemes: (a) multiphoton ionization (MPI), (b) tunnel ionization, (c) over-the-barrier ionization (OTBI). The dashed line sketches the atomic potential bended by the electric light field indicated as thin solid line. The electron wave function is sketched in blue. The arrows in (a) indicate the simultaneous absorption of multiple photons in order to reach the ionization threshold.

which sets the ionization potential I_p in relation to the ponderomotive potential energy U_p . This energy is given by

$$U_p = \frac{e^2 \mathcal{E}^2}{4 m_e \omega^2}, \quad (2.9)$$

and denotes the time averaged kinetic quiver energy which an electron of charge e and mass m_e acquires in an external electric field \mathcal{E} of angular frequency ω . For the estimate of the strong field intensity of $\sim 10^{15}$ W/cm² in Eq. (2.7), a ponderomotive potential energy in the order of $U_p \sim 80$ eV is obtained when assuming an optical field with a wavelength of 800 nm. Typical values of the ionization potential I_p are listed in Tab. 2.1. The dimensionless parameter γ in Eq. (2.8) is used to distinguish between the predominant ionization paths in the weak-field limit and in the strong-field limit, as discussed in the following. In the weak-field case of $\gamma > 1$, the ponderomotive energy is small compared to the ionization potential and ionization is obtained by simultaneous absorption of multiple photons (see Fig. 2.1(a)). In the strong-field case of $\gamma < 1$, the laser intensity is so large that the atomic potential is distorted in a way which allows the electron to tunnel out of the bonding potential through the

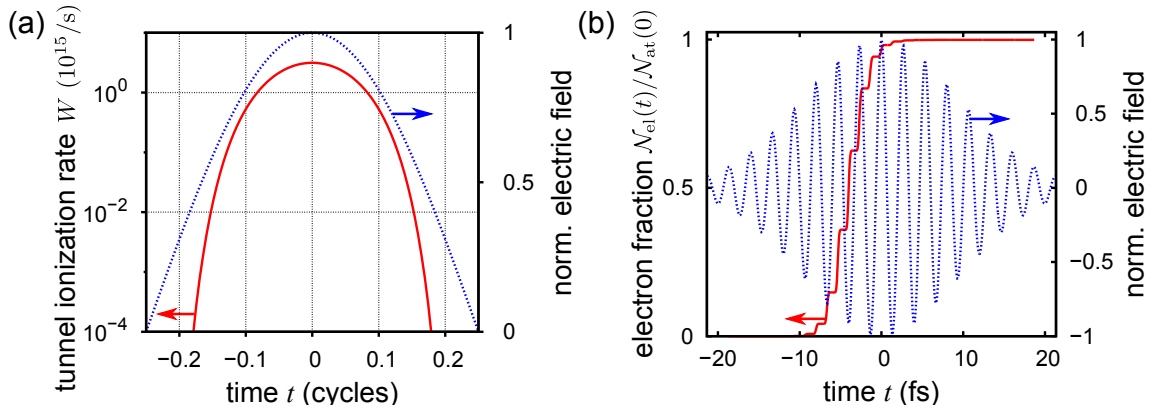


Figure 2.2: Tunnel-ionization rate in xenon predicted from the ADK-theory (see text for details). (a) Tunnel-ionization rate $W(\mathcal{E}(t))$ over a half-cycle of the laser field for an intensity of $1.5 \times 10^{14} \text{ W/cm}^2$ in xenon. (b) Fraction of free electrons versus time for a Gaussian pulse of 16 fs duration (FWHM), a wavelength of 800 nm, and a peak intensity of $1.5 \times 10^{14} \text{ W/cm}^2$. In both plots (a) and (b), the blue dashed lines show the laser electric field.

potential barrier (tunnel ionization, see Fig. 2.1(b)). At even higher intensities, the atomic potential is distorted so strongly that the barrier for the electron is suppressed below the atomic energy level. The electron is released “over the barrier” (over-the-barrier ionization (OTBI), see Fig. 2.1(c)). Optical field ionization constitutes the basis for interesting phenomena arising in strong-field physics [Ede04, Pro97], among which high-order harmonic generation (HHG) will be discussed in Section 2.3.

Tunnel-ionization rate The ionization rate in the regime of tunnel ionization is relevant for the present work. It can be calculated on the basis of the Ammosov-Delone-Krainov (ADK) theory [Amm86, Cor93]. Here, the optical electric field \mathcal{E} is assumed to be quasi-static, since ionization occurs within a fraction of an optical cycle. Considering an electron in the ground state (quantum numbers $l = 0, m = 0$) of a hydrogen like atom with ionization potential I_p , the instantaneous ionization rate for a linearly polarized laser field is given by [Amm86]

$$W(\mathcal{E}) = \frac{I_p |c_{n^*}|^2}{\hbar} \left(\frac{4 I_p}{\hbar \omega_{\mathcal{E}}} \right)^{2n^*-1} \exp\left(-\frac{4 I_p}{3 \hbar \omega_{\mathcal{E}}} \right). \quad (2.10)$$

Thereby, $\omega_{\mathcal{E}} = \sqrt{e^2 \mathcal{E}^2 / 2 m_e I_p}$ takes the magnitude of the instantaneous laser field \mathcal{E} into account. Further, there is $n^* = \sqrt{I_p^H / I_p}$ with the ionization potential I_p^H of hydrogen, and $|c_{n^*}|^2 = 2^{2n^*} / [n^* \Gamma(n^* + 1) \Gamma(n^*)]$, where Γ denotes the Gamma function [Amm86]. The evolution of the function $W(\mathcal{E}(t))$ is illustrated in Fig. 2.2(a). As expected, the maximum probability of ionization is at the maximum of the electric

field. According to the differential equation $d\mathcal{N}_{\text{at}} = -\mathcal{N}_{\text{at}}W(\mathcal{E})dt$ for the density \mathcal{N}_{at} of neutral atoms, the density \mathcal{N}_{el} of free electrons is obtained by integration over the time:

$$\mathcal{N}_{\text{el}}(t) \equiv \mathcal{N}_{\text{at}}(0) - \mathcal{N}_{\text{at}}(t) = \mathcal{N}_{\text{at}}(0) \left(1 - \exp\left(-\int_{-\infty}^t dt' W(\mathcal{E}(t'))\right) \right). \quad (2.11)$$

Exemplarily, Fig. 2.2(b) depicts the fraction of electrons versus time in xenon. It demonstrates that a xenon atom can be completely ionized during the raising edge of a strong laser pulse. The consequences for HHG will be discussed in Secs. 2.3.3 and 2.4.3. The ionization rate from Eq. (2.10) will be applied in this work for phase-matching simulations of high-order harmonics (cf. Sec. 2.4).

2.2 Filamentation

One possible route to isolated attosecond pulses (IAPs) is the application of high-power few-cycle driver pulses to HHG, as will be discussed in Sec. 2.3.4. The production of these intense few-cycle pulses is performed by spectral broadening of amplified ultra-short pulses. The common technique relies on gas filled hollow-core fibers [Nis97, San06a, Tho09, Wag04], where spectral broadening happens via SPM in the gas. A relatively new method is the femtosecond filamentation of high-power laser pulses in gaseous media [Hau04].

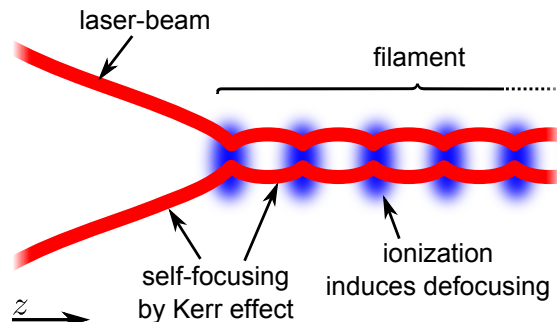
Filamentation describes the propagation of light in a nonlinear medium over extremely long lengths at a narrow beam radius without external guiding techniques (see Ref. [Cou07] for a review). This regime extends over lengths many times longer than the usual diffraction length. Due to the small beam radius in a filament, high intensities are reached within the core of the filament. This can be exploited for driving nonlinear effects over very long distances. In view of spectral broadening, the filament can be applied for inducing SPM at high intensities.

There are different models to explain filamentation, which are shortly introduced in the following.

2.2.1 Moving focus model

The moving focus model describes the process of filamentation by a transient self-focusing with different focal lengths for different time slices of the pulse [She71]. Therefore, the pulse is considered in time slices having different intensities due to the pulse envelope. The intensity dependence of the self-focusing effect implies a

Figure 2.3: Sketch of focusing-defocusing cycles in a filament proposed by the self-guiding model. Above a critical power the beam starts self-focusing. The increasing intensity results in plasma generation with a spatial profile of free electrons which induce a refractive index variation of a defocusing lens. A series of focusing-defocusing cycles leads to the formation of the filament as a self-guiding light channel.



different focus position for each time slice with minimum focal length for the pulse maximum. As a consequence, however, the built-up light channel does not go beyond the geometrical focus position, which contradicts to many experimental observations with femtosecond laser pulses [Cou07].

2.2.2 Self-guiding model

The self-guiding model, or self-channeling model [Bra95] is based on the self-trapping model [Chi64] which considers the balance between self-focusing and natural diffraction. Thereby, the induced intensity dependent refractive index of the Kerr effect leads to an increase of the angle for total internal reflection. As a consequence, the spreading by diffraction is suppressed. The self-trapping model is only valid for moderate pulse intensities.

At high pulse intensities, the self-channeling model extends the self-trapping model by contributions from free electrons, which are generated by optical field ionization by the strong laser pulse. Due to the spatial intensity profile $I(r, z)$ of the beam, ionization leads to a distribution of free electrons $\mathcal{N}_{\text{el}}(I(r, z))$. In turn, the refractive index contribution n_{el} of the free electrons depends directly on the electron density [Bra95, L'H91, Pfe06]:

$$n_{\text{el}}(\omega) = \sqrt{1 - \frac{\omega_p^2}{\omega^2}}, \quad (2.12)$$

where ω is the fundamental frequency and ω_p is the plasma frequency given by

$$\omega_p^2 = \frac{e^2}{m_e \epsilon_0} \mathcal{N}_{\text{el}}. \quad (2.13)$$

This leads to a minimum of the refractive index at the beam center,² where the

²In first order approximation, it is $n_{\text{el}} - 1 \propto -\mathcal{N}_{\text{el}}$ (cf. Eq. (2.46)).

ionization is most efficient, acting as a defocusing lens. The counteracting effect is the Kerr self-focusing induced by the intensity dependent refractive index of the nonlinear medium (cf. Sec. 2.1.1). As a consequence, the filament is built up by a series of focusing-defocusing cycles which balance to a self-guiding light channel in the nonlinear medium (see Fig. 2.3). A result of the self-guiding model is the balance between the Kerr effect and the plasma generation which implies a maximum equilibrium intensity in the light channel. Due to plasma generation, this *clamping intensity* near the ionization threshold cannot be exceeded. The balance between self-focusing (i), plasma defocusing (ii), and natural diffraction (iii) can be approximated by the equation [Bra95]

$$\underbrace{n_2 I}_{(i)} = \underbrace{\frac{\omega_p^2}{2\omega^2}}_{(ii)} + \underbrace{\frac{(1.22c)^2 \pi}{2n_0 \omega^2 w_0^2}}_{(iii)} \quad (2.14)$$

with beam radius w_0 . The model predicts³ stable self-guiding at a wavelength of 775 nm and a clamping intensity of 7×10^{13} W/cm². Since neither temporal dynamics of the pulse envelope nor spatial variation of the intensity is involved in the model, it provides a rough estimate, which yields the order of magnitude of the corresponding entities. A better estimation [Cou07] that accounts for the pulse duration yields a stable filament with diameter of 220 μ m and a clamping intensity of 1.6×10^{13} W/cm² for a 100 fs pulse at 800 nm central wavelength. Measurements of fluorescence spectra [Bec01] confirm this estimate.

The filament finally breaks up when multiphoton absorption and ionization lead to an unbalancing due to energy losses. This unbalancing is retarded by an energy cladding which surrounds the hot core of the filament and supplies it with energy [Nib96]. Typical lengths of a filament reach from tens of centimeter in the laboratory up to several meters or kilometers for atmospheric applications [Méc04].

2.2.3 Dynamic spatial replenishment model

The model of dynamic spatial replenishment extends the self-guiding model by the spatio-temporal dynamics. While the self-guiding model has a static view on the filamentation process, the dynamic spatial replenishment model [Mle98] considers the pulse propagation in the filament as a highly dynamical process. The pulse front generates a plasma by optical field ionization, causing defocusing of the pulse tail. The intensity of the pulse front decreases, allowing for another self-focusing cycle

³Assuming air with $n_2 = 5 \times 10^{-19}$ cm²/W, and a free electron density of about 0.16% of atmospheric air concentration [Bra95].

due to less plasma generation. Analogously to the self-guiding model, these cycles repeat and form the filament until the loss of energy is too high.

2.2.4 Filamentation for ultra-short pulse generation

The filamentation process is accompanied by a huge spectral broadening. Due to the high intensity in the hot core of the filament, nonlinear effects can take place over a very long range. Beside SPM also self-steepening and plasma effects due to the temporally varying free electron density lead to a characteristic shape of the generated spectrum after filamentation. In experimental studies, a pulse compression of 43-fs-amplifier-pulses of 0.84 mJ down to 5.7 fs was demonstrated in a double filamentation stage using argon as the nonlinear medium [Hau04]. It was shown that the CEO phase is conserved during the process [Hau04], thus filamentation is a considerable alternative to hollow-core-fiber based techniques [Nis97]. Analogously to pulse compression using a hollow-core fiber, the dispersion of the output pulses after the filament can be compensated by chirped mirrors. However, different from the hollow-core fiber, there are conditions in a filament where self-compression of the output pulses is obtained without the need for further dispersion management [Cou05, Cou06, Hau04]. The application of pulses after filamentation to HHG was first demonstrated by Lange *et al.* [Lan98]. Later, Zair *et al.* [Zai07] reported HHG from sub-10-fs pulses of a single filamentation stage and from sub-5-fs pulses of a double filamentation stage. They presented spectral broadening of the generated harmonics in argon due to the short pulse duration of the applied driver pulses. Simulations predict that pulses, which are compressed by a filament, can be used for IAP production [Cha06, Cou08]. Recent experimental studies showed that a continuous XUV spectrum can be generated by few-cycle pulses from a filament [Lee09, Ste09a].

2.3 High-order harmonic generation

The generation of (low-order) harmonics in a weak laser field can be understood in the multiphoton picture. By simultaneous absorption of multiple photons from the laser field, an electron of an atomic system is excited to a virtual energy level. The electron relaxes into its ground state under emission of a single photon which carries the energy of all absorbed photons. Lowest order perturbation theory predicts a rapid decrease of the conversion efficiency with increasing number of absorbed photons [Pan89]. Contrary, experiments applying strong laser fields [Fer88, McP87] reveal the existence of a plateau with a sharp cutoff, where the conversion efficiency

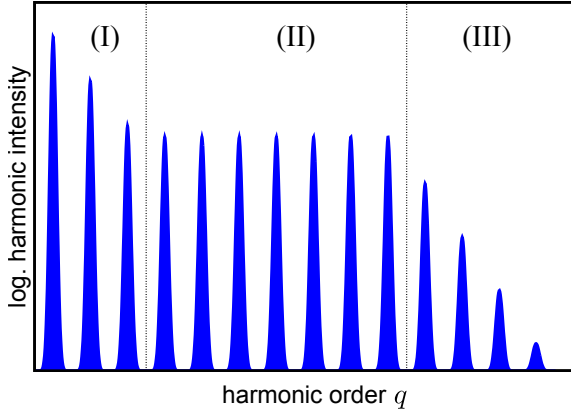


Figure 2.4: Sketch of a typical spectrum of high-order harmonics generated with a strong laser field. Three regimes are labeled which identify the perturbation region (I), the plateau region (II), and the cutoff region (III).

of high-order harmonics remains more or less equal in the plateau region (see [Ede04, L'H91] for a review and references therein). A sketch of a typical harmonic spectrum, generated by a strong laser field in a gaseous medium, is depicted in Fig. 2.4. The intensity of low orders decreases rapidly in the perturbation regime (I), whereas the harmonic intensity remains relatively constant at higher orders in the plateau regime (II). The highest orders represent the cutoff region (III), where again the harmonic intensity rapidly decreases with harmonic order. This behavior will be explained in the following two sections. First, the three-step model is discussed for a qualitative explanation of the process of HHG in a semi-classical picture. Second, the Lewenstein model is introduced allowing for quantitative predictions in a quantum mechanical treatment.

2.3.1 The three-step model

The phenomenon of high-order harmonic generation (HHG) was explained in 1993 by Corkum [Cor93] with an intuitive semi-classical picture in a three-step model. This model assumes an electron in the ground state which is released into the continuum with zero initial velocity at the place of the atom by tunnel ionization in the first step (i), cf. Fig. 2.5. In the second step (ii), the electron is accelerated classically in the external laser field which, if polarized linearly, drives the electron back to the parent ion. With a certain probability, the electron recombines with the ion in the last step (iii) under emission of a photon with the energy of the ionization potential I_p plus the kinetic energy E_{kin} , acquired during the acceleration of the electron before recombination. The kinetic energy E_{kin} of the electron as well as the traveling time τ between ionization and recombination is a function of the ionization time t' , depicted in Fig. 2.6. The maximum kinetic energy of about $3.17 U_p$ is obtained by a single electron trajectory with onset at an ionization time of $t'_{\text{max}} \approx 0.047$ optical cycles, shortly after the maximum of the driving laser field. This results in a maximum

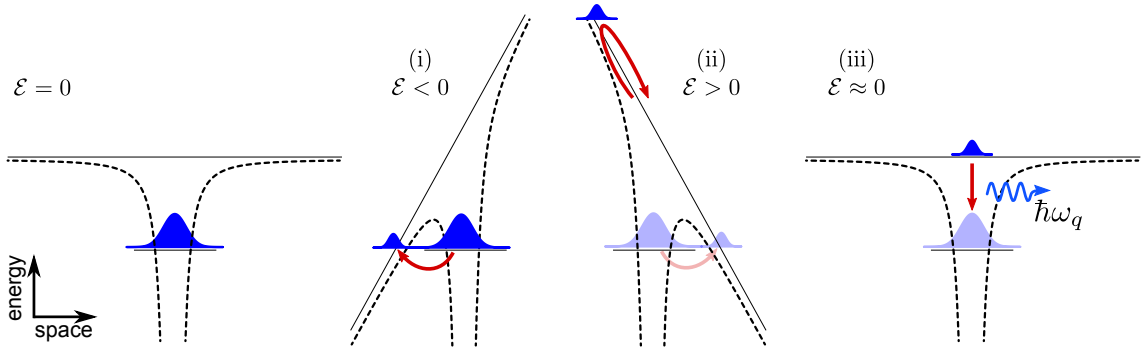
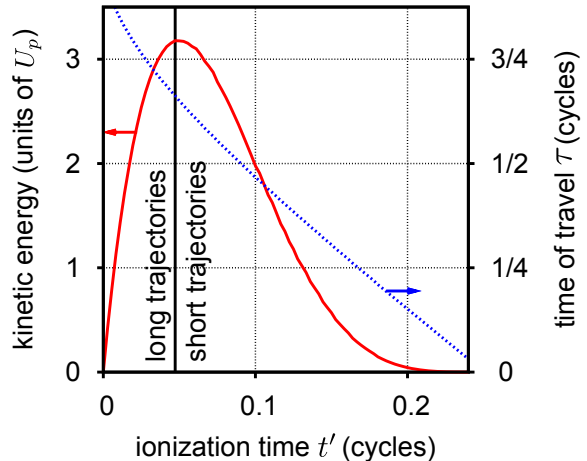


Figure 2.5: Three step model. (i) An electron is ionized from the ground state into the continuum by tunnel ionization around the maximum of the electric field. (ii) The laser field accelerates the electron in the continuum and drives it back to the ion. (iii) The electron can recombine with the ion under emission of a high energy photon. These three steps occur at every half-cycle of the laser field. The broken line sketches the atomic potential bended by the electric light field indicated as thin solid line. The electron wave function is sketched in blue.

Figure 2.6: Kinetic energy (red solid line) and traveling time τ (blue dashed line) of electron trajectories in HHG according to the three-step model in dependence of the ionization time t' (see text for details). The time is denoted in units for the driving laser period with the origin at the field maximum.



photon energy of

$$\hbar\omega_{q,\max} = I_p + 3.17 U_p, \quad (2.15)$$

defining the cutoff of the harmonic spectrum in the three-step model (cf. region (III) in Fig. 2.4). This highest photon energy is in reasonable agreement with the cutoff energy obtained in experimental studies [Kra92, L'H93].

The plateau region in the harmonic spectrum (cf. region (II) in Fig. 2.4) can be explained by considering the first step (i) of this model. The photon energies in the plateau region correspond to electrons which return with moderate kinetic energy below the maximum kinetic energy (cf. Fig. 2.6). These are released shortly after the maximum of the laser field, and thus have similar ionization probabilities (cf. Fig. 2.2(a)). As a consequence, the conversion efficiency for the corresponding photon energies in the region plateau remain relatively constant. Each kinetic energy

in the plateau is reached by two electron trajectories, as visible in Fig. 2.6. The *long* trajectory is released before t'_{\max} with a long traveling time τ_{long} , and the *short* trajectory is released after t'_{\max} with a short traveling time τ_{short} . The consequences which arise from the contributions of two electron trajectories will be discussed in Sec. 2.3.3.

The harmonic spectrum consists of only odd harmonics of the fundamental frequency due to the symmetry of the generation process. Since the three steps of HHG occur at every half-cycle of the driving laser field, the harmonic radiation interferes constructively with a frequency spacing of 2ω starting at the fundamental frequency ω . Despite of the simplicity of the three-step model, the basic features of HHG are well understood in this semi-classical picture. The model explains the plateau region as well as the sharp cutoff in the harmonic spectrum, which is not explained by perturbation theory. For quantitative predictions of the harmonic spectrum, however, a quantum mechanical treatment is necessary, introduced in the following section.

2.3.2 The Lewenstein model

A quantum mechanical treatment of the HHG process in the low-frequency, high-intensity limit was stated by Lewenstein *et al.* [Lew94] in 1994. By applying appropriate approximations stated below, this theory provides a closed-form equation to calculate the time-dependent dipole response $x(t)$ of a single atom without the need for integration of the complete time-dependent Schrödinger equation. The generated high-order harmonic spectrum can be computed via the dipole acceleration $\ddot{x}(t)$ which appears as a source for the harmonic radiation. The Lewenstein model includes important quantum effects, e.g. quantum diffusion and quantum interferences, and allows for classical interpretations of the HHG process as discussed below.

The low-frequency, high-intensity limit comprises the conditions that the photon energy $\hbar\omega$ of the fundamental field is low with respect to the ionization potential I_p ($I_p \gg \hbar\omega$), and that the ponderomotive potential U_p is equal to or higher than the ionization potential ($U_p \geq I_p$). The last condition implies that tunneling theory is applicable ($\gamma < 1$, see Sec. 2.1.2). The Schrödinger equation in its length gauge is considered with the following approximations and assumptions:

- (a) single active electron approximation (SAEA): only a single electron is considered under the influence of the laser field;
- (b) contributions from other states than the ground state of the system are negligible;
- (c) no depletion of the ground state;

- (d) strong-field approximation (SFA): the electron can be treated as a free particle without influence of the atomic potential, since it is released around the maximum of the electric field, gains rapidly kinetic energy, and is far from the ion at its turning point of motion.

With these assumptions, the Schrödinger equation can be solved, leading to an expression for the time-dependent dipole moment in the direction of the laser polarization (in atomic units) [Lew94]

$$x(t) = i \int_0^t dt' \int d^3p \underbrace{\mathcal{E}(t') d_x(\vec{p} + \vec{A}(t'))}_{(i)} \cdot \underbrace{\exp(-iS(\vec{p}, t, t'))}_{(ii)} \cdot \underbrace{d_x^*(\vec{p} + \vec{A}(t))}_{(iii)} + \text{c.c.}, \quad (2.16)$$

where d_x is the component of the atomic dipole matrix element for the ground-state-continuum transition into the direction of the laser polarization, and $S(\vec{p}, t, t')$ denotes the quasi-classical action. Thereby, the canonical momentum $\vec{p} = \vec{v} + \vec{A}(t)$ with the vector potential \vec{A} of the electric field and electron velocity \vec{v} is used.

Equation (2.16) offers a physical interpretation of the HHG process which agrees with the semi-classical three-step model (cf. Sec. 2.3.1). The first term (i) stands for the tunneling probability of an electron at time t' from the ground state into the continuum, which constitutes the first step of the three-step model. The second step is the propagation in the continuum which is treated classically in the three-step-model and is represented by the pure phase term (ii). Finally, the third step is described by the recombination amplitude at time t , term (iii).

A simplification of Eq. (2.16) is obtained by considering that the integral over \vec{p} has only major contributions from the stationary points of the quasi-classical action $S(\vec{p}, t, t')$:

$$\vec{\nabla}_{\vec{p}} S(\vec{p}, t, t') = 0. \quad (2.17)$$

Since on the other hand $\vec{\nabla}_{\vec{p}} S(\vec{p}, t, t') = \vec{x}(t) - \vec{x}(t')$ [Lew94], this implies that ionized electrons, contributing to HHG, are released close to the origin of the parent ion and return to the same position in agreement with the three-step model. Using the condition in Eq. (2.17), the saddle-point approximation can be applied, which yields in atomic units [Lew94]:

$$x(t) = i \int_0^\infty d\tau \left(\frac{2\pi}{\epsilon + i\tau} \right)^{\frac{3}{2}} \cdot d_x(p_s(t, \tau) + A_x(t - \tau)) \mathcal{E}(t - \tau) \\ \times \exp(-iS_s(t, \tau)) \cdot d_x^*(p_s(t, \tau) + A_x(t)) + \text{c.c.}, \quad (2.18)$$

where $\tau = t - t'$ is the traveling time between ionization and recombination, and A_x denotes the x -component of the vector potential. The canonical momentum of the

stationary trajectories along the polarization axis is given by [Lew94]

$$p_s(t, \tau) = -\frac{1}{\tau} \int_{t-\tau}^t dt'' A(t''), \quad (2.19)$$

and the stationary quasi-classical action is

$$S_s(t, \tau) = \int_{t-\tau}^t dt'' \left(\frac{(p_s + A(t''))^2}{2} + I_p \right) = \left(I_p - \frac{p_s^2}{2} \right) \tau + \int_{t-\tau}^t dt'' \frac{A(t'')^2}{2}. \quad (2.20)$$

The last unknown in Eq. (2.18) is the d_x component of the dipole matrix element $\vec{d}(\vec{p})$. For the sake of simplicity, a hydrogen-like atom is assumed which takes an s-wave function in its ground state [Lew94]:

$$\Psi(\vec{x}) = \frac{(2I_p)^{3/4}}{\sqrt{\pi}} \cdot e^{-\sqrt{2I_p}|\vec{x}|}. \quad (2.21)$$

Assuming the continuum states as plane waves, the dipole matrix element yields [Lew94]

$$\vec{d}(\vec{p}) = \frac{i\sqrt{2^7 I_p^5}}{\pi} \cdot \frac{\vec{p}}{\left(\frac{|\vec{p}|^2}{2} + I_p\right)^3}. \quad (2.22)$$

The acceleration $\ddot{x}(t)$ of the dipole appears as a source of the harmonic field. In order to compute the harmonic amplitude and phase at a certain order q , one takes the Fourier transform of the dipole acceleration

$$\ddot{x}_q := \mathcal{FT} \{ \ddot{x}(t) \} \Big|_{q\omega} \propto -(q\omega)^2 \cdot x(q\omega). \quad (2.23)$$

Computing the Fourier transform in Eq. (2.23) via numerical integration of Eqs. (2.19) and (2.20), the high-order harmonic spectrum for a single atom in a strong laser field can be computed according to the Lewenstein model.

For long driver pulses of tens of femtoseconds, one can further apply the slowly varying envelope approximation. Then, Eqs. (2.19) and (2.20) can be solved analytically [Lew94]:

$$p_s(t, \tau) = \mathcal{E}_0 (\cos(\omega t - \omega\tau) - \cos(\omega t)) / \omega^2 \tau, \quad (2.24)$$

$$S_s(t, \tau) = (I_p + U_p)\tau - 2U_p \frac{1 - \cos\omega\tau}{\omega^2 \tau} - \frac{U_p}{\omega} \left(\sin\omega\tau - \frac{4}{\omega\tau} \sin^2 \frac{\omega\tau}{2} \right) \cos(2\omega t - \omega\tau), \quad (2.25)$$

where a driving laser field $\mathcal{E}(t) = \mathcal{E}_0 \cos(\omega t)$ with a quasi-constant envelope \mathcal{E}_0 is considered. In Sec. 3.1, the analytical solution is used to compute the nonlinear polarization from 30-fs-pulses, as will be described in Sec. 2.4. In the simulations

of few-cycle pulses and chirped pulses (cf. Sec. 3.2), the integrals over the stationary solutions (Eqs. (2.19) and (2.20)) as well as the vector potential \vec{A} are solved numerically.

Note that the Lewenstein model approximates the harmonic generation process in the strong-field case. It is valid for higher orders only with return energy above the ionization potential, and yields a dipole strength which is up to 10 times lower than obtained by more precise calculations using the time-dependent Schrödinger equation [Gaa02, Gaa08]. Moreover, the Lewenstein model overestimates the contributions from the second trajectory [Gaa02]. Nevertheless, the Lewenstein model provides a simple algorithm for the quantitative estimation of HHG and its properties, which are discussed in the following section.

2.3.3 The atomic phase

The semi-classical three-step model predicts two electron trajectories with different traveling time ($\tau_{\text{short}}, \tau_{\text{long}}$) contributing to one harmonic order in the plateau region (cf. Sec. 2.3.1). These electron trajectories correspond to quantum paths j in the quantum mechanical Lewenstein model. Beside the two major contributions ($j = \text{short}, \text{long}$) of the short and long electron trajectory, the Lewenstein model allows further quantum path contributions of minor influence which will be neglected in the following considerations. Contrary to the three-step model, the cutoff in the quantum mechanical treatment is extended over a range of harmonics with photon energies also above $I_p + 3.17 U_p$, where the corresponding dipole strength is rapidly decreasing with harmonic order (cf. Fig. 2.4). Only a single quantum path contributes to HHG in the cutoff region.

The phase of a quantum path contribution j is determined by its quasi-classical action

$$\phi_{\text{at},j} = -S_s(\tau_j) \simeq -U_p \tau_j, \quad (2.26)$$

which is in first approximation proportional to the traveling time τ_j of the corresponding path and the ponderomotive potential U_p (cf. Eqs. (2.16) and (2.25), and Refs. [Lew95, Sal98]). Since U_p directly depends on the intensity I , there holds:

$$\phi_{\text{at},j} = -\alpha_j I \quad (2.27)$$

with the phase slope factor $\alpha_j \propto \tau_j$. For example, in the plateau region for the 27th harmonic in neon, a slope factor of $\alpha_{\text{short}} \approx 1 \times 10^{-14} \text{ rad cm}^2/\text{W}$ for the short trajectory, and $\alpha_{\text{long}} \approx 25 \times 10^{-14} \text{ rad cm}^2/\text{W}$ for the long trajectory was calculated by Gaarde and Schafer [Gaa02]. Note that Eq. (2.27) is a first order approximation, where higher orders of the intensity dependence can be accounted for by a weakly

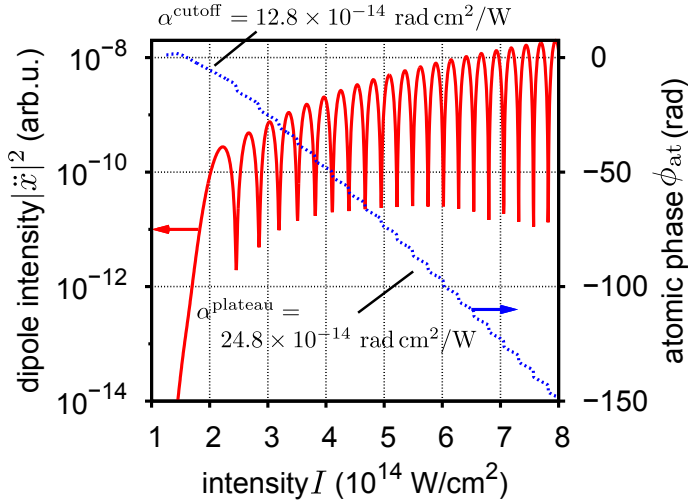


Figure 2.7: Dipole intensity and its phase versus intensity for the 45th harmonic in neon simulated by the Lewenstein model for two quantum path contributions.⁴ The phase is a piecewise linear function with different slopes in the cutoff and plateau region as labeled.

intensity dependent phase slope $\alpha_j(I)$ [cf. Gaa02].

The total harmonic field with its total phase ϕ_{at} , the *atomic phase*, consist of all contributing quantum paths. In the plateau region, with multiple quantum path contributions, this gives rise to interferences. Figure 2.7 shows exemplarily the total harmonic yield of the 45th harmonic in neon simulated with the Lewenstein model accounting only for the short and long trajectory.⁴ After the rapid increase of the total harmonic yield at a low intensity, where the harmonic is in the cutoff regime⁵ with only a single contributing quantum path, the total harmonic yield at higher intensities features interferences from the two quantum paths contributing in the plateau region. The atomic phase ϕ_{at} exhibits a piecewise and approximately linear behavior:

$$\phi_{\text{at}} \simeq -\alpha I \quad (2.28)$$

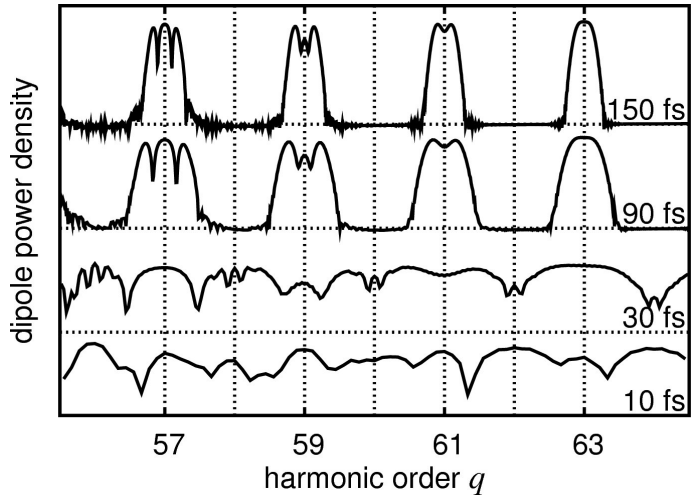
with a lower value of the phase slope α^{cutoff} in the cutoff region and a steeper slope α^{plateau} in the plateau. For the example in Fig. 2.7, the phase slope in the cutoff is $\alpha^{\text{cutoff}} \approx 12.8 \times 10^{-14} \text{ rad cm}^2/\text{W}$, and the slope in the plateau is $\alpha^{\text{plateau}} \approx 24.8 \times 10^{-14} \text{ rad cm}^2/\text{W}$. The steeper slope in the plateau region is a consequence of the long trajectory contribution with high slope factor α_{long} .

Applying ultra-short laser pulses, the intensity dependence of the atomic phase gives rise to a time dependent phase modulation. Similar to SPM in a nonlinear Kerr medium, this leads to the emergence of new frequencies $\Delta\omega_q$ in the generated

⁴Simulated single-atom response by the Lewenstein model (cf. Sec. 2.3.2) in neon using a constant driver field of 800 nm center wavelength for each intensity. Note that a bounded traveling time of one optical cycle is used to consider only two quantum path contributions of the long and short trajectory.

⁵Note that the location of the cutoff energy is intensity dependent due to $U_p \propto I$ in Eq. (2.15).

Figure 2.8: Non-adiabatic spectral splitting of harmonics in the single-atom response.⁶ The graph shows spectra of three harmonics in the plateau simulated with the Lewenstein model for different pulse durations.



harmonic radiation according to

$$\Delta\omega_q = -\frac{\partial\phi_{at}}{\partial t} \simeq \alpha \frac{\partial I(t)}{\partial t}. \quad (2.29)$$

At the rising edge of an ultra-short pulse, the rapidly changing envelope induces a blue shift of the harmonic, while on the falling edge a red shift is induced [Kan95, Shi99]. Beside a spectral broadening [Sal95], this leads to a splitting of the harmonic spectral profile, called *non-adiabatic spectral splitting* [Bru08, Kan95]. Figure 2.8 shows these effects for selected plateau harmonics generated in neon by driver pulses of different durations. For shorter pulse durations with a steeper slope $\partial I/\partial t$ of the pulse envelope, the splitting and broadening becomes more pronounced. The triple peak structure of individual harmonics⁷ originates from the interference of different quantum path contributions. Since the electron on the long trajectory remains longer in the continuum and its contribution features a higher slope α_{long} , it is more influenced by the rapidly varying envelope than the short trajectory $\alpha_{\text{short}} < \alpha_{\text{long}}$. As a consequence, the effect of spectral splitting is more pronounced for the long trajectory contribution, which is strongly blue shifted and red shifted, while the contribution of the short trajectory remains nearly unaffected.

In the cutoff region, the spectral splitting effect is less pronounced. This is because only a single quantum path with a low phase slope α^{cutoff} contributes to the harmonic yield. In addition, the harmonic field is generated around the maximum intensity of the driving laser field, where the intensity changes slowly even for ultra-short driver pulses. Nevertheless, also in the cutoff region, the spectral shape is influenced by the pulse duration of the driver pulses. The application of few-cycle driver pulses give rise to the generation of a continuous harmonic spectrum in the cutoff region

⁶Simulated single-atom response by the Lewenstein model (cf. Sec. 2.3.2) in neon using a driver pulse with 800 nm central wavelength and an intensity of $4 \times 10^{14} \text{ W/cm}^2$.

⁷See for instance the 57th harmonic for 150-fs-pulses in Fig. 2.8.

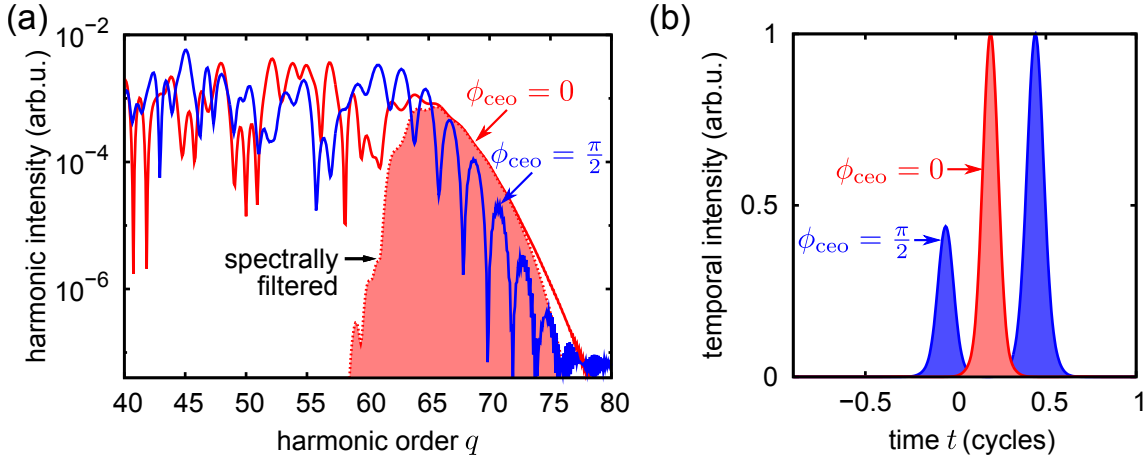


Figure 2.9: Generation of attosecond pulses by few-cycle driver pulses. (a) Spectrum of the single-atom response⁸ in neon driven by a 5-fs-pulse (800 nm central wavelength) with two different values of the carrier-envelope offset (CEO) phase ($\phi_{\text{ceo}} = 0, \pi/2$). Applying a spectral filter in the cutoff region, an isolated attosecond pulse (IAP) can be generated. (b) Corresponding temporal profile showing the emergence of an IAP generated from the pulse with $\phi_{\text{ceo}} = 0$. In case of $\phi_{\text{ceo}} = \pi/2$, a train of two attosecond pulses becomes visible. The time is denoted in cycles of the fundamental field.

which can be exploited for the production of isolated attosecond pulses (IAPs), as discussed in the following section.

2.3.4 Attosecond pulse generation

Common laser sources emit a spectrum in the near infrared region with an optical period of the electric field above a few femtoseconds. In order to generate pulses of sub-femtosecond pulse duration, a concept must be found to generate an electric field with an optical period well below the femtosecond barrier. This requires a coherent spectrum in the XUV spectral range. Frequency upconversion of infrared (IR) laser pulses by HHG is therefore the ideal method [Ago04, Gou08, Hen01, Kra09, Pau01]. Figure 2.9 exemplarily shows spectra generated by driver pulses with a center wavelength of 800 nm. The harmonic spectrum extends to the 75th harmonic order which corresponds to a wavelength of about 11 nm in the XUV spectral range. For generation of attosecond pulses an ultra-broad spectrum is necessary which is easily created by combining multiple harmonic orders. This, however, results in a train of attosecond pulses due to the discrete structure of the spectrum, which is in turn a consequence of the interference of harmonic from each half-cycle (cf. Sec. 2.3.1).

⁸Simulated single-atom response by the Lewenstein model (cf. Sec. 2.3.2) using a driver pulse with 5 fs FWHM pulse duration, 800 nm central wavelength, and an intensity of $4 \times 10^{14} \text{ W/cm}^2$.

Using a pulse with only a few optical cycles under its envelope, the highest harmonics in the cutoff are generated only within one half-cycle with the highest field strength. Due to the missing interference with contributions from another half-cycle, this gives rise to a continuous XUV spectrum in the cutoff region, as shown by the red line in Fig. 2.9(a). This may be exploited for the generation of isolated attosecond pulses (IAPs) after spectral filtering of the continuous part, as shown by the red filled curves in Fig. 2.9. Thereby, it was assumed that the maximum of the electric field oscillation coincides with the maximum of the pulse envelope. This, however, depends on the absolute phase between the carrier and the envelope, the carrier-envelope offset (CEO) phase ϕ_{ceo} . A CEO phase of $\phi_{\text{ceo}} = 0$ corresponds to the case above where the maximum of the electric field oscillation coincides with the maximum of the envelope, giving rise to XUV-continuum generation [Cav07]. In contrast, a CEO phase of $\phi_{\text{ceo}} = \pi/2$ yields a broad but modulated harmonic structure with reduced cutoff (blue line in Fig. 2.9(a)). Thus, a train of attosecond pulses is produced, as shown by the blue curve in Fig. 2.9(b).

The generation of few-cycle driver pulses, needed for IAP production, can be achieved by spectral broadening of amplified femtosecond pulses in a gaseous medium as discussed below in Sec. 2.2.4. As an alternative, it can be exploited that high-order harmonics are only generated in a linearly polarized light field. Since a circularly polarized field does not drive the electrons back to the parent ion after ionization, the recombination step is frustrated (cf. Sec. 2.3.1). The polarization gating technique [Mas08, Sol06, Tza07] uses a superposition of two circularly polarized pulses in the wings of a linearly polarized pulse. Thus, HHG takes place only on a short time duration in the linearly polarized part in the pulse center, having the similar consequences as the application of few-cycle driver pulses.

2.4 Phase matching of high-order harmonics

So far, the response of a single atom to a strong light field has been considered. In an experiment, however, not the generated harmonics of only a single atom but the coherent sum of all emitting sources contributes to the measured signal. Therefore, in order to maximize the measured harmonic yield, the phases of all emitting atoms must be matched for constructive interference.

The basic description of the harmonic generation process in an extended nonlinear

medium starts from the wave equation [L'H91, L'H92]:

$$\vec{\nabla}^2 \mathcal{E} - \frac{1}{c^2} \frac{\partial^2 \mathcal{E}}{\partial t^2} = \frac{4\pi}{c^2} \frac{\partial^2 \mathcal{P}}{\partial t^2} \quad (2.30)$$

$$\xrightarrow{\mathcal{FT}} \quad \vec{\nabla}^2 \mathcal{E}_q + \left(\frac{q\omega}{c}\right)^2 \mathcal{E}_q = -4\pi \left(\frac{q\omega}{c}\right)^2 \mathcal{P}_{\text{tot},q}, \quad (2.31)$$

where the total electric field \mathcal{E} and the polarization \mathcal{P} are considered as a superposition of all contributing frequencies:

$$\mathcal{E}(\vec{r}, t) = \text{Re} \left\{ \sum_q \mathcal{E}_q(\vec{r}, t) \cdot e^{-iq\omega t} \right\}, \quad \mathcal{P}(\vec{r}, t) = \text{Re} \left\{ \sum_q \mathcal{P}_{\text{tot},q}(\vec{r}, t) \cdot e^{-iq\omega t} \right\}. \quad (2.32)$$

For the process of high-order harmonic generation, the conversion efficiencies of frequencies $q\omega$ remain weak, so that only the polarization induced by the fundamental field contributes as a source to the harmonic field. All indirect generation processes (wave mixing) can be neglected [L'H91]. With the same reasoning, depletion of the fundamental field is neglected. Applying these approximations, Eq. (2.31) becomes decoupled [L'H91], and the total polarization $\mathcal{P}_{\text{tot},q}$ of each harmonic q is given by the sum $\mathcal{P}_{\text{tot},q} \approx \mathcal{P}_{\text{lin},q}(\mathcal{E}_q) + \mathcal{P}_q(\mathcal{E}_1)$ of the linear polarization $\mathcal{P}_{\text{lin},q}$, induced by the harmonic field \mathcal{E}_q , and the nonlinear polarization \mathcal{P}_q , induced by the fundamental field \mathcal{E}_1 . For high-order harmonic generation, usually low atomic densities in the nonlinear medium are considered. This allows us to neglect higher-order corrections of the refractive index for the harmonic field [L'H91]. Moreover, nonlinear effects on the propagation of the fundamental field are neglected, such as self-focusing [L'H91, Mar75], defocusing due to free electrons [Bel01, Mon92, Ran91], or a spectral blue shift due to plasma formation [Wah93]. Thus, Eq. (2.31) yields a linear propagation equation for the fundamental field, and an inhomogeneous differential equation for the harmonic fields according to [L'H91]

$$\vec{\nabla}^2 \mathcal{E}_q + k_q^2 \mathcal{E}_q = -4\pi \left(\frac{q\omega}{c}\right)^2 \mathcal{P}_q, \quad (2.33)$$

where the wave vector k_q of the harmonic field includes the linear polarization term. This equation can be written in its integral representation as [L'H91]

$$\mathcal{E}_q(\vec{r}') = \left(\frac{q\omega}{c}\right)^2 \int d^3r \frac{\exp(ik_q |\vec{r}' - \vec{r}|)}{|\vec{r}' - \vec{r}|} \mathcal{P}_q(\vec{r}). \quad (2.34)$$

Since the harmonic field is emitted close to the propagation axis z , the paraxial approximation is applied in the following. Further, the far-field approximation is used, since the field at a reference point \vec{r}' far from the medium ($z' \gg z$) is of interest. Then, the distance between a point in the medium $\vec{r} = (x, y, z)$ and the reference point $\vec{r}' = (x', y', z')$ becomes

$$|\vec{r}' - \vec{r}| \approx z' - z + \frac{(x' - x)^2 + (y' - y)^2}{2(z' - z)}. \quad (2.35)$$

Inserting Eq. (2.35) into Eq. (2.34) yields

$$\mathcal{E}_q(\vec{r}') = \left(\frac{q\omega}{c}\right)^2 \int d^3r \frac{\mathcal{P}_q(\vec{r})}{z' - z} \cdot e^{ik_q(z' - z)} \cdot e^{ik_q[(x' - x)^2 + (y' - y)^2]/2(z' - z)}. \quad (2.36)$$

Introducing slowly varying envelope functions $E_q = \mathcal{E}_q e^{-ik_q z}$ and $P_q = \mathcal{P}_q e^{-iqk_1 z}$ with fundamental wave vector k_1 , and making the assumption of rotational symmetry ($r^2 = x^2 + y^2$), finally yields [L'H91]

$$E_q(r', z') = 2\pi \left(\frac{q\omega}{c}\right)^2 \int dr dz \frac{P_q(r, z) \exp(-i\Delta\Phi_q(r, z))}{z' - z} \times \exp\left(\frac{ik_q(r^2 + r'^2)}{2(z' - z)}\right) J_0\left(\frac{k_q r r'}{z' - z}\right), \quad (2.37)$$

where J_0 denotes the zero-order Bessel function, and $\Delta\Phi_q$ is the complex phase mismatch discussed below.

The complex nonlinear polarization P_q of the high-order harmonics, which is induced in the medium by the fundamental field, can be computed via the single-atom response \ddot{x}_q (cf. Sec. 2.3.2). For a Gaussian beam with confocal parameter b , the nonlinear polarization yields [L'H91]

$$P_q(r, z) = 2\mathcal{N}_{\text{at}}(r, z) \cdot \ddot{x}_q(|\mathcal{E}_1(r, z)|^2) \times \exp\left(-iq\left(\arctan\left(\frac{2z}{b}\right) - \frac{2k_1 r^2 z}{b^2 + 4z^2}\right)\right), \quad (2.38)$$

where \mathcal{N}_{at} denotes the number density of neutral atoms.

The derivation above is performed for a static fundamental electric field. Assuming a laser pulse with slowly varying temporal envelope, the time dependence of the functions ($E_1, P_q, E_q, \Delta\Phi_q, \dots$) can be included quasi-statically. Integration of Eq. (2.37) over the time t and the detector plane in the far field at a distance z' , yields the number $N_{\text{ph},q}$ of generated photons for the q th harmonic [L'H91]:

$$N_{\text{ph},q} = \frac{c}{4\hbar q\omega} \int dr' dt r' |E_q(r', z', t)|^2. \quad (2.39)$$

The complex phase mismatch $\Delta\Phi_q$ in Eq. (2.37) is given by the integral [L'H91]

$$\Delta\Phi_q(r, z) = \int_{-\infty}^z dz'' \Delta k_q(r, z'') - i \int_z^\infty dz'' \kappa_q(r, z'') \quad (2.40)$$

with the imaginary part of the refractive index κ_q accounting for absorption. The dispersion between the fundamental field and the harmonic field is considered by the phase-matching vector Δk_q with contributions that will be discussed in the following section. For a constant dispersion and without absorption, the complex phase mismatch reduces to $\Delta\Phi_q(z) = \Delta k_q z = (k_q - qk_1)z$ with the harmonic wave vector k_q and the polarization wave vector qk_1 .

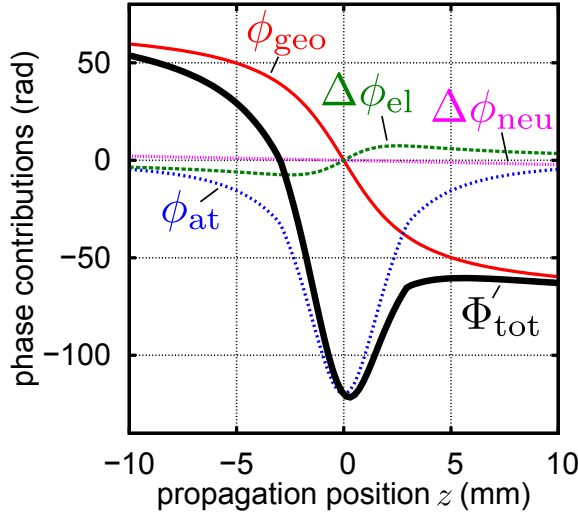


Figure 2.10: On-axis phase contributions versus propagation axis for phase matching of the 45th harmonic in 50 mbar neon. A Gaussian beam is assumed with confocal parameter $b = 5$ mm and peak intensity of 6×10^{14} W/cm². The atomic phase ϕ_{at} is computed for the phase slope factors α from Fig. 2.7 (cf. Sec. 2.3.3). A maximum ionization of 5% is considered which is roughly estimated to depend linearly on intensity. The sum of all phase contributions Φ'_{tot} is shown as a thick black line.

2.4.1 Phase contributions

Different phases contribute to the harmonic field E_q generated in the nonlinear medium. The overall photon count of a harmonic depends sensitively on how fast these phases are varying in the medium. The integral in Eq. (2.37) contains the contributing phase terms in the nonlinear polarization P_q (cf. Eq. (2.38)) and in the phase mismatch $\Delta\Phi_q$ (cf. Eq. (2.40)). Note that the phase term $\exp(ik_q(r^2 + r'^2)/2(z' - z))$ from the far-field integration varies rather slowly, since $z'' \gg z$ and $r, r' \ll z'$. In the following paragraphs the major phase contributions are introduced. The contributions to the polarization are given by the geometric phase $\phi_{\text{geo},q}$ and the atomic phase $\phi_{\text{at},q}$. The phase mismatch $\Delta\Phi_q = \Delta\phi_{\text{neu},q} + \Delta\phi_{\text{el},q}$ consists of phase contributions from neutral atoms $\Delta\phi_{\text{neu},q}$ and from free electrons $\Delta\phi_{\text{el},q}$. Figure 2.10 shows the according on-axis ($r = 0$) phase contributions versus the propagation axis for an example of HHG in neon discussed below. Thereby, the total phase $\Phi'_{\text{tot},q} = \phi_{\text{geo},q} + \phi_{\text{at},q} + \Delta\phi_{\text{neu},q} + \Delta\phi_{\text{el},q}$ is given by the sum of all contributing phases.

Geometric phase The geometric phase originates from the focusing geometry of the laser beam causing curved wave fronts and the Gouy phase shift [Bal97] which are imposed onto the polarization phase. In Eq. (2.38), the geometric phase is represented by the term

$$\phi_{\text{geo},q}(r, z) = -q \left(\arctan\left(\frac{2z}{b}\right) - \frac{2k_1 r^2 z}{b^2 + 4z^2} \right). \quad (2.41)$$

Atomic phase The phase contribution which differs most from the perturbation regime is an additional phase coming from the single-atom response. In the perturbation regime, a bound electron in the nonlinear medium follows immediately the external driving field, and induces a polarization with no phase delay. Contrary, in the strong-field regime, the electron is ionized by the external field, then propagates, and finally recombines. According to the Lewenstein model, this gives rise to the intensity dependent atomic phase $\phi_{\text{at}}(I)$ (cf. Sec. 2.3.3 for details) which is included in the nonlinear polarization in Eq. (2.38) in the complex dipole acceleration \ddot{x}_q .

Dispersion and absorption from neutral atoms The influence of the neutral atoms is taken into account by a complex phase contribution to $\Delta\Phi_q$, namely,

$$\Delta\phi_{\text{neu},q}(r, z, t) = \int_{-\infty}^z dz'' \Delta k_{\text{neu},q}(r, z'', t) - i \int_z^{\infty} dz'' \kappa_q(r, z'', t), \quad (2.42)$$

where $\Delta k_{\text{neu},q}$ denotes the wave-vector mismatch from dispersion, and κ_q represents the absorption term described below. The mismatch of the wave vectors can be calculated via

$$\Delta k_{\text{neu},q} = k_{\text{neu}}(q\omega) - qk_{\text{neu}}(\omega) \approx \frac{q\omega}{c} (n_{\text{neu}}(q\omega) - 1). \quad (2.43)$$

The refractive index for the fundamental field is approximately 1, whereas the index for the harmonic field can be determined via listed atomic scattering factors $f_{\text{at}}(q\omega)$ [Hen93]

$$n_{\text{neu}}(q\omega) = 1 - 2\pi \left(\frac{c}{q\omega} \right)^2 r_{\text{el}} \cdot \mathcal{N}_{\text{at}} \cdot \text{Re} \{ f_{\text{at}}(q\omega) \}. \quad (2.44)$$

Here, $r_{\text{el}} = \frac{e^2}{4\pi\epsilon_0 m_e c^2}$ denotes the classical electron radius, and \mathcal{N}_{at} is the density of neutral atoms. The imaginary part κ_q of the refractive index can be calculated from the imaginary part of the atomic scattering factors [Hen93]

$$\kappa_q \equiv \kappa(q\omega) = -\frac{4\pi c}{q\omega} r_{\text{el}} \cdot \mathcal{N}_{\text{at}} \cdot \text{Im} \{ f_{\text{at}}(q\omega) \}. \quad (2.45)$$

Dispersion from free electrons Analogous to the dispersion from neutral atoms, the dispersion from free electrons and its resulting phase contribution $\Delta\phi_{\text{el},q}$ can be determined via the refractive index. The approximation of the refractive index of free electrons, Eq. (2.12), according to

$$n_{\text{el}}(q\omega) = \sqrt{1 - \frac{\omega_p^2}{(q\omega)^2}} \approx 1 - \frac{\omega_p^2}{2(q\omega)^2}. \quad (2.46)$$

yields the wave-vector mismatch of

$$\Delta k_{\text{el},q} = \frac{\omega_p^2}{2cq\omega}(q^2 - 1). \quad (2.47)$$

The electron density \mathcal{N}_{el} which determines the plasma frequency $\omega_p \propto \mathcal{N}_{\text{el}}$ (cf. Eq. (2.13)) varies in space and time, and can be computed from the tunnel-ionization rate (cf. Sec. 2.1.2).

Figure 2.10 shows an estimate of the on-axis phase contributions for the 45th harmonic generated in neon. The most important contributions are given by the geometric phase and the atomic phase. The dispersion of neutral atoms may be neglected. Considering a gas with a lower ionization potential than neon (e.g. xenon, cf. Tab. 2.1), also the dispersion from free electrons becomes more important than for the case in Fig. 2.10. The sum of all phase contributions $\Phi_{\text{tot},q}$ is shown as thick solid line in Fig. 2.10. In order to maximize the harmonic yield, the spatial variation $\Delta \vec{k}_{\text{tot},q} = \vec{\nabla} \Phi_{\text{tot},q}$ of the total phase must be minimized. For an estimation of local phase-matching conditions, a characteristic length $L_{\text{coh},q}$ can be introduced, which will be discussed in the following section.

2.4.2 Coherence length

A phase mismatch in harmonic generation gives rise to a periodic build-up and decay of the generated harmonic field in a nonlinear medium. The length over which the yield of a harmonic q increases is called the coherence length⁹

$$L_{\text{coh},q} = \frac{\pi}{|\Delta \vec{k}_{\text{tot},q}|}. \quad (2.48)$$

The total phase-matching vector $\Delta \vec{k}_{\text{tot},q}$ is determined from all contributing phase terms as discussed above in the Sec. 2.4.1. Harmonics generated within the distance of the coherence length $L_{\text{coh},q}$ still interfere constructively, while beyond this length the magnitude of the field starts to decrease due to destructive interference. Thus, it is desirable to use a medium of a length $L_{\text{med}} \approx L_{\text{coh},q}$ close to the coherence length in order to reach the maximum conversion efficiency. In an extended medium larger than the confocal parameter b of the laser beam, the medium length L_{med} should be replaced by the effective length of the medium L_{amp} , over which enough intensity for HHG is available [L'H92]. Note that the value of the coherence length depends on the position in the medium and thus denotes an estimate of the local phase-matching conditions.

⁹Note that the coherence length $L_{\text{coh},q}$ should not be confused with the length over which the radiation is coherent and is able to interfere.

At higher pressure the absorption length becomes important:

$$L_{\text{abs},q} = \frac{1}{2\kappa_q} = \frac{1}{\sigma_q \mathcal{N}_{\text{at}}}, \quad (2.49)$$

where κ_q denotes the absorption coefficient (cf. Sec. 2.4.1) which depends on the ionization cross section σ_q and the atomic density \mathcal{N}_{at} [Con99]. A balance between the medium length, the coherence length, and the absorption length must be found for an optimal yield of harmonics. An optimization rule was found by Constant *et al.* [Con99] using an one dimensional model:

$$L_{\text{med}} > 3L_{\text{abs},q} \quad \text{and} \quad L_{\text{coh},q} > 5L_{\text{abs},q}. \quad (2.50)$$

2.4.3 Phase-matching effects

The interplay between phase contributions from different positions in the nonlinear medium or at different times of the driving pulse give rise to many phenomena in measurements of high-order harmonics. The best studied geometry is the gas jet, where most effects of phase matching have been observed (see [Sal97] for a review). A confined jet allows for a direct estimation of the contributing phases giving rise to phase matching at a certain position. In extended distributions of the nonlinear medium, in contrast, an integration of Eq. (2.37) is necessary for phase-matching considerations. Thus, in the following, phase-matching effects are reviewed for a gas jet geometry.

The yield and the spatial distribution of the generated harmonics substantially depend on the position of the medium with respect to the focus of the fundamental laser beam [Sal95, Sal97]. The solid line in Fig. 2.11(a) shows the conversion efficiency versus the positions of the gas jet with respect to the focus. A maximum conversion efficiency for a jet position $z \approx -1$ mm in front of the focus (with respect to the propagation direction), and a maximum for a jet position $z \approx 3$ mm behind the focus is observed. The conversion efficiency drops when the gas jet is placed close to the focus position. This can be understood when considering the phases contributing to phase matching, introduced in Sec. 2.4.1. The maximum conversion efficiency at $z \approx 3$ mm is caused by good phase-matching conditions on the axis, seen from the low variation of the total phase $\Phi_{\text{tot},q}(z)$ in Fig. 2.10. The maximum at a jet position in front of the focus ($z < 0$) cannot be explained by the rapidly varying total phase on the axis, but it results from off-axis phase matching. The radial intensity profile of the fundamental beam induces a radially varying atomic phase as illustrated exemplarily in Fig. 2.11(b). In addition, the geometric phase has a radial component due to the curved wave fronts of a focused beam. The sum of both phases yields low variations at an off-axis distance of $r \approx 25$ μm . Low phase

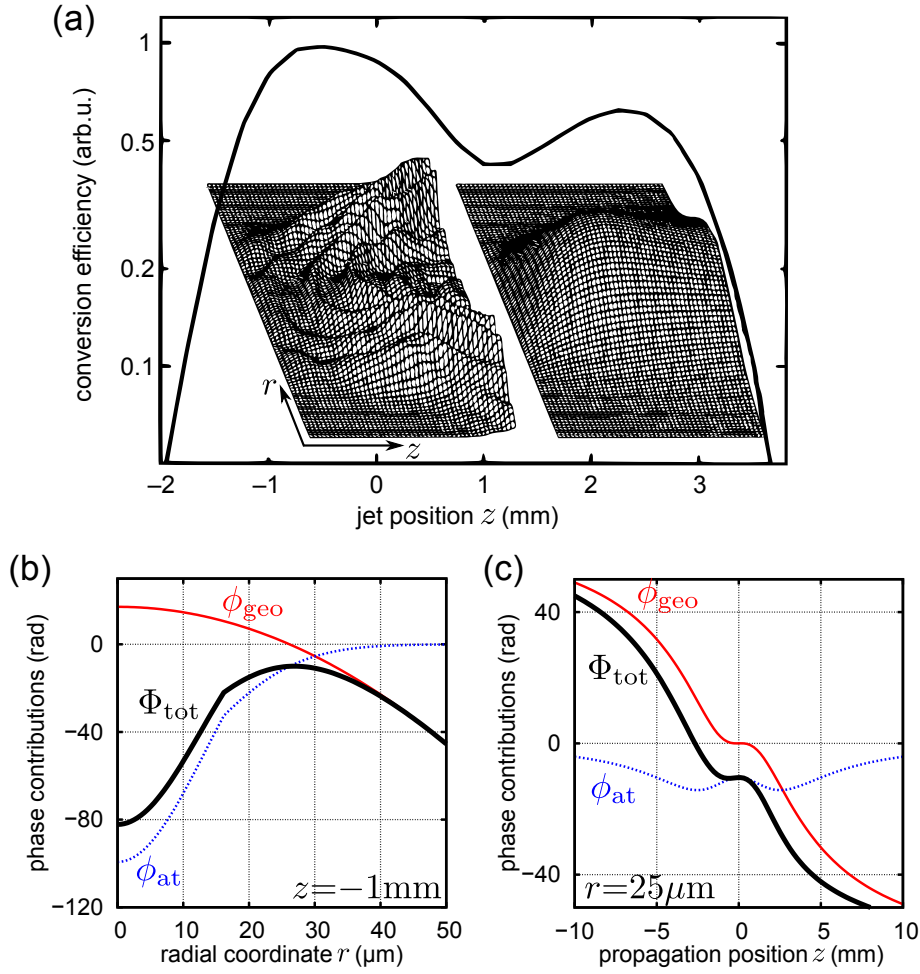
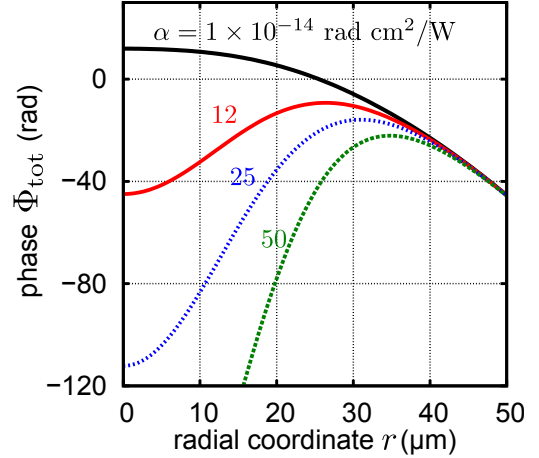


Figure 2.11: HHG in dependence on the medium position. (a) The harmonic conversion efficiency of the 45th harmonic in neon versus the position of the gas jet [after Sal95]. For positions $z < 0$ the gas jet is located before the focus with respect to the propagation direction of the laser. The insets show the harmonic intensity profile versus jet position [after Sal95]. Compare to Fig. 2.10 for the according on-axis phase contributions to phase matching. (b)-(c) Off-axis phase contributions of the geometric and atomic phase for the 45th harmonic in neon versus r at $z = -1$ mm in (b), and versus z at $r = 25 \mu\text{m}$ in (c), calculated for the same conditions as in Fig. 2.10.

variations are also obtained in direction of the propagation axis z at this distance, depicted in Fig. 2.11(c). The off-axis phase matching gives rise to a ring structure in the spatial profile of the harmonic, which is shown in the insets of Fig. 2.11(a).

Phase matching can also select different trajectories that contribute to HHG. Salières *et al.* [Sal98] demonstrated that the trajectories with short traveling time are favored for on-axis phase matching after the focus, due to their weak intensity dependence (α_{short}). For example in Fig. 2.10, the low variations of the total phase at

Figure 2.12: Total phase for off-axis phase matching for different phase slopes α . Note that an equal value of α is assumed in the plateau and cutoff. Phase contributions from dispersion and free electrons are not considered. (Conditions as in Fig. 2.10).



$z \gtrsim 3 \text{ mm}$ are a result from the smaller phase slope factor α used in the cutoff region with a single contributing trajectory. At a jet position in the focus or in front of the focus, the long trajectories are dominant. The higher phase slope factors α_{long} are the reason for the off-axis phase matching in this region [Gaa02]. Figure 2.12 shows calculations of the off-axis total phase for different phase slope factors α . It can be seen that the off-axis region of low phase variation shifts to higher distances r from the axis with increasing slope factor α .

In the far field, different slope factors α cause that harmonic radiation is emitted with a divergence angle θ according to $\theta \propto \alpha$, derived in a geometrical optics approximation [Gaa02]. Thus, also in the far field, an off-axis contribution in the harmonic beam profile corresponds to the long trajectory, while the on-axis radiation is dominated by the short trajectory contribution [Bel98].

Beside spatial phase matching, the phase contributions may vary in time due to the intensity envelope of the driving pulse resulting in transient phase-matching phenomena. This occurs in ionizing media at intense driving pulses [Wan00, Zho00] and gives rise to the *adiabatic* spectral splitting and blue shift. Different from the non-adiabatic effects due to the rapidly varying atomic phase $\phi_{\text{at},q}$ (cf. Sec. 2.3.3), the adiabatic effects are caused by the rapidly changing phase induced by free electrons $\Delta\phi_{\text{el},q}$. During the rising edge of the pulse, the medium gets strongly ionized yielding a time dependent density of free electrons. This in turn results in a rapidly changing index of refraction. Figure 2.13 shows exemplarily the temporal evolution of the wave-vector mismatch $\Delta k_q = \partial\phi_q/\partial z$, in order to demonstrate the rapidly changing on-axis phase-matching conditions. Beside the geometric and the atomic contribution, the wave-vector mismatch from the free electrons gains influence due to ionization at the raising edge of the pulse. The total wave-vector mismatch vanishes at two instances in time where good phase-matching conditions are obtained. Due to the monotonically varying phase contribution from free electrons, new higher frequency components are generated, similar to SPM (cf. Sec. 2.1.1). Thus, the

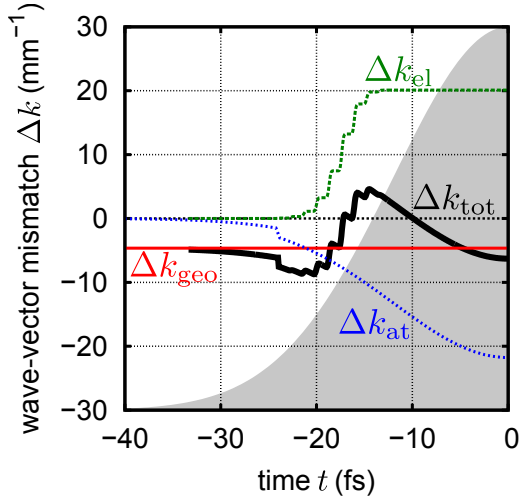


Figure 2.13: Transient phase matching. Temporal evolution of the on-axis wave-vector mismatch $\Delta k_q = \frac{\partial \phi_q}{\partial z}$ for the 19th harmonic in 20 mbar xenon at $z = -2$ mm with arbitrarily chosen parameters¹¹ for the sake of demonstration. The shaded background indicates the intensity of driving laser field.

harmonic emission is strongly chirped¹⁰ and the temporal selection by transient phase-matching results in a split and blue-shifted harmonic spectrum. Figure 2.14(a) shows the temporal evolution of the envelope of the driving field and the envelope of the 19th harmonic in xenon, calculated by Zhong *et al.* [Zho00]. In addition, the density of free electrons is depicted, which increases rapidly during the pulse and gives rise to a chirp and the double peak temporal structure of the 19th harmonic. Consequently, the spectrum of the harmonic features a splitting as well as a blue shift [Alt99, Wan00, Zho00]. In contrast to the non-adiabatic spectral splitting from the single-atom effect (cf. Sec. 2.3.3), the adiabatic spectral splitting depends on the gas pressure, as shown in Fig. 2.14(b). The gas pressure determines the density of free electrons which in turn influences the phase contribution ϕ_{e1} of free electrons.

2.4.3.1 Coherence properties

The coherence of high-order harmonic radiation is a necessary feature for attosecond pulse generation. The degree of coherence between any two points A and B is computed by the normalized correlation function [Sal97]

$$\gamma_{q,AB}(\tau_d) = \frac{\langle \mathcal{E}_{q,A}(t - \tau_d) \mathcal{E}_{q,B}^*(t) \rangle}{\sqrt{\langle |\mathcal{E}_{q,A}| \rangle \langle |\mathcal{E}_{q,B}| \rangle}}, \quad (2.51)$$

¹⁰Note that the harmonic emission is also chirped due to the intensity-dependent atomic phase [Alt98].

¹¹The transient phase-matching vector is calculated for a Gaussian pulse with duration of 30 fs and center wavelength of 780 nm occurring in a Gaussian beam with confocal parameter of $b = 5$ mm and peak intensity of $I_0 = 6 \times 10^{14}$ W/cm². The ionization rate is calculated according to Sec. 2.1.2. The atomic phase dependence is chosen to $\alpha^{\text{cutoff}} = 13 \times 10^{-14}$ rad cm²/W below a cutoff intensity of $I^{\text{cutoff}} = 0.5 \times 10^{14}$ W/cm² and $\alpha^{\text{plateau}} = 25 \times 10^{-14}$ rad cm²/W above.

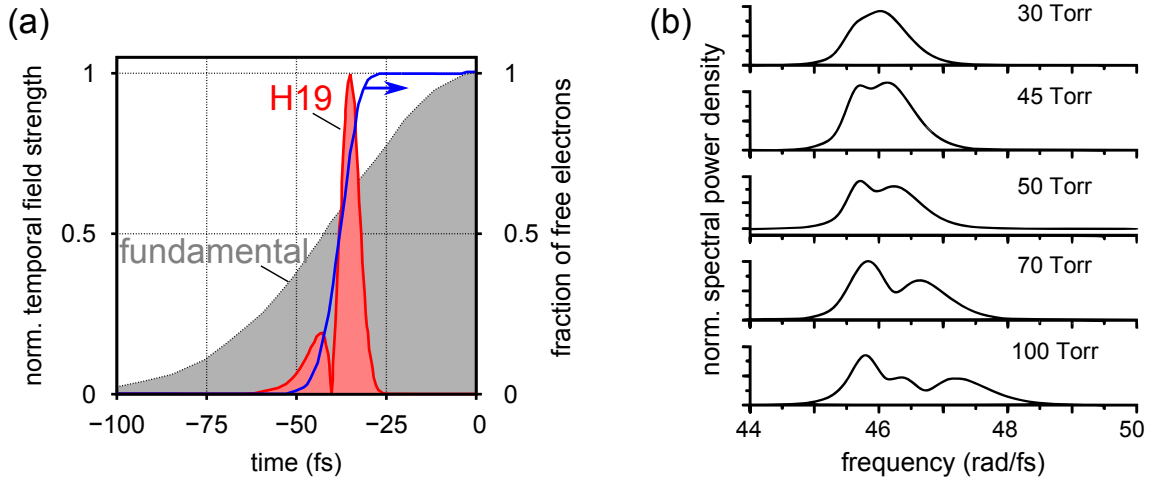


Figure 2.14: Adiabatic spectral splitting due to transient phase matching [after Zho00]. (a) Simulated time evolution of generated field (red filled curve) of the 19th harmonic in 50 Torr argon from a 50-fs-pulse of peak intensity of $1 \times 10^{15} \text{ W/cm}^2$. The filled gray curve indicates the intensity of the fundamental pulse, and the blue curve (right axis) shows the fraction of free electrons versus time. (b) Spectral splitting of the 19th harmonic at different argon pressures for the same conditions as in (a). [after Zho00]

where the angle brackets denote an average over the time t . $\mathcal{E}_{q,A}$ and $\mathcal{E}_{q,B}$ are the complex electric field amplitudes of harmonic order q at the two points of interest, which are delayed by the time τ_d . The quantity $|\gamma_{q,AB}(\tau_d)|$ is a measure for the ability of the two fields to interfere with each other. In an experiment, the coherence properties can be observed via interference fringes in the harmonic spatial profile. The fringe visibility is defined by the contrast between the maximum and the minimum intensity of an interference pattern [Bel98]:

$$V = \frac{I_{\max} - I_{\min}}{I_{\max} + I_{\min}}. \quad (2.52)$$

The degree of coherence is distinguished with respect to space and time. While the spatial coherence $|\gamma_{q,AB}(0)|$ is determined by the variation of the distance between A and B at $\tau_d = 0$, the temporal coherence is considered at fixed locations of the harmonic sources for a varying delay τ_d . The coherence time $T_{\text{coh},q}$ is defined by the FWHM of the temporal correlation function $|\gamma_{q,AB}(\tau_d)|$. Since the temporal correlation function constitutes the Fourier transform of the power spectrum of the q th harmonic [Lyn99], the coherence time is directly linked to the spectral bandwidth $\Delta\omega_q \propto 1/T_{\text{coh},q}$ of the harmonic. This, in turn, is influenced by the intensity dependent phase (cf. Sec. 2.3.3), having a steeper slope α_{long} for the long trajectories than for the short ones (α_{short}). As a consequence, the harmonic radiation dominated by the long trajectory features a shorter coherence time than the radiation domi-

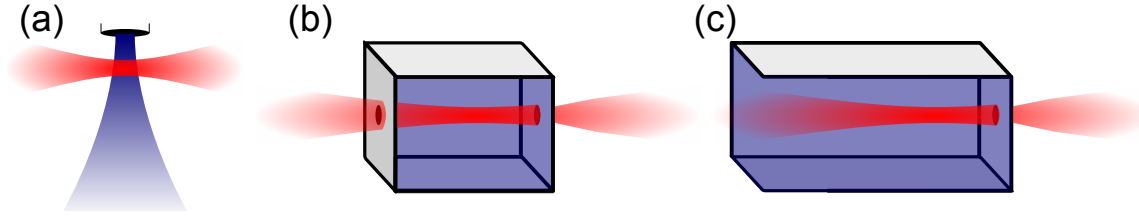


Figure 2.15: Standard geometries: (a) The *gas jet* is the most frequently used geometry for HHG. It features a small interaction region which confines the origin of HHG in the focus region. (b) The *finite gas cell* is defined by a gas filled container bounded by two pinholes for the laser transmission. (c) The *semi-infinite gas cell* (SIGC) consists of an entrance window, which is far from the interaction region, and a pinhole terminating the cell.

nated by the short trajectory:

$$T_{\text{coh},j} \propto 1/\Delta\omega_j \propto 1/\alpha_j, \quad (2.53)$$

where the index j denotes the dominating quantum path. This can be exploited to identify the dominating trajectory contribution in the spatial harmonic profile by local measurement of the coherence time. Bellini *et al.* [Bel98] performed measurements of the coherence time for a gas jet in an on-axis region, which they identified as contributions from the short trajectory, and in an off-axis region, which was assigned to the long trajectory. Analogously, this method will be applied to HHG in a SIGC for identification of trajectory contributions in the spatial harmonic profile (cf. Chapter 3).

2.4.4 Geometries

Phase matching is greatly influenced by the chosen geometry, i.e. by the density distribution of the nonlinear medium. The geometry defines, on the one hand, the location of the sources for the nonlinear polarization, and thus, limits the spatial region of the integral in Eq. (2.38). On the other hand, it determines the dispersion and its resulting phase contributions. In the following sections, the main geometries are introduced as sketched in Fig. 2.15.

Gas jet The gas jet is the most common and best studied geometry for HHG [Sal97]. Its density distribution can be estimated by a Lorentzian profile [Alt96] which features a spatial confined interaction region. Even for relatively tight focusing conditions, the extent of the medium (in the order of 800 μm FWHM width [Sal97]) is small or comparable to the confocal parameter. This is a benefit for phase matching,

because positions of the jet with respect to the focus can be found, where the phase variation is small over the propagation distance. Moreover, the confined interaction range permits the investigation of HHG under consideration of *local* phase-matching conditions. For higher conversion efficiencies, a moderate pressure of tens of mbar in the interaction volume is required, which is achieved by a high backing pressure of several bar [Alt96]. This is accompanied by a high gas flow into the vacuum which can be reduced by using a pulsed gas jet. The best conversion efficiencies with this setup are measured in the plateau region in xenon to 10^{-5} [Her02]. In argon and neon the conversion efficiency reaches 7×10^{-6} and 10^{-7} , respectively.

Finite gas cell The finite gas cell comprises a relatively compact interaction volume which consists of a closed chamber with two pinholes where the laser passes through. These pinholes can be laser-drilled for a alignment-free setup. It permits a relatively high atomic density within the cell without the need for complex pulsing mechanisms as required for the jet. Due to its extended selectable interaction length and higher possible pressure, this geometry is suited for high conversion efficiencies reaching up to 4×10^{-4} in xenon [Tak02], 1.5×10^{-5} in argon [Tak02], and 5×10^{-7} in neon [Tak04].

The semi-infinite gas cell The semi-infinite gas cell (SIGC) is one of the simplest geometries regarding their setup and alignment [Pap01]. It consists of a gas-filled cell with an entrance window, which is far from the interaction region to avoid nonlinear effects, and an exit pinhole to couple out the radiation. Since the exit pinhole is laser-drilled before an experiment, the SIGC is alignment free with only one transition to vacuum in contrast to the finite gas cell. It features the advantages from the finite gas cell permitting a relative high pressure of a few hundred millibars and high conversion efficiency measured up to 10^{-4} in argon [Bri09]. In contrast to a gas jet, the pressure in the interaction region is accurately known and can be well controlled. The phase-matching and coherence properties in this geometry are poorly studied so far, and will be investigated systematically in Chapter 3.

Chapter 3

High-order harmonic generation in a semi-infinite gas cell

In this Chapter, a systematic study on experimental HHG in a SIGC is presented [Ste09b]. The experimental results are compared to phase-matching simulations including the single-atom response.

In the last part of this Chapter, the study is extended into the few-cycle regime by generating high-order harmonics with ultra-short pulses after a filamentation stage [Ste09a].

3.1 Phase-matching experiments

While phase matching in a gas jet geometry is well investigated (see Sec. 2.4.3 and review [Sal97]), the SIGC geometry is rarely studied. First experiments on the SIGC were performed by Papadogiannis *et al.* [Pap01] in 2001. They investigated this geometry for phase matching in krypton and argon at selected parameter values regarding the focus position, input intensity, and gas pressure. The performance of the SIGC was found to be comparable to other sources with the advantage of its compactness and versatility. Peatross *et al.* [Pea04] and Sutherland *et al.* [Sut04] investigated the effect of an aperture, which was placed before the focusing lens, on HHG in a SIGC. Similar to results in a finite gas cell [Kaz02], they found an increase of the conversion efficiency, as well as an extension of the generated harmonic cutoff for a truncated beam due to improved phase-matching conditions. Recently, the generation of a few phase-matched high-order harmonics in a SIGC was published [Tei09, VD08]. Also a comparative study on conversion efficiencies in different sources [Bri09] demonstrated that the SIGC is a promising geometry for generation

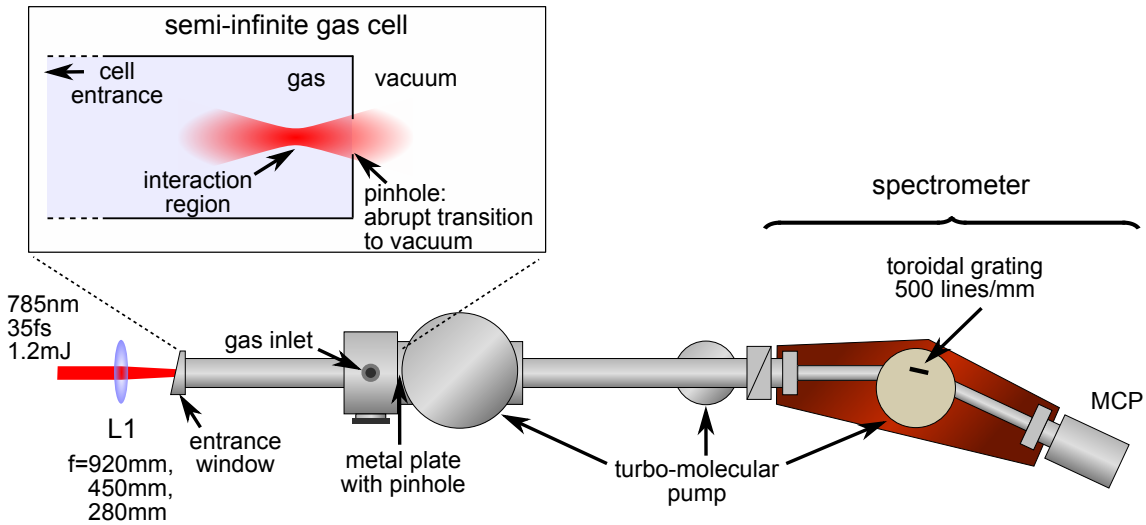


Figure 3.1: Experimental setup for phase-matching investigations of HHG in a SIGC. The inset describes the principle of the SIGC. (See text for details.)

of high-order harmonics with high photon flux and a conversion efficiency of up to 10^{-4} in argon.

In order to gain more insights into the phase-matching properties of the SIGC, a systematic investigation on different parameters of direct impact on phase-matching conditions is performed [Ste09b]. In the following subsections, the influence of the focus position is studied, which is changed with respect to the exit pinhole of the SIGC. Thereby, different focal lengths and two noble gases, xenon and helium, are applied. Next, the pressure in the SIGC is varied. The experimental results are compared to simulations which account for HHG as well as propagation effects. A good agreement is obtained by the use of a genetic fitting algorithm to optimize selected parameters of the input laser pulse. Investigations on the spatial profiles of individual harmonics are performed, and different quantum path contributions are identified by exploiting coherence properties of the harmonic radiation. Finally, effects of adiabatic as well as non-adiabatic spectral splitting and blue shift in the harmonic spectral profiles are shown.

3.1.1 Experimental setup

The experimental setup is sketched in Fig. 3.1. The amplified laser pulses (see Appendix A.1) with duration of 35 fs, energy of 1.2 mJ, and center wavelength of 785 nm are focused with lens L1 into the SIGC. Lenses of different focal lengths ($f = 280$ mm, 450 mm, 920 mm) are applied to investigate different phase-matching conditions. Depending on the lens, the length of the SIGC ranges from 20 cm to

70 cm. An abrupt transition to vacuum is realized by a laser-drilled pinhole (diameter¹ $\lesssim 500 \mu\text{m}$) in a metal plate, which can be replaced quickly by a screwable adapter plate. Since the distance between the focusing lens and the transition pinhole needs to be adjusted for investigation of different phase-matching conditions, the focusing lens is mounted onto a manual translation stage. The SIGC can be filled with different gases or mixtures of gases. In the following, xenon and helium are considered. The pressure is measured using a piezo-resistive gauge (GDH 14 AN, Greisinger electronics) with 1 mbar resolution. After the SIGC and a propagation distance through vacuum, the generated radiation is detected with a scanning XUV monochromator (LHT 30, Horiba-Jobin-Yvon). The entrance and exit slits of the spectrometer are chosen for high resolution with diameter of $250 \mu\text{m}$. Via a multi-channel plate (MCP), a lock-in amplifier, and a computer, the harmonic signal is recorded.

Setup for measurement of harmonic profiles and trajectory contributions

To measure the harmonic spatial profiles (cf. Sec. 3.1.4), a lens L1 with $f = 500 \text{ mm}$ focal length is applied to generate high-order harmonics in xenon. Instead of the compact XUV monochromator LHT 30 (see above), a home-built Seya-Namioka-type spectrometer [Nam59a, Nam59b, Nam59c] (toroidal grating: 600 lines/mm, 1.5 m focal length) with a large aperture is used. The grating is placed at a distance of about 1.2 m from the exit pinhole of the SIGC and separates the different harmonic orders over the wavelength in the horizontal plane, while the vertical beam profile is maintained. In order to record the full harmonic beam profile, the entrance slit and the exit slit of the spectrometer are removed. The harmonic radiation is detected via an MCP with phosphor screen and a charge-coupled device (CCD) camera (C4742-95-12NRG, Hamamatsu Photonics K.K).

Before the focusing lens L1, a Mach-Zender interferometer is installed for the measurement of the coherence time of the generated harmonic radiation. By misalignment of one arm of the interferometer, two focal points with a distance² of about $130 \mu\text{m}$ to $300 \mu\text{m}$ are realized in the SIGC which serve as two sources for harmonic generation each with an intensity of about $2.5 \times 10^{14} \text{ W/cm}^2$ (cf. [Bel98, Lyn99] for a similar experiment). The beam waist in the focus is estimated to $38 \mu\text{m}$. Thus, both sources are well separated. In the far field, the generated harmonics from both sources interfere leading to fringes in their spatial profile, which is recorded as described above.

¹Note that the diameter of the pinhole is enlarged on e.g. moving the focus position. Constant conditions for HHG are obtained after a couple of minutes or by moving the focus position before the start of an experiment.

²The distance of the focal points is measured via the distance of the laser-drilled pinholes in the metal plate which terminates the SIGC.

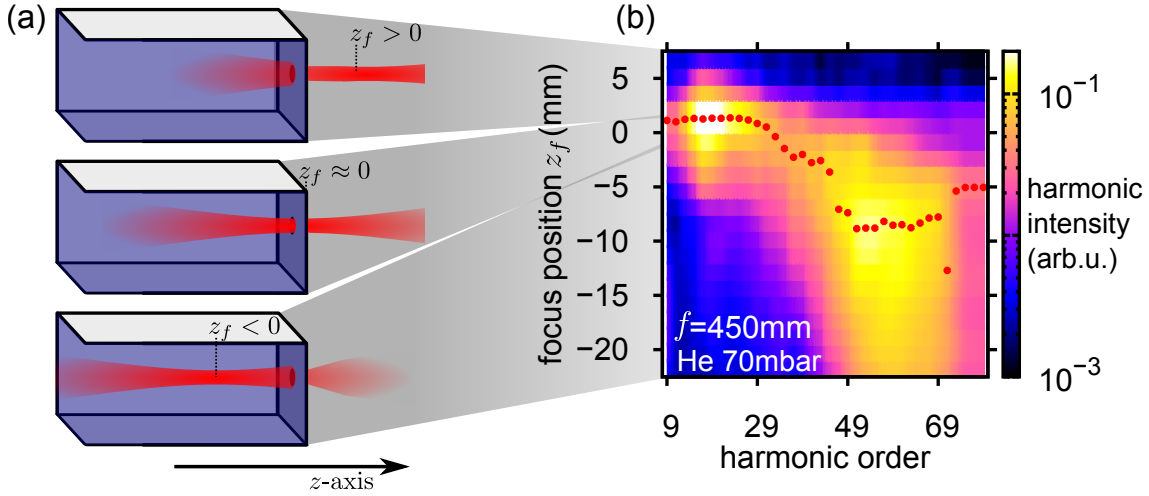


Figure 3.2: Dependence of the harmonic yield on the focus position. (a) Sketch of the nomenclature of the focus position. The gray shaded background indicates the covered range of the z_f -axis in (b). (b) Measured harmonic peak intensity versus harmonic order and focus position. The map shows HHG in 70 mbar helium using a lens with $f = 450$ mm focal length. The red points (\bullet) indicate the maximum intensity versus focus position at a specific order. The color scale encodes the spectral power density of the individual harmonic orders in arbitrary units. Note that the map is interpolated with two points between each focus position for better visualization.

3.1.2 Dependence on focus position

The phase-matching effect from different focus positions is investigated experimentally by changing the distance between the focusing lens and the exit pinhole of the SIGC. The position z_f denotes the position of the focus relative to the exit pinhole. It is determined roughly by eye and then fitted against the simulation results. A position $z_f < 0$ refers to a focus position within the gas cell, while for $z_f > 0$ the focus is placed outside the SIGC in the vacuum (see Fig. 3.2(a)).

In Fig. 3.2(b), the spectral power density at the harmonic orders versus the position of the focus for a lens with focal length of $f = 450$ mm is plotted in a logarithmic color map. The red points (\bullet) show the location of the maximum intensity of a harmonic order over the focus position. Two regions of efficient HHG can be identified. In the first region at focus positions $z_f \approx 1$ mm slightly in the vacuum chamber, lower harmonic order up to the 31st are phase-matched, while higher orders are not generated significantly. The second region with maximum conversion efficiency around the 53rd harmonic, is located at negative z_f ($z_{f,\text{max}} \approx -7.5$ mm), thus for a focus within the SIGC. Here higher orders are generated phase-matched while lower harmonic orders vanish. A minimum conversion for all orders is observed at $z_f \approx 0$ where the focus is located at the pinhole. The harmonic yield versus focus

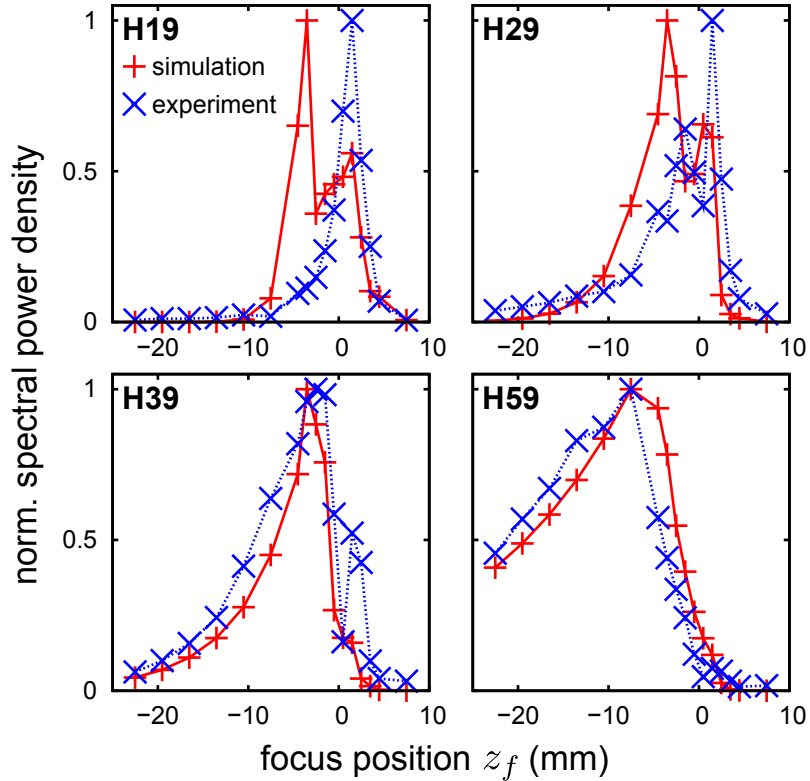


Figure 3.3: Harmonic yield of selected harmonic orders in helium versus focus position. The normalized harmonic intensity from the measurement (\times) and from the simulation ($+$) at selected harmonic orders (as labeled) are shown versus focus position for the same conditions as in Fig. 3.2(b). The lines serve as a guide to the eyes.

position for selected harmonics is shown in Fig. 3.3. For example, the 19th harmonic is only generated for a focus position outside the SIGC, while the 29th and the 39th harmonic exhibit a double peak structure with a minimum around $z_f \approx 0$ mm. Harmonic 59 is only generated within the SIGC.

Along the experimental data, the results from a phase-matching simulation are presented in Fig. 3.3. The simulations are performed in a paraxial approximation described in Sec. 2.4, assuming a Gaussian temporal and spatial profile of the fundamental laser field. Pulses with 30 fs pulse duration centered around 800 nm with energy of 1.2 mJ are used for the driving laser field. According to Eqs. (2.39) and (2.37), the harmonic field for each order q is calculated in the far field at a distance of $z' = 1$ m from the pinhole by integration over a radial coordinate $r' \leq 100 \mu\text{m}$ with $5 \mu\text{m}$ resolution. The temporal integration is performed with a resolution of 3 fs in a time window of 60 fs. In the medium, the integration is computed from a z -position of -100 mm, where harmonic generation is negligible, up to the position $z = -z_f$ denoting the end of the SIGC (see below in Fig. 3.2). The radial

coordinate is integrated with $1\ \mu\text{m}$ resolution in the range $r \leq 200\ \mu\text{m}$ exceeding the beam waist by approximately a factor of 4. As introduced in Sec. 2.4.1, the simulation includes dispersion from neutral atoms and free electrons, as well as absorption from neutral atoms. The density of neutral atoms and free electrons is calculated applying the Ammosov-Delone-Krainov (ADK) ionization rate [Amm86] as described in Sec. 2.1.2. The complex nonlinear polarization P_q is determined via Eq. (2.38) by precomputing the complex dipole response \tilde{x}_q of a harmonic order q versus the fundamental intensity using the Lewenstein-model [Lew94, Lew95] (cf. Sec. 2.3.2). The offset of the experimental z_f -axis, the exact focal length f , the M^2 -value, and the waist w_0 of the input laser beam, which are not accurately known in the experiment, were adjusted to reproduce the experimental data using a genetic fitting algorithm (cf. Appendix B.1). The algorithm converged for $f = 451\ \text{mm}$, $M^2 = 1.42$, and $w_0 = 5.2\ \text{mm}$, which are values very close to the experimental conditions. The calculated harmonic yield of the harmonic orders reproduces the experimental data, as shown in Fig. 3.3. In agreement with the experiment, in the simulation low harmonic orders are generated merely at focus positions outside the SIGC, whereas higher orders are most efficiently generated for positions inside the SIGC. Around the pinhole position, a minimum of the conversion efficiency is visible. Different to the experiment, the simulation overestimates the harmonic yield for lower orders at a focus positions $z_f \approx -3.5\ \text{mm}$ in the SIGC. A possible explanation is given below.

The characteristics of the measured and simulated harmonic intensity map versus focus position can be explained by phase matching as well as absorption in the helium gas. For the higher harmonic orders, the intensity, which is strong enough for the generation of these orders, is confined in a narrow volume around the focus. This effective interaction volume³ V_{eff} must be located inside the medium, which explains the absence of higher harmonic orders for the focus located outside the SIGC ($z_f > 0$). For lower orders, V_{eff} is enlarged, enabling the generation of harmonics as long as this volume is partially located inside the SIGC (cf. the 19th and 29th harmonic in Fig. 3.3). Deep inside the SIGC ($z_f < 0$), absorption determines the harmonic yield. Figure 3.4(a) shows the calculated transmission of XUV radiation as a function of the propagation distance in 70 mbar helium, computed via atomic scattering factors as described in Sec. 2.4.1. Moving the focus inside the SIGC, the generated harmonics suffer losses during the propagation towards the pinhole. This results in the characteristic decrease of the conversion efficiency for all harmonic orders with decreasing z_f . As a consequence of the high absorption of lower harmonic orders, a rapid decay of the harmonic yield is observed, while the decay is slower for higher orders (cf. Fig. 3.3). The low conversion efficiency of all harmonic orders at $z_f \approx 0$, is explained by phase-matching considerations. Fig-

³Compare with L_{amp} in Sec. 2.4.2

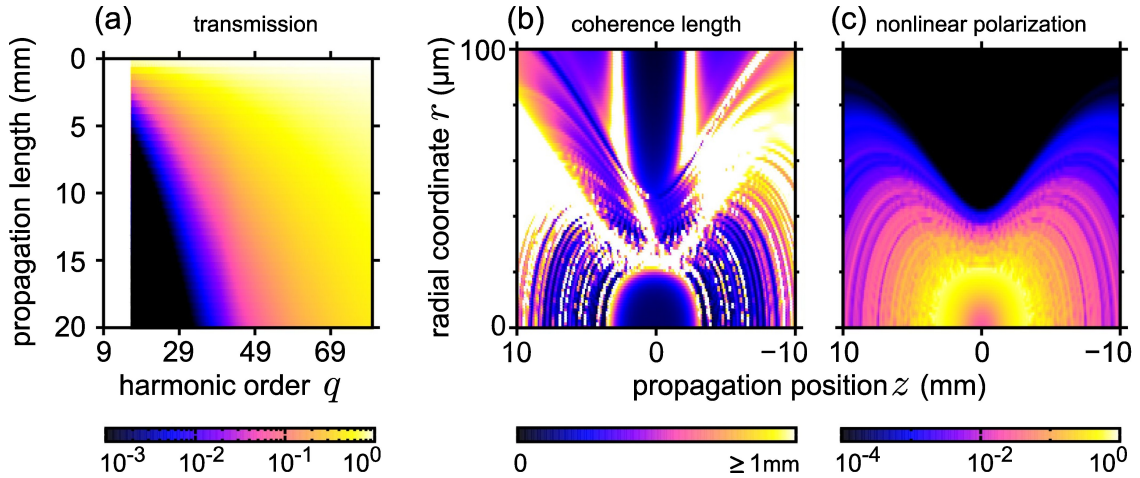


Figure 3.4: Phase-matching considerations for a variation of the focus position. (a) Transmission through helium at 70 mbar versus propagation distance and harmonic order. (b) Coherence length $L_{\text{coh},q}(r, z)$, and (c) the normalized nonlinear polarization $|P_q(r, z)|$ of the 19th harmonic over the coordinate space (r, z) in a local frame around the focus at $z = 0$. Note that a focus position z_f in the laboratory frame with respect to the pinhole corresponds to harmonic generation in the half space $z \leq -z_f$. Thus, the z -axis in (b) and (c) is shown in reverse order to allow for direct comparison with Fig. 3.3. The simulation conditions are the same as in Fig. 3.3.

Figure 3.4(b) shows exemplarily the coherence length $L_{\text{coh}}(r, z)$ of the 19th harmonic over the coordinate space (cf. Sec. 2.4.2). The corresponding nonlinear polarization is shown in Fig. 3.4(c). Directly in the focus, the coherence length exhibits a minimum corresponding to a high phase mismatch. This phase mismatch originates from the rapid variations of the geometric phase and the atomic phase close to the focus, similar to considerations in a gas jet [Sal95, Sal97]. In addition, a high ionization rate around $z = 0$ results in phase contributions from free electrons, and a lower number of atoms generating the harmonics, which causes a decrease of the nonlinear polarization. The overestimated harmonic yield of lower orders at $z_f \approx -3.5$ mm in the SIGC (cf. Figs. 3.3(a) (b)) might be explained by the approximation of an abrupt transition into vacuum at the end of the SIGC while in the experiment a gradient is formed. This gradient results in additional absorption of the generated radiation in the experiment, which is significant for lower orders.

To summarize, it was shown that the higher order harmonics in helium are generated for a focus position inside the SIGC, whereas the lower harmonic orders are generated most efficiently for a focus located slightly outside the SIGC. By comparison to numerical simulations, a decrease of the harmonic conversion efficiency for $z_f < 0$ was attributed to absorption, and for $z_f > 0$ to the decreasing effective interaction volume. The minimum conversion efficiency around $z_f \approx 0$ is attributed to high

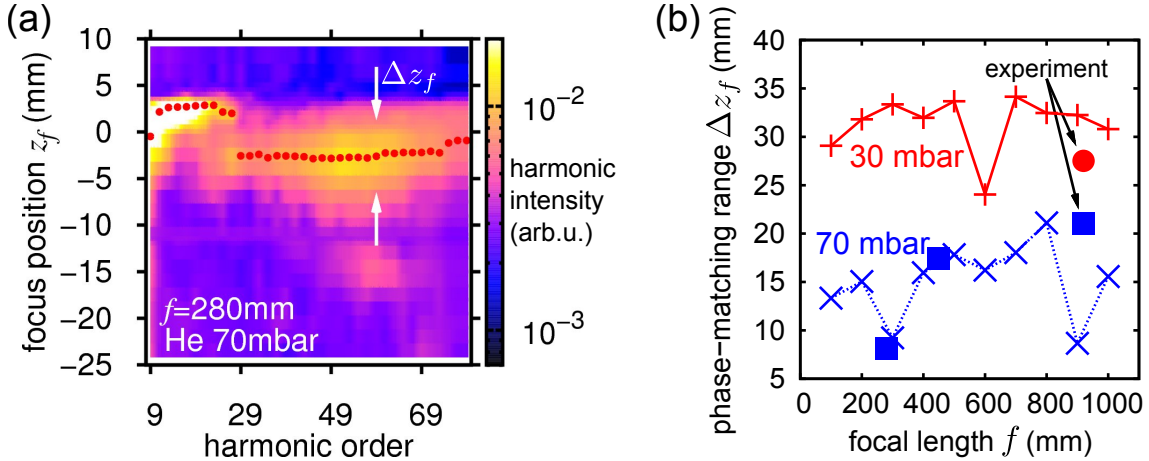


Figure 3.5: HHG in helium at different focal lengths. (a) Measured harmonic spectral map at focal length $f = 280$ mm. The color scale encodes the spectral power density of the individual harmonic orders in arbitrary units. The red points (\bullet) indicate the focus position of the maximum intensity. For the 59th harmonic, the phase-matching range is shown by the white arrows. (b) Simulated ($+$, \times) and experimental (\bullet , \blacksquare) phase-matching range Δz_f (see text) of the 59th harmonic versus focal length f at two different pressures. The lines serve as a guide to the eyes.

phase variations close to the focus and a decreased nonlinear polarization due to ionization at this position. This is similar to considerations for a gas jet [Sal95, Sal97], where also a minimum of the conversion efficiency is observed when placing the jet close to the focus. This minimum is explained by the same argument of rapid phase variations [Sal97].

Different focal lengths The maps of the harmonic spectrum versus focus position are recorded for different focal lengths while the pulse energy is kept approximately constant. Figure 3.5(a) shows the map of the harmonic yield versus focus positions for a lens with focal length of $f = 280$ mm. The characteristic features are similar to the observed ones in Fig. 3.2 for a focusing lens with $f = 450$ mm. The lower order harmonics are generated preferably for a focus position outside the SIGC ($z_f > 0$), while higher orders are efficiently generated for $z_f < 0$. Also the influence from absorption is observable. The overall yield of this short focusing condition is decreased in comparison with the looser focusing condition, as can be seen from the color scale in Figs. 3.5(a) and 3.2(b), respectively. This trend is confirmed by measurements using a lens with focal length of $f = 900$ mm (not presented). As a consequence, the range of focus positions z_f , where harmonic radiation is efficiently generated, appears to be smaller for the shorter focal length (cf. Fig. 3.5(a)). While this is true with regard to the absolute conversion efficiency, the range regarding the

relative yield remains similar for the considered focal lengths, as discussed in the following. For a quantitative estimation, the phase-matching range Δz_f is introduced as the width of the z_f -range where the intensity of a harmonic is higher than half of its maximally reached intensity. In Fig. 3.5(a), the white arrows indicate exemplarily the phase-matching range for the 59th harmonic order. Both experimental and calculated phase-matching ranges Δz_f of the 59th harmonic are shown in Fig. 3.5(b) versus focal length for two different pressures. For all experimental points, the input laser power is approximately constant. The simulations are performed under the same conditions as above while changing the focal length f . It can be observed that the phase-matching range Δz_f remains relatively constant for a variation of the focal length f . This can be explained as following. Moving the focus out of the SIGC (increasing z_f), the harmonic intensity is reduced, since the effective interaction volume is shifted out of the medium. This decay of the harmonic intensity is very rapid (cf. Fig. 3.3), and thus, has minor impact on the phase-matching range for the considered conditions. When moving the focus into the SIGC (decreasing z_f), the harmonic intensity decreases due to absorption, independently from the chosen focal length. At both presented pressures, the decrease from absorption is slow and determines the phase-matching range, which in turn is approximately constant for different focal lengths. A significant enhancement of the phase-matching range is achieved by decreasing the pressure. Due to lower absorption, the harmonic radiation can be observed at focus positions deeper inside the SIGC ($z_f < 0$). At certain focal lengths f in Fig. 3.5(b), a reduced phase-matching range Δz_f is observed. This can be attributed to unfavorable phase-matching conditions causing a minimum in the harmonic yield versus focus position. For example, in Fig. 3.5(a), the local minimum of the harmonic intensity around a focus position $z_f \approx -11$ mm results in a reduced phase-matching range for this focal length (cf. $f = 280$ mm in Fig. 3.5(b)).

In conclusion, a reduction of the focal length at a constant pulse energy decreases the harmonic conversion efficiency. The range of focus positions Δz_f , where harmonics are generated, is determined by the gas absorption rather than by the focal length of the lens.

Xenon as nonlinear medium Helium as a nonlinear medium enables the generation of harmonics with high photon energy, since the ionization potential is high (cf. Tab. 2.1). This, however, causes a relatively low ionization rate. As a consequence, HHG in helium exhibits a low photon flux. Choosing xenon as the nonlinear medium permits HHG with high photon flux due to a low ionization potential. However, the maximum achievable photon energy is lower using the same driver pulses as in helium. Maps of harmonic intensity versus focus position generated in xenon are shown in Fig. 3.6 for two different conditions. Due to the high absorption in xenon at the

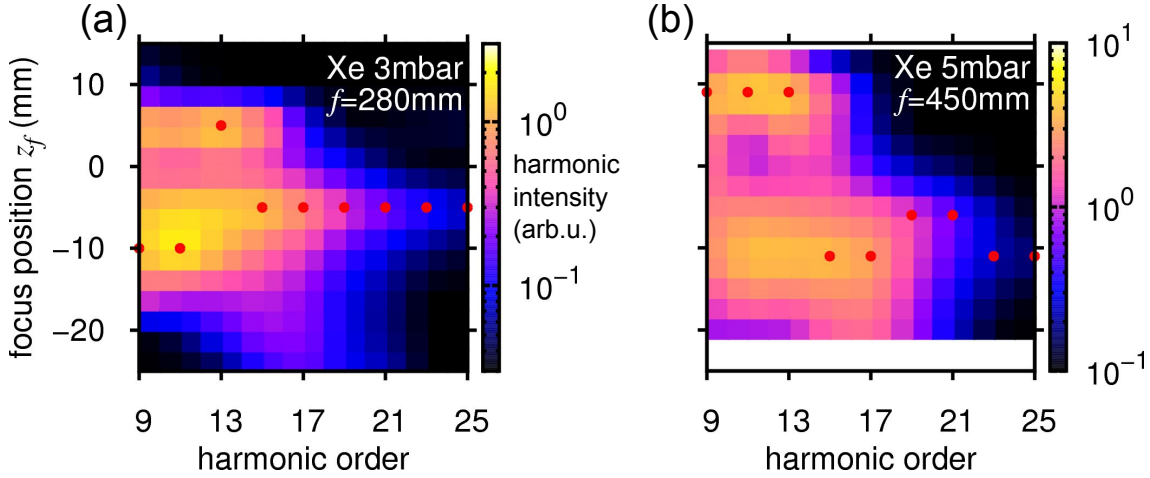


Figure 3.6: Harmonic intensity versus order and focus position in xenon (a) for a pressure of 3 mbar and a lens with focal length $f = 280$ mm, and (b) for a pressure of 5 mbar and a lens with focal length $f = 450$ mm. The red points (\bullet) indicate the focus position of maximum harmonic intensity. The color scale encodes the spectral power density of the individual harmonic orders in arbitrary units. Note that the harmonic intensity is interpolated with two points between the harmonic orders and the focus position, respectively, for better visualization.

relevant wavelength range, HHG is confined to approximately ± 10 mm around the exit of the SIGC even at the low pressure. As expected, a high intensity of the generated harmonics is obtained as can be seen from the range of the color scales in comparison to the maps recorded in helium (compare e.g. Figs. 3.2 and 3.6). The features observed for helium are also found in the case of xenon (Fig. 3.6), as discussed in the following. Placing the focus at the location of the pinhole ($z_f \approx 0$), a drop in the harmonic intensity is observed, which is attributed to bad phase-matching conditions and high ionization in the focus. The low order harmonics are generated for focus positions before and behind the pinhole as observed in helium for the 29th and 39th harmonic (cf. Fig. 3.3). A possible explanation could be that the formation of a gradient is suppressed at this low pressure, and thus, low harmonics generated within the SIGC are not absorbed beyond the exit of the SIGC. Higher orders are generated efficiently only inside the SIGC, as discussed above for the case of helium. The maximum harmonic order observed in xenon is the 25th harmonic, which is well below the expected order⁴ of about 219 according to the cutoff law (2.15). This can be explained by the high ionization rate of xenon leading to a depletion of the density of neutral atoms before the maximum intensity of the pulse is reached. In

⁴The estimate uses Eq. (2.15) with an intensity of $I = 1.7 \times 10^{15}$ W/cm² and a central wavelength of $\lambda_0 = 800$ nm. For the intensity estimate, a focal length of $f = 450$ mm, $M^2 = 1.5$, a waist of $w_0 = 5$ mm, and a pulse energy of 1.2 mJ at 35 fs pulse duration is assumed.

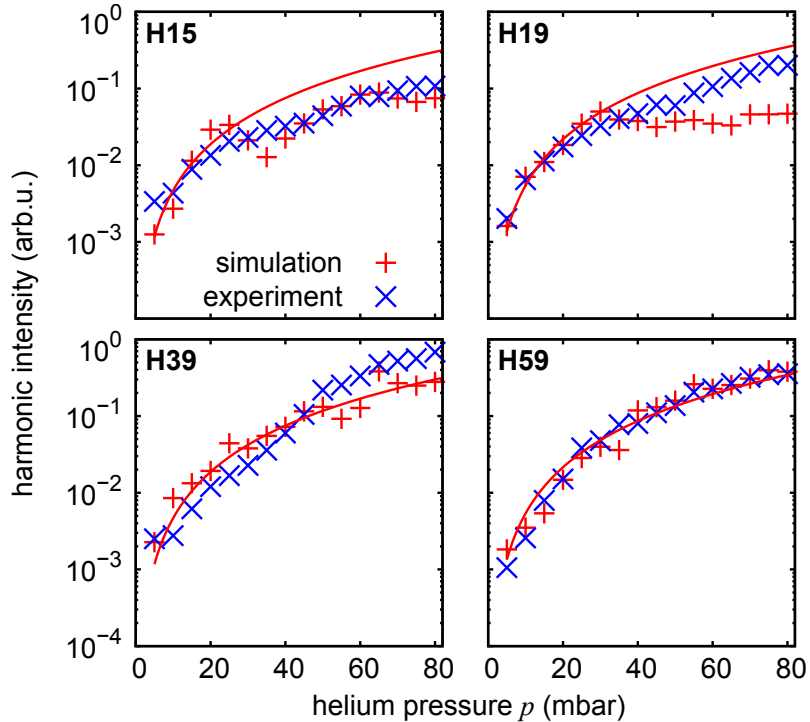


Figure 3.7: Pressure dependence of the harmonic intensity in helium. The measured (\times) and the simulated intensities ($+$) of selected harmonics (as labeled) are shown versus helium pressure at a fixed focus position $z_f \approx 0$ for a lens with focal length $f = 450$ mm. The red solid line represents a parabola fitted to the first points of the simulation.

addition, the fundamental beam is influenced by the density of free electrons, which leads to defocusing before the geometrical focus is passed (cf. Sec. 2.2.2).

In summary, xenon features a high photon flux at low photon energies, in contrast to helium. The phase-matching effects discussed for helium are also found for xenon: higher orders are only produced within the SIGC, while lower orders are generated for focus positions both inside and outside the SIGC.

3.1.3 Pressure dependence

Keeping the focus position fixed at $z_f \approx 0$, the pressure of helium is varied from 5 mbar to 80 mbar. The harmonic intensity increases monotonically with the gas pressure as shown in Fig. 3.7 for a lens with focal length of $f = 450$ mm. The 15th harmonic order starts to saturate above a pressure of about 30 mbar. For harmonics higher than the 17th order, no saturation is observed. This remains valid for

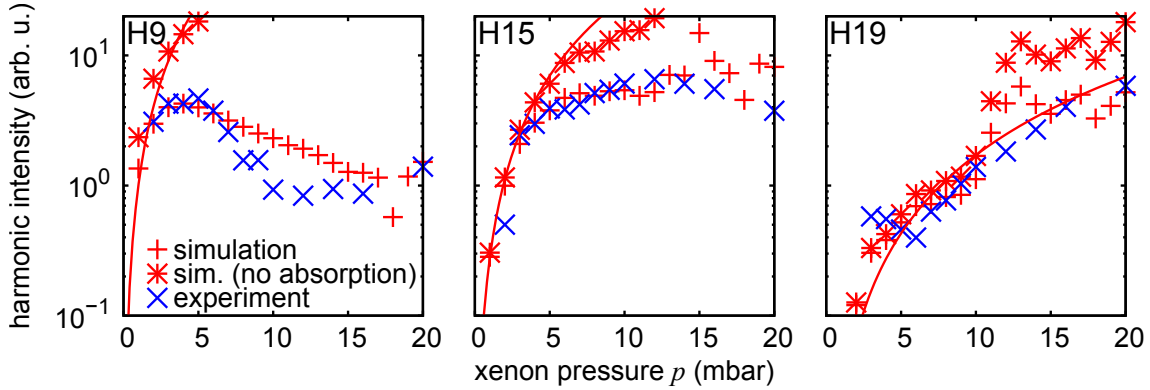


Figure 3.8: Pressure dependence of the harmonic intensity in xenon. The measured (\times) and the simulated intensities ($+$) of selected harmonics (as labeled) are shown versus xenon pressure at a fixed focus position $z_f \approx 0$. In addition, the numerical results without absorption are plotted ($*$). The solid red line represents a parabolic fit to the first points of the simulation without absorption.

a pressure measured up to 250 mbar.⁵ Numerical simulations (\times in Fig. 3.7), performed at the experimental conditions (same parameters as in Sec. 3.1.2), reproduce the measured data well. In agreement with absorption data [Hen93], the saturation effect is attributed to absorption, which is more relevant at the lower orders as can be seen from Fig. 3.4(a). Different to the experiment, a significant absorption is observed in the simulation at the 19th harmonic above a pressure of 30 mbar, while absorption in the experiment becomes important at the 17th harmonic order. This might be explained by the fact that static atomic scattering factors are used to calculate absorption. Intensity dependent effects are not accounted for, which might induce absorption at a shifted wavelength in the presence of the strong laser field [Gaa11]. An absorption-limited generation of harmonics can be tested by comparing the pressure dependence with a quadratic law as discussed in the following. Neglecting phase-matching and absorption effects, a nonlinear medium generates harmonic radiation with an intensity proportional to the square number of emitting atoms: $I_q \propto |\mathcal{E}_q|^2 \propto |\mathcal{P}_q|^2 \propto \mathcal{N}_{\text{neu}}^2$ (cf. Eqs. (2.39), (2.37), and (2.38)). Figure 3.7 shows a parabolic fit to the first points of the simulation. It demonstrates that the higher orders increase according to the assumption of negligible absorption, and the conversion efficiency can be further scaled up at these conditions by increasing the pressure.

In xenon, the saturation effects are more pronounced. Measured (\times) and simulated data ($+$) of the harmonic intensity versus pressure are presented in Fig. 3.8. In addition, results from simulations are shown, where absorption is disabled ($*$). Increasing the xenon pressure above 5 mbar, the 15th harmonic features a saturation

⁵For the measurement at the high pressure, a lens of 280 mm was applied for no particular reason.

of the measured intensity and simulated intensity accounting for absorption. The intensity of lower harmonic orders (H9 to H13) even decreases on raising the pressure. A saturation and a decrease of the conversion efficiency with increasing pressure has also been reported for a gas jet [Alt96]. The decrease of the conversion efficiency was attributed to be caused mainly by a defocusing of the fundamental field due to free electrons. Since ionization plays a major role, especially in xenon, the free electron distribution results in defocusing of the fundamental beam, which reduces the conversion efficiency of harmonics. In the simulations presented here, this defocusing effect of the fundamental field is not included which might cause the deviation between measured and simulated data for the 9th harmonic at high pressure. Nevertheless, the behavior of the 9th harmonic as well as the measured data for other harmonics is well reproduced by the simulations. Moreover, no saturation is observed for the simulations with disabled absorption, which follow the square-law as discussed above, illustrated by the solid lines (Fig. 3.8). Thus, the saturation effects and the decrease of the conversion efficiency is attributed mainly to the xenon gas absorption. Higher orders are still generated according to the square-law (see H19) with negligible influence from absorption when changing the pressure from 2 mbar to 20 mbar.

The simulation with absorption reproduces the experimental data in good agreement for higher harmonic orders. As stated above, a growing deviation at higher pressure could be attributed to neglected nonlinear effects in the simulated propagation of the fundamental field. Another important influence has the spectral splitting effect (see Sec. 3.1.5) which reduces the measured spectral power density mainly for the lower harmonic orders. Since the simulation computes the spectral power density at a discrete frequency, these effects are not incorporated and lead to an increasing discrepancy between experiment and simulation at lower orders.

In summary, the pressure dependence of HHG in helium and xenon in a SIGC has been presented. An absorption-limited generation of lower harmonic orders was observed in both gases, while higher orders could be generated without saturation in the applied pressure range. The simulations reproduce the experimental data, and confirm that absorption causes the saturation in the harmonic conversion efficiency.

3.1.4 Trajectory contributions and coherence properties

The phase matching of high-order harmonics does not only influence the conversion efficiency, but also has a major effect on the spatial profile of the emitted radiation. As shown in Fig. 2.11(a) in Sec. 2.4.3 for the gas jet geometry, the harmonic radiation features a spatial ring structure for a jet position before the focus due to off-axis phase matching [Sal95]. In this section, measurements of the spatial beam profile of

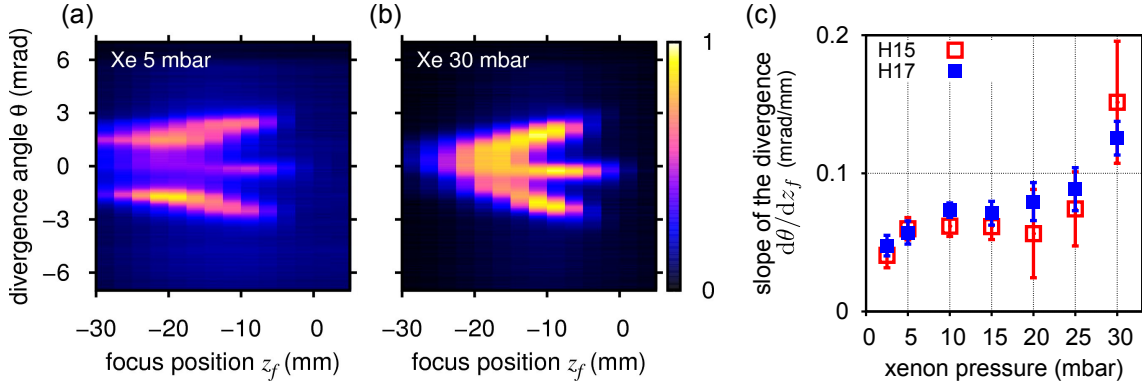


Figure 3.9: Spatial harmonic profiles versus focus position in xenon. (a)–(b) Spatial profiles of the 17th harmonic versus focus position z_f in xenon (a) at a pressure of 5 mbar, and (b) at a pressure of 30 mbar. A lens with $f = 500$ mm was applied. The color encodes the normalized linear intensity. (c) Slopes of the divergence of the outer ring structure versus focus position at different pressures. The slopes of the 15th (\square) and 17th (\blacksquare) harmonic order are illustrated. The error bars indicate the least square difference of the linear fit (see text for details).

high-order harmonics generated in a SIGC filled with xenon [Kre11] are presented. Therefore, the experimental setup is modified as described in Sec. 3.1.1.

Figure 3.9(a) and (b) show vertical slices of the beam profiles of the 17th harmonic versus the focus position at two different xenon pressures. Harmonic radiation is observed which is emitted on-axis with low divergence, and a ring structure emitted at high divergence symmetrically around the axis.⁶ At $z_f \lesssim -20$ mm inside the SIGC, the on-axis and the off-axis contribution appear to overlap and merge at higher pressure. Translating the focus in the direction of the exit pinhole, the ring structure exhibits an increasing divergence angle θ , which well separates the on-axis from the off-axis contributions. At higher pressures, the divergence angle θ versus focus position increases with a steeper slope $d\theta/dz_f$. This is illustrated in Fig. 3.9(c) which shows these slopes versus pressure for the 15th and 17th harmonic order. The slopes are determined by a linear fit to the center of gravity of the off-axis contributions.

The occurrence of the spatial structure of the emitted harmonic radiation is explained by phase matching of different electron trajectory contributions to HHG. As introduced in Sec. 2.3.3, the HHG contributions from different quantum paths j exhibit an intensity dependent phase with a slope α_j proportional to their traveling time τ_j [Gaa02]. This results in a larger divergence angle $\theta_{\text{long}} \propto \alpha_{\text{long}}$ of the long trajectory contribution, and accordingly, a small divergence angle $\theta_{\text{short}} \propto \alpha_{\text{short}}$

⁶The divergence angle θ is determined by assuming that the harmonics are generated in a point source close to the axis at the position of the pinhole.

for harmonic radiation from the short trajectory (cf. Sec. 2.4.3). The different divergences of both trajectory contributions were confirmed in a gas jet by spatially resolved measurements of the coherence time $T_{\text{coh},j} \propto 1/\alpha_j$ [Bel98, Lyn99]. The ratio $\nu = \alpha_{\text{long}}/\alpha_{\text{short}} = T_{\text{coh,short}}/T_{\text{coh,long}}$ between the coherence times in both regions corresponds to the relation between the phase slope factors of both contributing electron trajectories. For the 17th harmonic in argon in Ref. [Lyn99], the ratio yields $\nu \approx 3.2$.

In analogy to Refs. [Bel98] and [Lyn99], spatially resolved measurements of the coherence time are performed to confirm that the measured off-axis structure in Fig. 3.9 originates from the long trajectory, and the on-axis contribution stems from the short trajectory (cf. Appendix A.2). For the 17th harmonic in 20 mbar xenon, a coherence time $T_{\text{coh,short}} = (15.5 \pm 2.9)$ fs and $T_{\text{coh,long}} = (3.9 \pm 0.6)$ fs is measured in the on-axis and off-axis region, respectively, supporting the above interpretation. A factor $\nu = (4.0 \pm 1.4)$ between the phase slopes is determined for these conditions, which is in excellent agreement with the factor $\nu = \alpha_{\text{long}}/\alpha_{\text{short}} = \theta_{\text{long}}/\theta_{\text{short}} \approx 4.1$, determined via the divergence angles from the profile measurements (cf. Appendix A.2).

Figure 3.9 also shows that the divergence θ of the off-axis contribution increases, when moving the focus position from inside the SIGC towards the pinhole, corresponding to an increasing z_f . This effect can be explained by the following argument. The phase slope $\alpha_{\text{long}}(I)$ of the long trajectory increases with raising laser intensity I [Gaa02],⁷ and so does the divergence $\theta(I) \propto \alpha_{\text{long}}(I)$ of the corresponding harmonic radiation. Moving the focus position z_f from inside the SIGC towards the pinhole causes a higher intensity I in the interaction volume⁸ for HHG and consequently an increased divergence $\theta(I)$. Note that this could be exploited to track the intensity dependence of the phase slope $\alpha_{\text{long}}(I)$.

A similar argument explains the higher slope $d\theta/dz_f$ at a higher pressure, illustrated in Fig. 3.9(c). Considering a focus position $z_f < 0$ well inside the SIGC, the pressure determines the interaction volume via absorption and thus, influences the intensity contributing to HHG. At a high pressure, the interaction volume is confined close to the exit pinhole of the SIGC and might not contain the focus having the highest intensity. For a low pressure, the interaction volume is larger and higher intensities from positions deep inside the SIGC contribute to the harmonic yield. This, results in a larger divergence angle $\theta(I)$ for a low pressure compared to a high pressure at a focus position $z_f < 0$, and in turn, in a smaller slope $d\theta/dz_f$ at a lower pressure. At a focus position $z_f \approx 0$, the intensity contributing to HHG is equal for all pressures, and consequently, the divergence angle θ is equal in agreement with the observations shown in Fig. 3.9.

⁷Remind that the slopes α are only constant in a first order approximation, and merge in the cutoff region at a single value (cf. Sec. 2.3.3).

⁸Compare to Sec. 3.1.2 and L_{amp} in Sec. 2.4.2.

To summarize, spatially separated contributions to the harmonic radiation have been identified, which originate from different electron trajectories in HHG. The contributions from the short trajectory are emitted on-axis, while the radiation of the long trajectory emerges in an off-axis ring structure. The intensity dependence of the phase slope $\alpha(I)$ gives rise to an increase of the divergence angle θ when moving the focus position from deep inside the SIGC towards the pinhole. In turn, this might be exploited in future experiments to track the intensity dependence of the phase slope. With regard to IAP generation, the different divergence angle is beneficial to spatially filter different quantum path contributions for optimal compensation of the harmonic chirp [Mai03].

3.1.5 Spectral splitting, broadening, and blue shift

The application of ultra-short laser pulses at high intensity leads to non-adiabatic effects and transient phase matching as discussed in Secs. 2.3.3 and 2.4.3. Thereby, non-adiabatic spectral splitting occurs for driving laser pulses below ~ 100 fs due to the rapidly varying envelope which induces a temporally changing atomic phase ϕ_{at} in the single-atom response. Adiabatic spectral splitting is caused by the rapidly changing density of free electrons. This induces transient phase matching due to the varying phase contribution $\Delta\phi_{\text{el}}$ from the free electrons. In literature, spectral splitting and blue shift is assigned to either the non-adiabatic [Bru08, Kan95, Pap01, Shi99] or the adiabatic case [Alt99, Fan02, Wan00, Zho00]. In the following, both the adiabatic effects and the non-adiabatic effects are demonstrated in HHG with the SIGC setup.

Spectral splitting and blue shifting of harmonics are observed in the experiments with xenon using the XUV monochromator setup (LHT 30, Horiba-Jobin-Yvon, cf. Sec. 3.1.1). Figure 3.10 shows normalized spectra which are generated in 5 mbar xenon at different focus positions. Harmonics, which are generated at a focus position

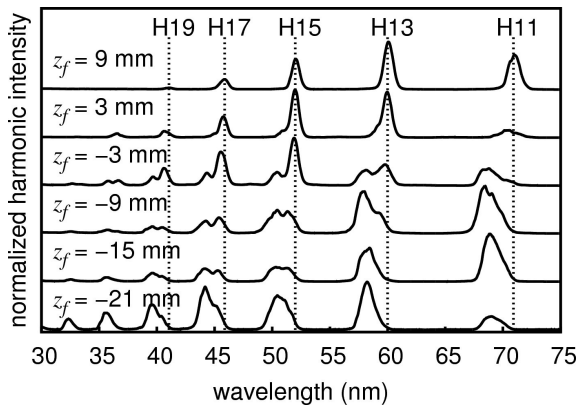


Figure 3.10: Spectral evolution versus focus position of harmonics generated in xenon. Harmonic spectra are generated in 5 mbar xenon using a lens with a focal length $f = 450$ mm at different focus positions z_f as labeled. Moving the focus into the SIGC results in a spectral blue shift, broadening, and line splitting.

Figure 3.11: Spectral splitting and blue shift versus pulse energy. Plotted is the energy dependence of the 15th harmonic in 5 mbar xenon obtained using a lens with $f = 280$ mm and the focus at $z_f = -5$ mm.

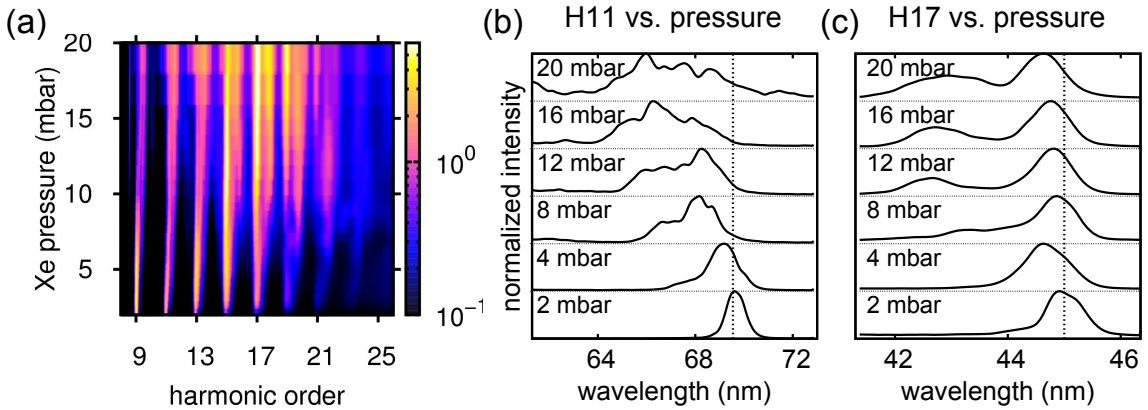
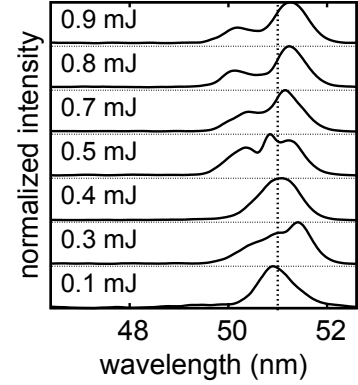


Figure 3.12: Spectral splitting and blue shift versus pressure in xenon. (a) Spectral intensity map of the pressure dependence using a lens with $f = 450$ mm at $z_f \approx 0$. The color encodes the harmonic intensity in arbitrary units. The single spectra at different pressures are shown in (b) for the 11th harmonic, and in (c) for the 17th harmonic.

outside the SIGC ($z_f > 0$), hardly exhibit any splitting effects nor a blue shift. Moving the focus inside the SIGC, spectral splitting immediately becomes visible and the harmonics feature a blue shift. In addition, the spectral width of the harmonics increases. In Fig. 3.11, the dependence of the spectral effects on the driving pulse energy is demonstrated. With increasing pulse energy, the splitting of the harmonics gets more pronounced. Moreover, the spectral center is shifted further into the blue spectral region. Raising the xenon pressure has a similar consequence as shown in the spectral map, Fig. 3.12(a). Figures 3.12(b) and 3.12(c) illustrate harmonic spectra of the 11th and 17th harmonic, respectively, at a varying pressure. The harmonic spectrum becomes modulated and is shifted to lower wavelengths in case of a higher pressure. While the transient phase matching depends directly on the atomic density, the non-adiabatic splitting stems from the single-atom response and is not directly influenced by pressure. Due to the fact, that a dependence on the pressure is obtained, the observed features are attributed to transient phase matching, i.e. to an adiabatic effect. The features observed in the measurements (cf. Fig. 3.12(b))

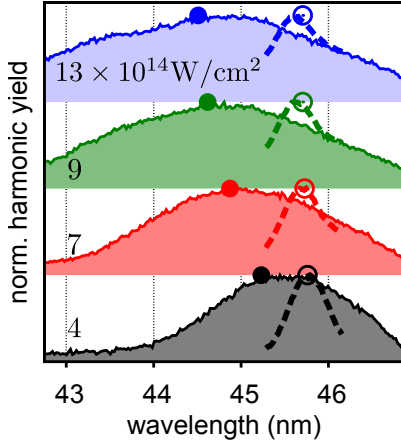


Figure 3.13: Non-adiabatic spectral splitting at varying laser intensity. The laser intensity is labeled in units of 10^{14} W/cm^2 . The filled curves are evaluated in the off-axis region (see text for details), the dashed lines illustrate the on-axis contributions. The points show the corresponding center-of-gravity wavelength.

are supported by simulations of transient phase matching at different conditions (cf. Fig. 2.14(b)) [Zho00].

Experiments in helium exhibit marginal spectral splitting even at high pressure. Since helium has a high ionization potential, the ionization rate is low and the density of free electrons does not change significantly during the pulse. Thus, these observed features are expected to be less pronounced than in xenon which has a low ionization potential.

Non-adiabatic spectral splitting and blue shift are determined by the intensity dependent atomic phase ϕ_{at} . While these effects are hardly observable for the short trajectory, the long trajectory with a strong intensity dependence is strongly influenced. Using the XUV monochromator (LHT 30, Horiba-Jobin-Yvon), only minor contributions from the long trajectory are recorded. Assuming a divergence of the harmonic radiation from the long trajectory of 3 mrad (cf. Sec. 3.9), the harmonic ring structure has a diameter of 6 mm in a distance of 1 m from the SIGC pinhole, where the entrance slit of the spectrometer is located. Since the slit has a height of about 6 mm, the long trajectory is transmitted only partially. Using the home-built Seya-Namioka spectrometer, which was used for the beam profile measurements in Sec. 3.1.4, it is possible to measure the non-adiabatic effects in the spectrum of the long trajectory contributions [Kre11]. To demonstrate the non-adiabatic effects, spatially resolved measurements of the harmonic spectrum are performed via measurements of the beam profile behind the grating of the spectrometer. The wavelength axis is calibrated by the horizontal center positions of the 17th and 19th harmonic, which are both recorded simultaneously. By integration over the vertical axis in a narrow region, the harmonic yield of the on-axis and off-axis contribution is estimated, respectively. Figure 3.13 shows the resulting spectrum in the on-axis region (dashed lines) and off-axis regions (filled solid curves) at different laser intensities. Despite of the poor spectral resolution due to missing entrance and exit slits of the spectrometer, it is visible from the center-of-gravity wavelength that the on-axis

and off-axis contributions to the same harmonic order diverge with increasing laser intensity. Since the on-axis contribution originates from the short trajectory (cf. Sec. 3.1.4) with a small phase slope α_{short} , its center wavelength changes marginally with a varying intensity. In contrast, the off-axis contribution from the long trajectory has a large phase slope α_{long} and is blue shifted at higher laser intensities. This results in the non-adiabatic spectral splitting of the complete spectrum of the harmonic.

In summary, both adiabatic and non-adiabatic spectral splitting of high-order harmonics generated in a SIGC filled with xenon have been presented. The adiabatic spectral splitting and blue shift was studied versus focus position, pulse energy, and xenon pressure. The non-adiabatic spectral splitting was identified directly from HHG contributions of the short and long trajectory. Both contributions are shifted in the wavelength with respect to each other, which was shown for different laser intensities. It was demonstrated that both adiabatic and non-adiabatic effects are apparent for HHG in the SIGC and can be identified by a pressure variation or spatial measurements. In future experiments, both effects could be detected simultaneously by spatially resolved measurements of the spectrum with higher spectral resolution.

3.2 Harmonic generation from ultra-short pulses

Attosecond pulse generation relies on HHG by few- or single-cycle pulses. Filamentation, as a promising technique for the production of few-cycle driver pulses with a simple setup (cf. Sec. 2.2), was first applied to HHG in 1998 by Lange *et al.* [Lan98]. They reported the 15th harmonic in 50 mbar xenon using a 3 mJ driver pulse after filamentation in air. Zaïr *et al.* [Zai07] generated harmonics up to the 33rd order, which feature spectral broadening and a blue shift due to the short duration of the driving pulses of 10 fs after a single filamentation stage and below 5 fs after a second filamentation stage. At the time of the present work [Ste09a], the generation of an XUV continuum up to 113 eV in neon was reported from pulses after filamentation [Lee09].

In this section, the generation of high-order harmonics was demonstrated using pulses, which are compressed in a filament with subsequent dispersion compensation by double chirped mirrors (DCMs) [Ste09a]. These few-cycle pulses from the filament are applied to HHG in different noble gases, featuring spectral broadening and a continuous XUV spectrum up to 124 eV. The influence of the noble gas and the influence of the chirp of the driver pulse on the harmonic spectra is investigated.

3.2.1 Generation of ultra-short pulses using filamentation

The setup for the generation of ultra-short pulses by filamentation is shown in Fig. 3.14. The 30-fs-pulses from the CPA-laser-system are focused into the filamentation cell by a curved mirror CM1 with 2 m focal length. The 2-m-long cell filled with 450 mbar argon is terminated by a 1-mm-thick CaF₂ window on each side placed in Brewster's angle. A single filament is formed which can be optimized using the aperture A1 behind the amplifier exit. For an aperture diameter of 7 mm used in the experiment, the transmitted pulses have an energy of 0.85 mJ. The shortest pulse durations after filamentation are only found in the white-light core [Cou08]. Thus, care has to be taken to screen the outer parts of the beam, which contain radiation from the reservoir and from conical emission [Nib96]. Therefore, a second aperture A2 with diameter of 3 mm is placed behind the filamentation stage. The dispersion management is realized by a pair of DCMs [Kär01] which cause an average group-delay dispersion (GDD) of about -70 fs^2 per reflection. After eight reflections, a GDD of -560 fs^2 is accumulated which compensates the dispersion of the air and of the subsequent HHG setup, in order to achieve a flat phase at the place of HHG. High-order harmonics are generated in the same SIGC setup as characterized in Sec. 3.1.1 and shown in Fig. 3.1. A focusing lens L1 with focal length of $f = 500 \text{ mm}$ is applied which yields a real focal length of about 660 mm due to the

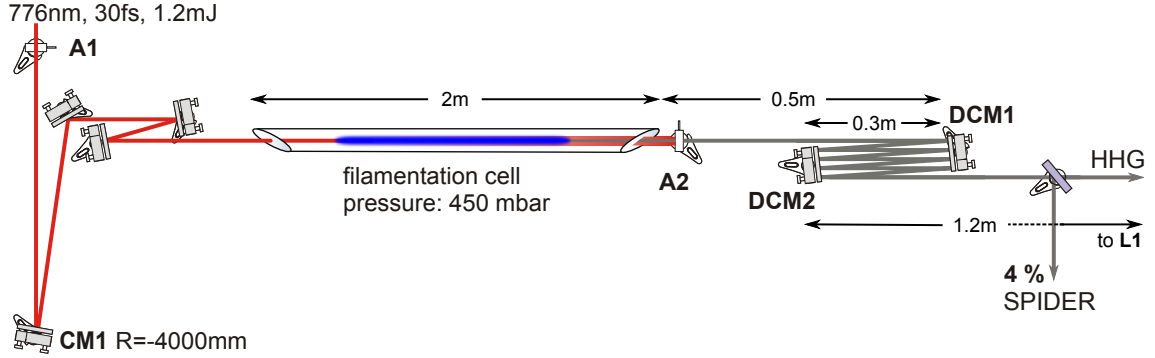


Figure 3.14: Experimental filamentation setup for generation of ultra-short pulses. The spectrum of laser pulses from the amplifier system is broadened in the filamentation stage and characterized in a SPIDER setup. The double-chirped mirrors (DCM) compensate the dispersion. The compressed pulses are applied to HHG in a subsequent setup described in Sec. 3.1.1, see Fig. 3.1. (See text for details.)

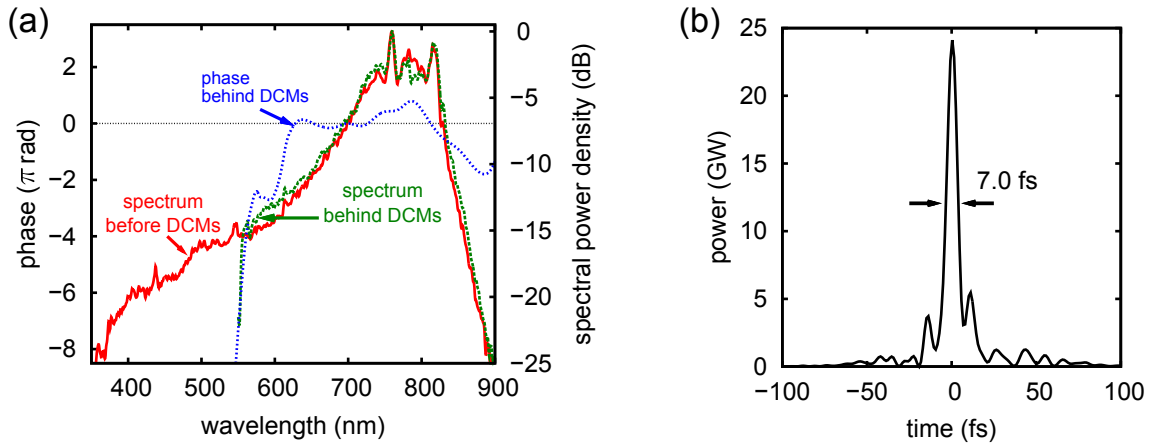


Figure 3.15: Pulse characterization after the filamentation stage. (a) Spectrum and phase of the pulses after dispersion compensation with eight reflections on DCMs. For comparison, the spectrum before the DCMs is shown. (b) The reconstructed pulse with pulse energy of 0.3 mJ and duration of 7.0 fs.

beam divergence after the filament. The focus is placed approximately 1 cm before the pinhole within the SIGC, to generate harmonics of high order (cf. Sec. 3.1.2).

After filamentation, the pulses are characterized by spectral phase interferometry for direct electric field reconstruction (SPIDER) [Iac98]. The white-light core after filamentation supports a Fourier-limited pulse duration of 5.2 fs (FWHM). Figure 3.15(a) shows the corresponding spectrum, as well as the spectrum and the measured phase behind the dispersion compensation. Since the DCMs are designed for a wavelength range from 600 to 1200 nm, the phase diverges and the spectrum suffers losses below 600 nm. After the dispersion compensation, a pulse energy of

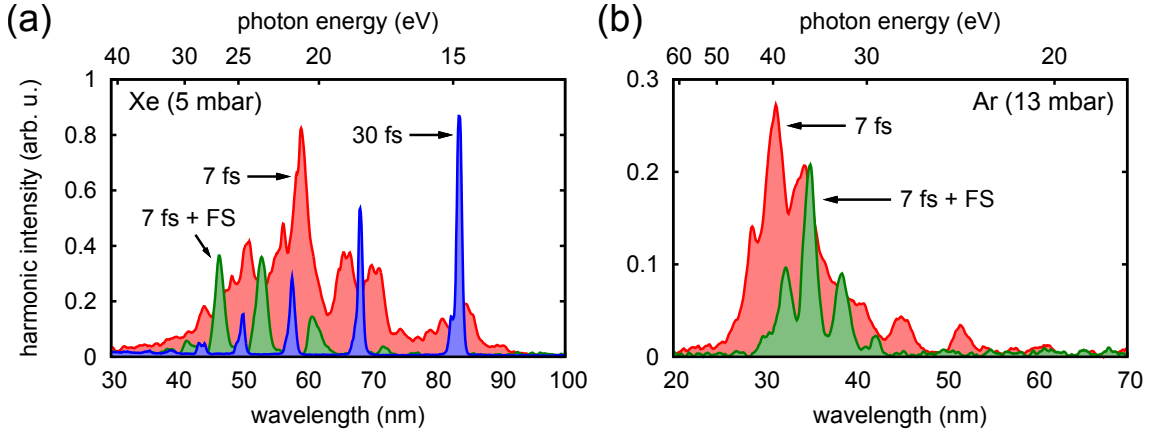


Figure 3.16: Harmonic spectra from few-cycle pulses in xenon and argon. (a) Harmonic spectra in 5 mbar xenon using 7-fs-pulses after filamentation. For comparison, harmonics from pulses of 30 fs duration and comparable peak intensity are shown. In addition, harmonic spectra are presented, generated from 7-fs-pulses which are stretched by 6.35 mm fused silica (FS). (b) Harmonic spectrum in 13 mbar argon using 7-fs-pulses after filamentation and the spectrum from stretched 7-fs-pulses.

0.3 mJ remains and a pulse of 7 fs FWHM duration is reconstructed. A detailed analysis of the filament is published in Ref. [Sch09b].

3.2.2 Spectral broadening of high-order harmonics

The 7-fs-pulses generated in the filament are applied to HHG in a SIGC filled with different noble gases. Figure 3.16(a) shows the spectra which are generated in 5 mbar xenon by pulses of different durations. Note that all spectra are averaged over different CEO phases, since the used amplifier system is not CEO-phase stabilized. The compressed few-cycle pulses after the filament as well as 30-fs-pulses directly from the amplifier are applied and attenuated to have a comparable peak intensity. While the 30-fs-pulses produce a well resolved harmonic peak structure with harmonics of narrow bandwidth, a broad and modulated spectral structure is generated by the 7-fs-pulses. Both spectra extend to a similar cutoff energy, which is mainly determined by the strong ionization in xenon and the resulting depletion of the ground state (cf. Sec. 3.1.2). The third spectrum in Fig. 3.16(a) is generated by pulses from the filament that are stretched by propagation through an additional fused silica substrate with length of 6.35 mm. Thus, the pulses of initially 7 fs duration are stretched to about 80 fs with a peak power reduced by a factor of nine. The measured cutoff energy corresponds well to the single-atom prediction. It can be observed that the modulated broad harmonic structure from the 7-fs-pulses becomes resolved to individual harmonic orders for the stretched pulses. The harmonics are red shifted to

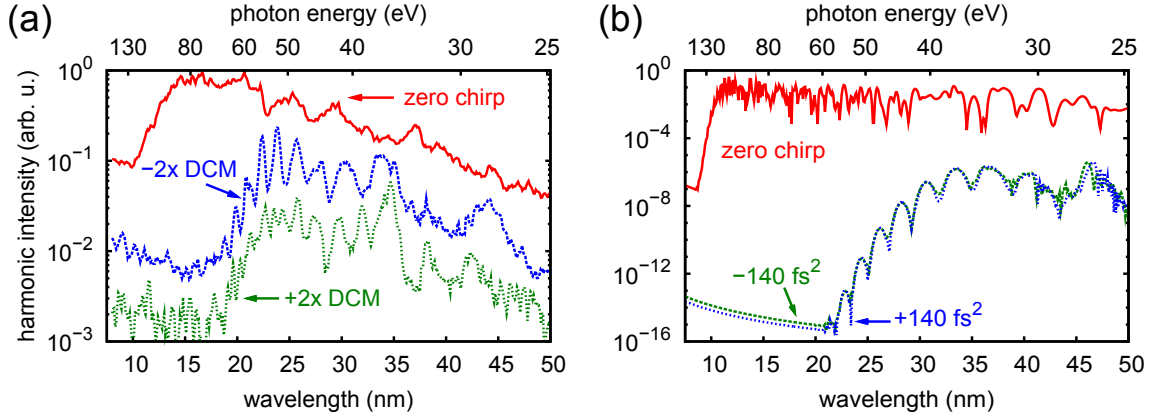


Figure 3.17: HHG in 40 mbar neon using few-cycle pulses. (a) Experimental results using 7-fs-pulses with zero chirp (red solid line), a positive chirp (blue dashed line), or a negative chirp (green small dashed line). Different chirps are realized by less or additional reflections on the DCMs. (b) Results from the simulation of the single-atom response mimicking experimental conditions. In addition to the harmonic spectrum from a Fourier-limited 7-fs-pulse, two spectra are shown with applied dispersion of $\pm 140 \text{ fs}^2$, which is caused by two reflections on the DCMs in the experiment.

higher wavelengths and broadened compared to the harmonics from the 30-fs-pulse. This can be attributed to the positive dispersion of the driver pulse. Since the pulse carries still enough energy to completely ionize xenon during the pulse, harmonics are generated predominantly on the raising slope of the envelope. Thus, the precursory part of the pulse produces harmonics with the momentary central frequency in the infrared (IR) spectral region. Due to the variation of the central frequency, harmonics are broadened.

Changing the nonlinear medium to argon of 13 mbar pressure, the obtained harmonic spectrum from 7-fs-pulses is shown in Fig. 3.16(b). For comparison, the pulses are stretched by fused silica, as above. A large spectral broadening is observed when the few-cycle pulses are applied, while the spectrum exhibits deeper modulation and a reduced cutoff for the chirped pulses due to the lower peak intensity of the chirped pulses.

The spectrum with the highest cutoff energy is obtained in neon. Neon features a high ionization potential (cf. Tab. 2.1) and thus allows for reaching high cutoff energies. Figure 3.17(a) shows the harmonic spectrum generated in 40 mbar of neon. A broad continuous spectrum with little modulations in the cutoff region which extends down to 10 nm (124 eV) is obtained from the few-cycle pulses. Changing the re-compression of the pulses demonstrates the effect of the pulse duration on the harmonic generation process. By removing two reflections on the DCMs, positive dispersion of 140 fs^2 is applied, while adding two reflections results in negatively chirped

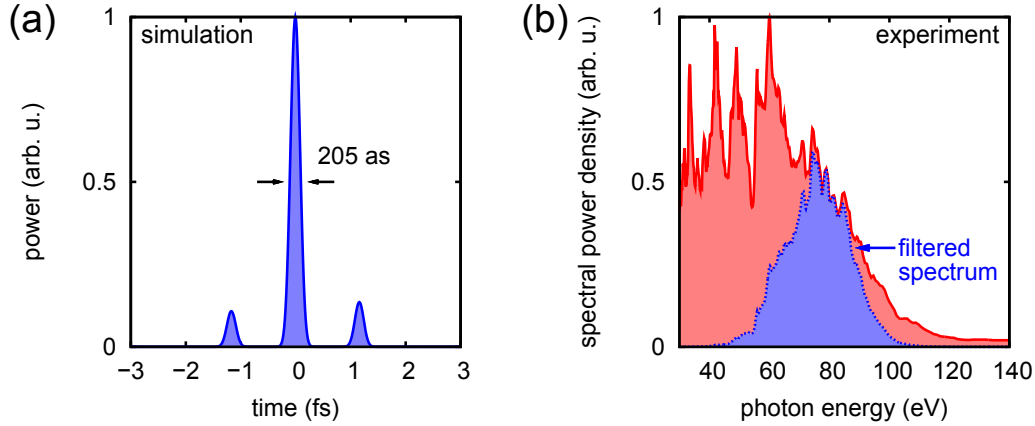


Figure 3.18: Attosecond pulses. (a) IAP reconstructed from the simulation (see Fig. 3.17(b)). The simulated spectrum is convolved with a Gaussian spectral filter around 124 eV with bandwidth of 14 eV. The reconstructed pulse using the filtered spectrum and the simulated phases yields an IAP of 205 as duration. (b) Experimental spectrum (cf. Fig. 3.17(a)) with and without Gaussian filter. The filter is centered around 80 eV with bandwidth of 28 eV.

pulses with GDD of -140 fs^2 . The pulses are stretched to a duration of about 50 fs. Generating harmonics with positively or negatively chirped pulses, a reduction of the cutoff energy is observed. Moreover, the spectrum becomes modulated and resolved harmonics are recognized. The total harmonic yield decreases using chirped pulses, which can be reversed for negatively chirped pulses by introducing positive dispersion with additional material. The different harmonic yield between application of positive and negative chirp might be a result from the asymmetry in the spectral shape of the driving laser pulse and from higher losses for the additional reflections on the DCMs. Simulations on the single-atom response are performed according to the Lewenstein model (cf. Sec. 2.3.2). A pulse with Gaussian temporal envelope function of 7 fs FWHM duration is assumed with a center wavelength of 700 nm. The peak intensity of the Fourier-limited pulse is set to $6 \times 10^{14} \text{ W/cm}^2$ close to the experimental conditions. The simulated harmonic spectra from a Fourier-limited pulse and from pulses, which are stretched by $\pm 140 \text{ fs}^2$, are shown in Fig. 3.17(b). An excellent agreement between the features of the experiment and the single-atom response is observed. The Fourier-limited pulses generate a harmonic spectrum which extends down to 10 nm, while chirped pulses reduce the cutoff energy and exhibit well resolved harmonics. The overall shape of the spectrum differs from the experimental structure for three main reasons: first, due to the assumption of a Gaussian pulse, second, due to propagation effects such as absorption, and third, due to the spectral response of the spectrometer. Particularly in the case of chirped pulses, the assumption of a Gaussian pulse in the simulations results in a disagreement with the experimental results. As a consequence from the spectral symmetry for a Gaus-

sian pulse, marginal changes in the calculated harmonic spectral shape and yield obtained when applying positive or negative dispersion. In contrast, the experimental spectrum of the driver pulses after filamentation is strongly asymmetric and the corresponding harmonic spectra for different chirps deviate in their intensities as discussed above.

Using the simulated spectrum with a convolution of a Gaussian spectral filter, one can estimate the attosecond pulse which could be produced. The Gaussian filter mimics a multi-layer mirror with a bandwidth of 14 eV centered around 124 eV. An isolated pulse with a duration of 205 as is reconstructed from the filtered XUV spectrum of the simulation, as shown in Fig. 3.18(a). Assuming flat phases and a filter bandwidth of 28 eV [Gou08] an isolated pulse of 76 as duration could be obtained using the measured spectrum in Fig. 3.18(b). Note, however, that the experimental spectrum is less modulated than the simulated one, which may stem from the resolution of the spectrometer as well as from the fact that the CEO phase of the driving laser is not stabilized. Thus, the above estimate has to be taken with care. Nevertheless, the filamentation setup is expected to deliver IR pulses with even shorter pulse duration when applying advanced multilayer optics designs [Per07] covering the full spectral bandwidth after the filament. This allows for the robust generation of short attosecond pulses with improved cutoff.

In summary, spectral broadening and blue shift of high-order harmonics generated by few-cycle driver pulses in different noble gases have been demonstrated. For comparison, harmonic spectra produced by pulses of different durations were presented. The XUV spectrum with the highest cutoff energy of 124 eV and a continuous shape was obtained in neon. This cutoff energy is well comparable to the cutoff energy around 120 eV reached by setups using hollow-core fibers [Gou08, Sch07], where IAP generation has been demonstrated. Simulations of the single-atom response were performed for the experimental conditions. The measured characteristics in the harmonic spectrum under application of differently chirped pulses are in agreement with the simulation. Using XUV multi-layer mirrors, an IAP with duration below 250 as might be generated using the filamentation setup provided that the CEO phase of the laser system is stabilized.

3.3 Conclusion

In this Chapter, the generation of high-order harmonics in a SIGC geometry has been studied. A systematic investigation of the phase-matching conditions has been performed by variation of the focus position and the pressure using different lenses and two different noble gases, helium and xenon. Phase-matching simulations re-

produce the experimental results in good agreement allowing for the interpretation of experimental features, such as the generation of higher harmonic orders only inside the SIGC and the absorption-limited generation of lower harmonic orders. The spatial profile of the harmonic radiation was analyzed, and contributions from different electron trajectories to HHG were identified. Thereby, coherence properties of the generated harmonic radiation are exploited. Adiabatic as well as non-adiabatic spectral splitting is observed in the experiment using two setups. The adiabatic effect was investigated in dependence on focus position, pressure, and energy. In the second part of this Chapter, a filament is applied to generate high-order harmonics by few-cycle driver pulses. Spectral broadening of harmonics in different noble gases was observed. The spectrum with the highest cutoff was obtained in neon featuring a continuous XUV structure. Simulations on the single-atom response reproduce well the experimental characteristics and the behavior of the spectrum applying chirped pulses. The simulation results and the experimental spectra are a promising basis for the generation of IAPs.

Chapter 4

Direct generation of high-order harmonics within a filament

In this Chapter, the generation of high-order harmonics by intensity spikes directly in a filament is discussed [Ste11]. While in previous studies the production of ultra-short laser pulses and the harmonic generation setup for attosecond pulse generation is always performed separately [Ago04, Gou08, Hen01, Kra09], the method presented here establishes a combined setup which constitutes a strongly simplified technique. The first generation of high-order harmonics directly in a filament was reported by Couairon *et al.* [Cou06] in 2006. Well resolved harmonics up to the 23rd order were demonstrated, generated by 0.8-mJ-pulses which were focused into a 14-cm long gas cell filled with 1 bar of argon. HHG within a filament is possible due to the occurrence of intensity spikes, predicted by recent theoretical work [Gaa09]. These spikes feature near single-cycle sub-pulses at an intensity well above the clamping intensity which is established in the standard filamentation models (cf. Sec. 2.2).

After a brief introduction into the theory of intensity spikes, the experimental results are presented, which feature a broad intense continuum in the XUV spectral region. An excellent agreement with numerical simulations is demonstrated. These simulations predict isolated attosecond pulse (IAP) production directly from the filament. Finally, it is shown that the intensity spikes can be controlled via accessible experimental parameters.

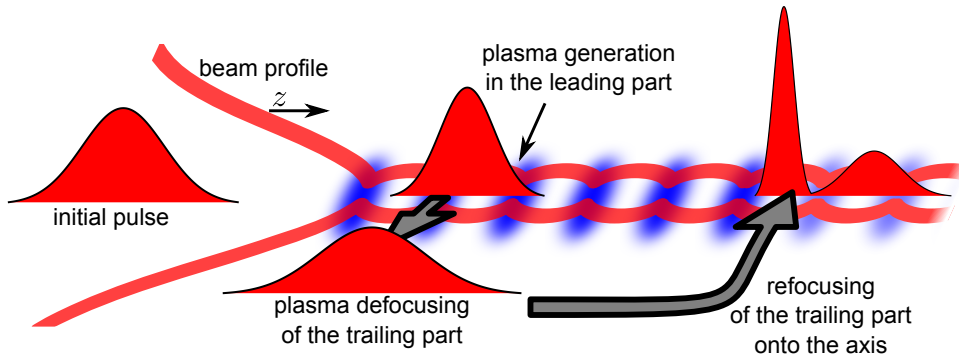


Figure 4.1: Sketch for the model of intensity spikes inside a filament. As in the self-guiding model a filament is initiated by Kerr focusing and balanced by plasma generation. The plasma generated in the leading part defocuses the trailing part of the pulse. During the propagation, the leading part suffers absorption and losses from plasma generation. In a rapid dynamical process the trailing part is refocused onto the axis leading to a highly intense sub-pulse.

4.1 The occurrence of intensity spikes in filamentation

The theoretical description of femtosecond filamentation is based on a local equilibrium between focusing and defocusing effects as discussed in Sec. 2.2. Thereby, filamentation models consider the two balancing effects of Kerr self-focusing and defocusing due to the generation of plasma and its free electron distribution. As a consequence, the maximally reached intensity during filamentation is clamped to the ionization threshold of the nonlinear medium. Recent theoretical work [Gaa09], has predicted the occurrence of intensity spikes, which far exceed the clamping intensity. The explanation of their emergence is sketched in Fig. 4.1. Intensity spikes are formed during filamentation in a dynamical spatio-temporal reshaping process. First, the trailing part of the pulse is defocused off the axis due to plasma generation in the leading part. Then, it is rapidly refocused onto the axis. This spatial refocusing process happens too quickly for the ionization to maintain the equilibrium by defocusing, and thus, the on-axis intensity is enhanced on a short time duration within a confined near single-cycle sub-pulse.

In contrast to the clamping intensity, the intensity of the spikes well exceeds the ionization threshold and is high enough for the generation of high-order harmonics. Due to the near single-cycle duration of the sub-pulse, the generated XUV radiation exhibits a continuum structure, which can be exploited for the production of IAPs. This technique offers a major simplification for the IAP generation, since spectral broadening, pulse compression, and HHG is performed within a single stage.

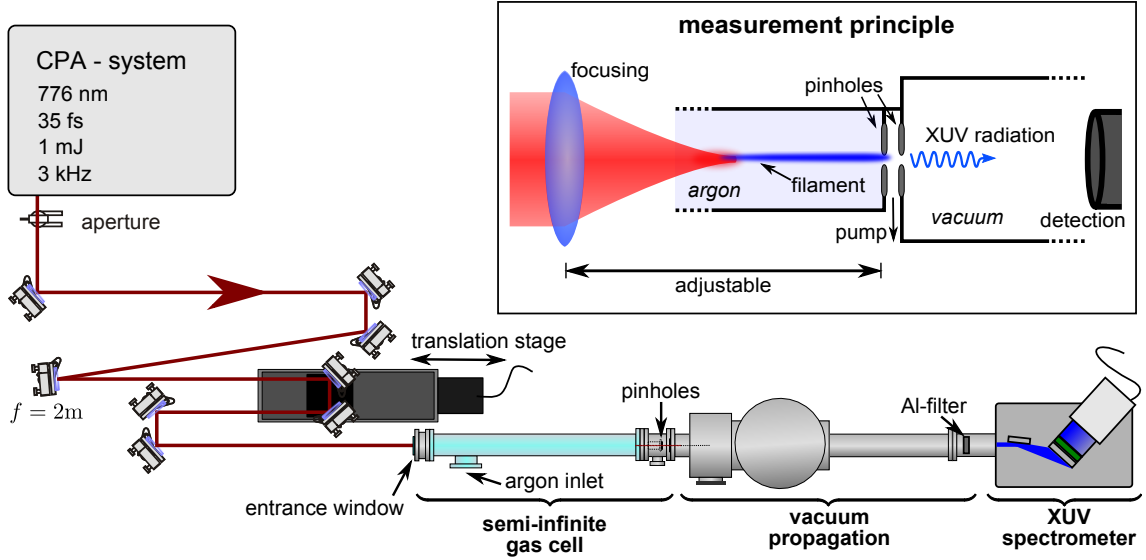


Figure 4.2: Experimental setup for HHG directly in a filament. The amplifier pulses are focused into a long SIGC, which is terminated by two pinholes as sketched in the inset. The distance between focusing mirror and pinholes can be adjusted by a translation stage. After propagation in vacuum and behind an aluminum filter, the generated harmonic radiation is recorded by a spectrometer.

4.2 Experimental observation of intensity spikes

The predicted intensity spikes, which occur on a spatially and temporally confined sub-pulse, are intense enough for the generation of high-order harmonics. Thus, this new filamentation model can be tested experimentally by extraction of XUV radiation directly from the filament. Thereby, the harmonic radiation acts as a highly nonlinear probe of the intensity within the filament. The spectral structure of the generated harmonics indicates the temporal dynamics on which the spikes occur. For near single-cycle sub-pulses a continuous spectral structure is expected, whereas a multi-cycle pulse produces resolved individual harmonics within the spectrum.

4.2.1 Experimental realization

The experimental setup is shown in Fig. 4.2, with a sketch of the measurement principle in the inset. Pulses of 35 fs duration are focused by a curved mirror with 2 m focal length into a 1 m long SIGC which is filled with argon at atmospheric pressure. An aperture with diameter of 7.5 mm is placed before the focusing mirror for stabilization and control of the filament. The transmitted pulse energy of 0.8 mJ yields a peak power of about 21 GW, which is 4 times larger than the critical power for self-

focusing in 1000 mbar argon¹ and enables filamentation in the SIGC. The entrance window of the SIGC consists of 2 mm CaF₂ and is passed in normal incidence in order to minimize misalignment and spatial dispersion due to refraction at different pressure conditions. The usual design of the SIGC (cf. Sec. 3.1.1) is extended by a second pinhole with diameter of 250 μm , which is placed at a distance of 1 cm behind the first one (500 – 800 μm diameter). The two pinholes serve as a double differential pumping stage and realize a steep pressure gradient from atmospheric pressure in the SIGC down below 5×10^{-4} mbar in the vacuum chamber. Between the pinholes, the background pressure is smaller than 10^{-1} mbar. The focused pulses create a filament in the SIGC which is truncated by the pinholes due to stopping of all non-linear effects at the transition to vacuum. Using a delay line between the focusing mirror and the SIGC, the filament can be displaced and cut at different positions. The generated harmonic radiation passes through the pinholes into vacuum and is recorded by an XUV spectrometer after 1 m linear propagation through vacuum and an aluminum foil of 200 nm thickness to block the fundamental light. In addition to the XUV monochromator (LHT 30, Horiba-Jobin-Yvon), a spectrometer with MCP and phosphor-screen (248/310-G, McPherson) is applied. The latter spectrometer is used for the measurement of single-shot spectra. For this purpose, the voltage of the MCP is gated between two levels using a pulse generator (PVX-4140, Directed Energy, Inc.) and two high-voltage sources (PS350/5000V-25W, Stanford Research Systems, Inc.) (see Appendix A.3).

Absolute photon numbers are measured via an XUV diode (AXUV100, International Radiation Detectors, Inc.) with a flat response of 0.25 A/W in the spectral range from 30 to 50 nm. The fundamental light is blocked by three aluminum foils, each with thickness of 300 nm and a measured transmission of 14% for the total harmonic radiation. The XUV diode is placed in 1.5 m distance from the pinholes and measures the full harmonic beam. The beam profiles of the full harmonic radiation are acquired by an MCP with phosphor-screen behind a 200 nm thick aluminum foil at the same distance of 1.5 m from the exit pinholes. The screen is recorded by a charge-coupled device (CCD) camera (C4742-95-12NRG, Hamamatsu Photonics K.K) and the images are saved on a computer.

¹A nonlinear refractive index of 1.74×10^{-19} cm²/W is assumed for this estimate (cf. Eq. (2.3) in Sec. 2.1.1) [Cou08].

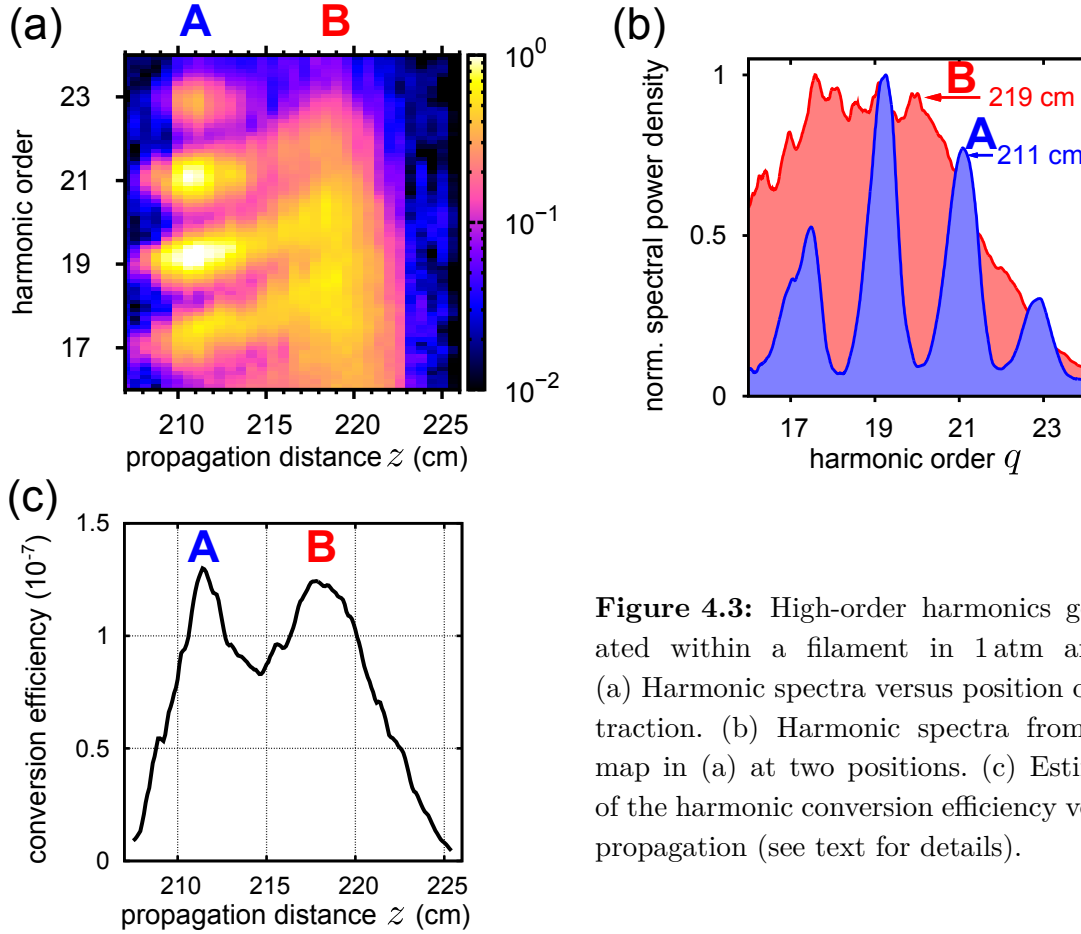


Figure 4.3: High-order harmonics generated within a filament in 1 atm argon. (a) Harmonic spectra versus position of extraction. (b) Harmonic spectra from the map in (a) at two positions. (c) Estimate of the harmonic conversion efficiency versus propagation (see text for details).

4.2.2 Generation of high-order harmonics by intensity spikes

A filament with a length of about 30 cm is created by focusing the pulses from the amplifier into the SIGC filled with 1000 mbar of argon. Due to the occurrence of intensity spikes at certain positions, it is possible to generate high-order harmonics which are coupled out from the SIGC through the truncating pinholes. In argon at atmospheric pressure, absorption of the harmonic radiation is more relevant than other phase-matching contributions. The absorption length is about $13 \mu\text{m}$ at the 17th harmonic and $32 \mu\text{m}$ at the 23rd harmonic [Hen93]. Thus, the harmonics originate directly from the position of the truncating pinhole and can be interpreted as a nonlinear measure of the local electric field. Figure 4.3(a) shows spectra of harmonics generated at different positions within the filament. The propagation distance z denotes the path length between the focusing mirror and the first pinhole of the SIGC. While the filaments extends over ~ 30 cm, two confined regions, A and B, are identified, where the yield of high-order harmonics is high. The XUV spectrum in the first region at propagation distance around $z = 211$ cm exhibits discrete har-

monics, while the region around $z = 219$ cm features a continuous spectral shape. At a pinhole position smaller than 207 cm and greater than 223 cm no significant harmonic contributions are measured, which is attributed to a low local intensity in the filament as discussed below. Single spectra from both regions, A and B, are presented in Fig. 4.3(b). The spectra extend both to a similar cutoff energy, which allows to estimate a lower bound for the driving laser intensity in these regions. Assuming the cutoff law (see Sec. 2.3.1) and a wavelength of 780 nm, a cutoff at the 23rd harmonic corresponds to an intensity of 1.2×10^{14} W/cm². The best conversion efficiency is measured to 1.3×10^{-7} for the harmonic radiation in the range from 30 to 50 nm via an XUV diode. Figure 4.3(c) shows the harmonic conversion efficiency versus propagation, measured by an MCP behind the XUV monochromator in the zeroth order. The ordinate axis is rescaled to the measured maximum conversion efficiency assuming a linear response of the MCP. Both regions, A and B, feature an equal total energy content of about 0.1 nJ per pulse.

The generation of high-order harmonics in the regions A and B constitutes the occurrence of intensity spikes in the filament. For propagation distances shorter than 207 cm and longer than 223 cm, the intensity is clamped at the ionization threshold, and is not sufficient for HHG. The first intensity spike is formed at a position $z \approx 211$ cm and generates well resolved harmonics which corresponds to a driving pulse of several cycles. The spike propagates a few centimeter before it undergoes another defocusing-refocusing-cycle. A second spike occurs at a propagation distance of $z \approx 219$ cm. The observation of a continuous harmonic spectrum may indicate that the second spike emerges with an even shorter pulse duration.

Since the CEO phase of the used laser system is not stabilized, the spectra, shown in Fig. 4.3, are averaged over many shots of different CEO phases. As illustrated in Sec. 2.3.4, the CEO phase determines the shape of the XUV spectrum generated by few-cycle pulses. While the harmonic spectrum for one CEO phase may show resolved harmonic orders, another CEO phase could yield a continuous spectrum which can be used for IAP generation. However, averaging the spectra over different CEO phases always yields a continuous shape. To ensure that the continuous harmonic spectra from region B could be applied to IAP production, single-shot spectra are recorded. Figure 4.4 shows the single-shot spectra, which are extracted from region A and B, respectively. While the spectra from the first region A exhibit well resolved harmonics, the continuous harmonic structure is preserved for spectra of region B. Little variation in the measured single-shot spectra are observed which suggests a minor influence of the initial CEO phase on the CEO phase of the second spike. This corresponds to theoretical predictions assigning this effect to properties of the refocusing process [Gaa09]. The CEO phase of the refocused sub-pulse is determined by the rapid refocusing process rather than by the initial CEO phase of the driving pulse. A CEO-phase independent generation of a contin-

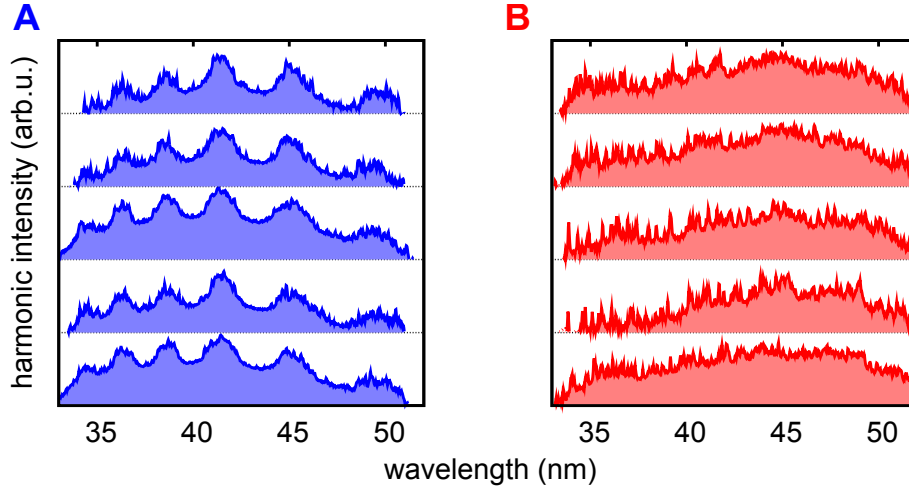


Figure 4.4: Single-shot spectra from the two regions A and B, as labeled (cf. Fig. 4.3). For each region, five consecutive spectra are shown, generated from every 30th laser pulse with different CEO phases.

uous harmonic spectrum would suggest a possible IAP production directly from the filament without the need for a CEO-phase stabilization of the driving laser system. This could strongly simplify the setup for IAP production combining CEO-phase stabilization, pulse compression and HHG in a single filamentation stage. To verify that the sub-pulses in region B are independent of the initial CEO phase, a future experiment could directly measure the CEO phase of the emerging IR pulses using single-shot electron spectra [Wit09]. Note that the occurrence of spatial averaging effects cannot be excluded in the above measurements of the harmonic spectra. A spatial chirp in the harmonic radiation may smear out the measured spectra due to averaging over the detector area, and may thus result in an apparently continuous spectrum. Thus, spatially resolved measurements of the spectrum are necessary to exclude these averaging effects. However, the entrance slit of the McPherson spectrometer, used for the single-shot measurements, has a height of 2 mm and a width of a few 10 μm . Thus, the recorded harmonic spectra are averaged over a relatively small area of the harmonic beam profile, and effects from a spatial chirp should be strongly reduced.

The harmonics are emitted in a nearly Gaussian beam as shown in the profile measurements in Fig. 4.5, which are recorded in 1.5 m distance from the exit pinholes of the SIGC. Assuming a point source, a divergence angle of 1.4 mrad is estimated for the harmonic beam in the first region A, and 1.7 mrad in the region B. The divergence of the harmonic beam is similar to the measured divergence of the fundamental beam of 1.4 mrad before the onset of the filament. Depending on the dimensions of the pinholes, the divergence of the transmitted fundamental beam is between

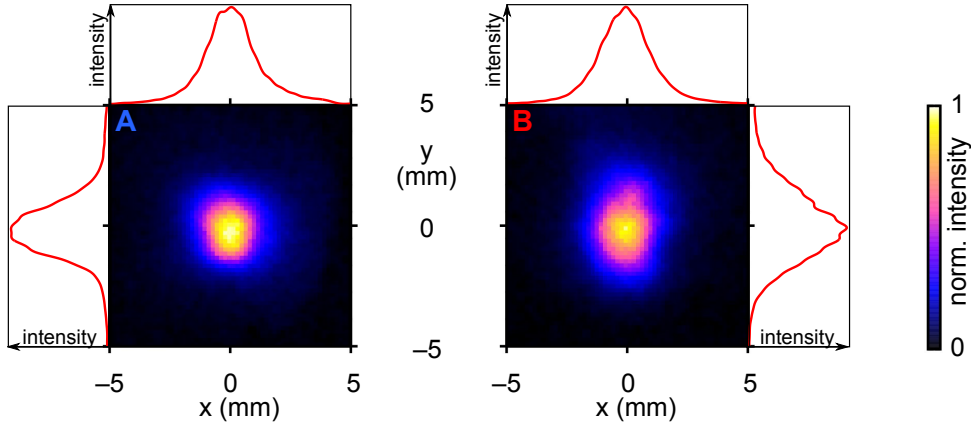


Figure 4.5: Profile of the total harmonic radiation from two regions A and B, as labeled (cf. Fig. 4.3). The red solid lines show horizontal and vertical sections of the profile through the maximum intensity. The curves are smoothed over 0.2 mm to reduce artifacts from the mesh of the aluminum foil. For the same reasons, the resolution of the color maps is reduced.

1.7 mrad and 3.4 mrad due to diffraction. It was shown [Sal94] that the divergence of the harmonic beam does not follow the divergence $\theta_q = \theta_1/\sqrt{q}$ of the perturbation theory with the divergence angle θ_1 and θ_q of the fundamental and harmonic beam, respectively. The divergence of the harmonics is expected to be smaller compared to the divergence of the fundamental beam by a factor between 3 to 9 depending on the phase-matching conditions [Sal96]. In contrast, a similar divergence of the harmonic beam is observed compared to the divergence of the fundamental beam. This might be explained by the rapid and steep refocusing process forming the intensity spike in the filament, and which in turn, gives rise to HHG. This refocusing of the trailing sub-pulse occurs with a larger divergence yielding also a harmonic beam of an unexpected large divergence angle.

In summary, strong indications for intensity spikes inside a femtosecond filament has been found by measuring their high-order harmonic spectra. Two spikes were identified, whereby the second spike generates a continuous harmonic spectrum which show little variations for different CEO phases of the initial laser pulse. The measured conversion efficiency is comparable to the conversion efficiency of traditional gas targets [Bra00, Ede04], and the harmonics are emitted in a nearly Gaussian beam.

4.2.3 Numerical results

Large-scale numerical calculations with sub-optical-cycle precision are performed by Mette B. Gaarde and Arnaud Couairon [Gaa08, Gaa09], including both the filamentation dynamics and the generated harmonic radiation, to support the interpretation of the experimental results. For a description of the simulation method, please refer to Appendix B.2. Figure 4.6 shows the simulated evolution of the peak intensity in the filament and the resulting harmonic spectra over the propagation distance. The spectra shown in Fig. 4.6(b) are integrated radially and averaged over different CEO phases and three different intensities for comparison with the experiment. In addition, they are corrected by the response of the spectrometer and the transmission of the aluminum filter. The onset of the filament is observed 2 m behind the focusing mirror with a clamped peak intensity of about $0.8 \times 10^{14} \text{ W/cm}^2$ (cf. Fig. 4.6(a)). This gives rise to weak and well resolved harmonics, seen in Fig. 4.6(b) at positions $z < 210 \text{ cm}$. The first intensity spike with a peak intensity of $0.9 \times 10^{14} \text{ W/cm}^2$ is formed at $z \approx 212 \text{ cm}$ (region A) generating well resolved harmonics on the axis as shown in Fig. 4.6(c). Due to a spatial chirp, the radially integrated spectra of Fig. 4.6(b) smear out. Around the propagation distance $z = 219 \text{ cm}$ (region B), a

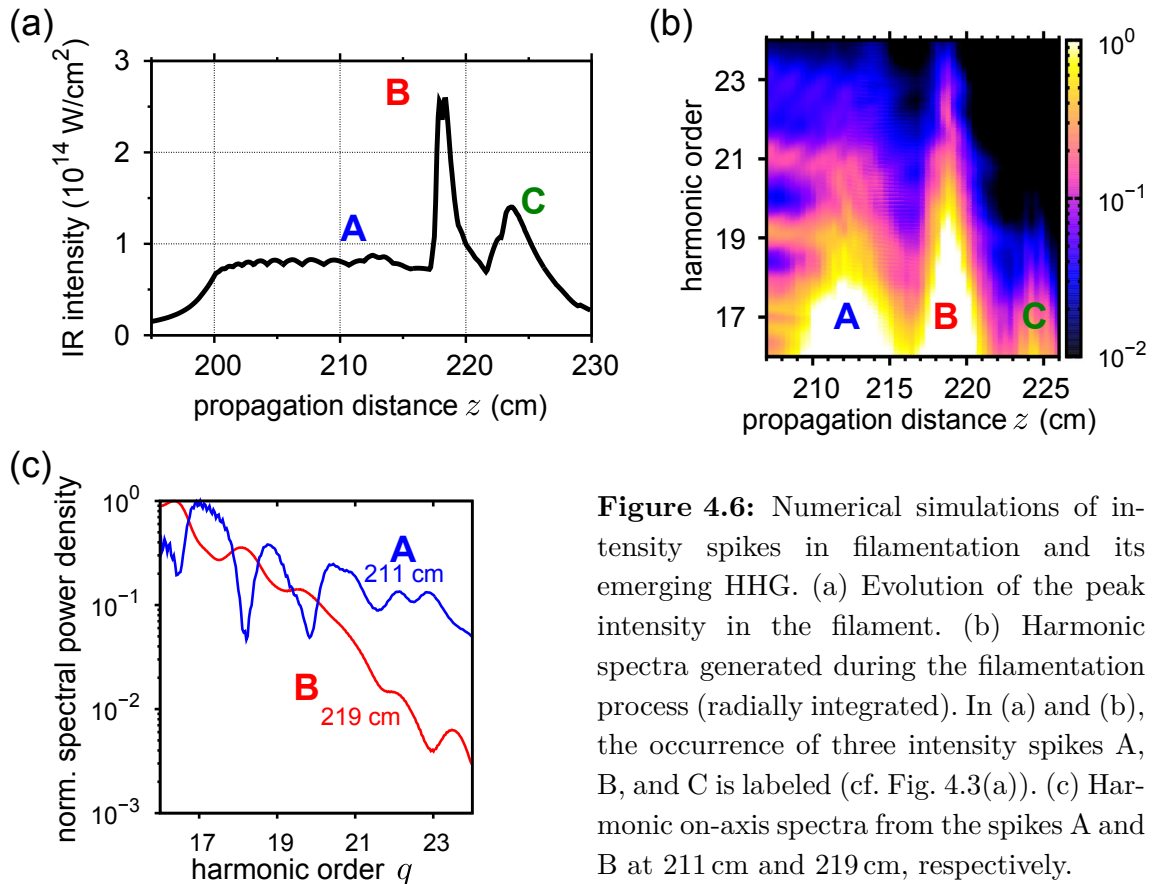


Figure 4.6: Numerical simulations of intensity spikes in filamentation and its emerging HHG. (a) Evolution of the peak intensity in the filament. (b) Harmonic spectra generated during the filamentation process (radially integrated). In (a) and (b), the occurrence of three intensity spikes A, B, and C is labeled (cf. Fig. 4.3(a)). (c) Harmonic on-axis spectra from the spikes A and B at 211 cm and 219 cm, respectively.

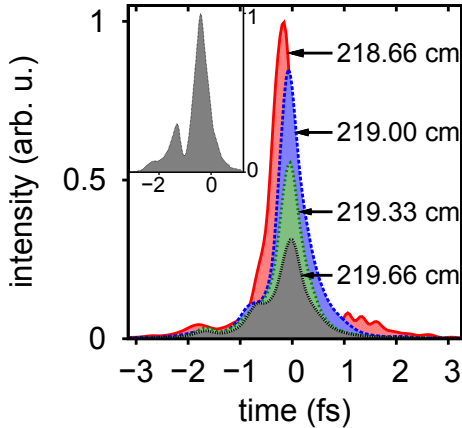


Figure 4.7: IAPs generated in the filament by spike B. The initial laser pulses are assumed to have a fixed CEO phase. Their generated harmonic spectrum around 219 cm is filtered by blocking harmonics below the 16th order. The inset shows the generated attosecond pulses for an initial CEO phase changed by $\pi/2$.

high peak intensity above $2.5 \times 10^{14} \text{ W/cm}^2$ is obtained for the second spike. An ultra-short sub-pulse of near single-cycle duration is formed in the trailing edge of the pulse, which generates a continuous XUV spectrum. Both, on-axis and the radially integrated spectra exhibit a continuous shape, showing no spatial chirp. Because of a strong blue shift of the fundamental frequency in the sub-pulse [cf. Cha06, Gaa09], the cutoff of the spectrum remains at a similar energy as for the first spike. Before the filament breaks up, a third spike occurs in the simulation at a position $z \approx 224 \text{ cm}$ (region C), which is not observed in the experiment. Its contribution to HHG is only minor for radially integrated spectra, since its intensity is high only on the axis. Note that in the following, the intensity spikes are labeled according to the regions A, B, and C, where they are located.

An excellent agreement is obtained between the measurements (cf. Fig. 4.3) and the simulations (cf. Fig. 4.6). The simulations reproduce the existence of the intensity spikes and their relative spacing. Moreover, the highest harmonics, which are generated by the simulated spikes, agree with the experimental observations. Note that excellent agreement of the simulations with the experiment is also found in the power spectra of the fundamental pulses [Sch11]. The minor HHG contribution of the third spike as well as an earlier termination of the experimental filament may explain the absence of the third spike in the experiment.

The continuous spectrum, which is generated by the second spike B around a position $z = 219 \text{ cm}$, can be used for the production of IAPs directly from the filament without additional pulse compression. Applying a spectral filter which blocks harmonics lower than the 16th order, the simulation yields an IAP with duration of approximately 500 as and an energy of about 0.02 nJ. Since the SFA underestimates the harmonic power by a factor between five to ten [Gaa02, Gaa08], the calculated pulse energies are in good agreement with the measured energies when taking this factor into account. Figure 4.7 shows the propagation of the IAP in the filament. It remains robust over a distance of more than 1 cm, which can be seen in the

small change of its temporal shape during the propagation. Similar to the marginal change in the single-shot spectra in region B, the time structure of the XUV field depends only slightly on the CEO phase of the initial laser pulse for the presented conditions. Changing the initial CEO phase by $\pi/2$ with respect to the above case, gives rise to an IAP with a small satellite, as illustrated in the inset in Fig. 4.7. However, at different conditions, such as a changed intensity or pressure, a dependence on the initial CEO phase is obtained in the simulations. Thereby, a changed initial CEO phase results in two or three attosecond pulses rather than one. A detailed future experimental study on single-shot harmonic spectra or on single-shot CEO-phase measurements versus intensity and pressure could clarify the CEO-phase dependence observed in the simulations. Conditions might be identified in such an experiment, where a robust production of IAPs directly in the filament is possible without previous CEO-phase stabilization of the laser system.

4.2.4 Control of the intensity spikes

In this section, the properties of the intensity spikes in the experiment are systematically investigated by a variation of the chirp, the energy and the beam profile of the driving laser pulses at different pressures of the nonlinear medium. The beam profile is changed by using different diameters D of the first aperture before the focusing mirror (cf. Fig. 4.2). This modifies the pulse energy, which can be adjusted separately by an attenuator placed between the aperture and the focusing mirror. The intensity spikes are analyzed via the generated averaged XUV spectra versus focus position (cf. Fig. 4.3) regarding their location and intensity. Thereby, it is exploited that the first spike A generates well resolved harmonics while the second spike B generates a continuous spectrum. A detailed description of the analysis method is found in Appendix A.4. Note that the laser parameters have changed since the experiments of the previous section due to a declined quality of the beam profile and enhanced output power.²

Figure 4.8 shows the positions z_A and z_B of the intensity spikes A and B, respectively. The spikes appear for a wide range of pressures and chirp values, which demonstrates the robustness and universality of intensity spikes in filamentation. At a fixed chirp value $\beta \approx 0 \text{ fs}^2$ of the input pulses, the pressure is varied from 600 to 1000 mbar which induces a shift of the spike position, see Fig. 4.8(a). Below a pressure of 700 mbar, the second spike B disappears which is attributed to an earlier termination of the filament at a low pressure. The shift can be explained by changing self-focusing conditions due to the intensity dependent refractive index $n_2(p)$, which increases linearly with the pressure p of the nonlinear medium [Bör10]. This affects

²The diodes of the pump-laser for the amplifier system have been replaced in the meantime.

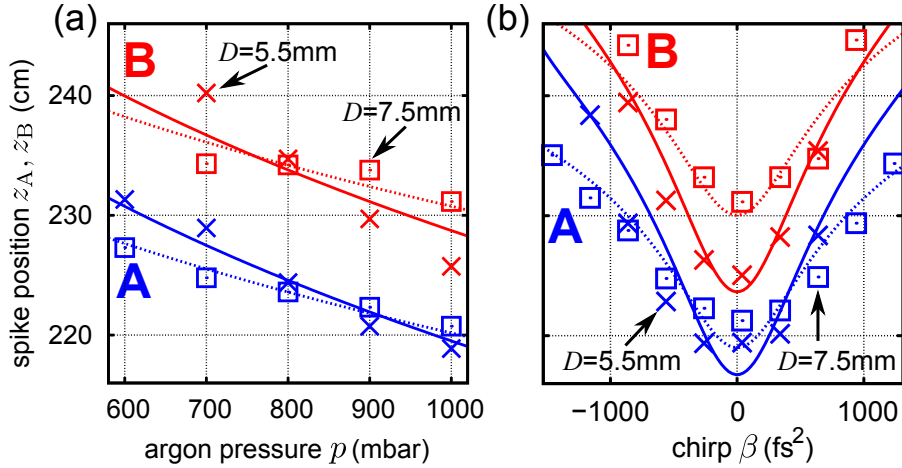


Figure 4.8: Position control of the intensity spikes by variation of different experimental parameters. (a) Positions z_A and z_B of the intensity spikes versus pressure of the nonlinear medium at zero chirp. The lower blue symbols show the experimental positions of spike A for two diameters of the aperture $D = 5.5$ mm (\times) and $D = 7.5$ mm (\square). The red symbols illustrate the positions of spike B. (b) Positions z_A and z_B of the intensity spikes versus chirp at 1000 mbar argon. The lines in (a) and (b) correspond to the calculated spike positions z_A and z_B according to the beam-collapse model, Eq. (4.1), with adjusted offset L_A and L_B for spike A and B, respectively (see Tab. 4.1). The solid lines correspond to an aperture diameter $D = 5.5$ mm, dashed lines correspond to $D = 7.5$ mm.

the distance $L_{c,f}(p)$ until the beam collapses due to self-focusing as introduced in Sec. 2.1.1, Eq. (2.5). Let us consider $L_{c,f}(p)$ to be the onset of the filament. Assuming the location of the spikes at a relative offset L_A and L_B , respectively, their absolute positions are given by

$$z_i = L_{c,f}(p) + L_i \quad \text{with } i = A, B. \quad (4.1)$$

Using parameter values from the experiment,³ this model reproduces the experimental curves for adjusted values of L_A and L_B as listed in Tab. 4.1(a) (lines in Fig. 4.8(a)). A good agreement is observed between the spike positions and the model. The absolute values of about half a meter for the fitted offsets L_A and L_B are apparently large when assuming the start of the filament at $L_{c,f}$ and compare the offsets to the filament length of about 25 cm to 30 cm, estimated from the plasma fluorescence. This can be explained by a slightly divergent beam from the amplifier and the initial beam quality, which is both not taken into account in the model and leads to a shifted focus position and thus, to a later collapse $L_{c,f}$ in the experiment.

³For an aperture of diameter $D = 5.5$ mm, a beam waist of 2.8 mm and a transmitted pulse energy of 0.75 mJ is used. For $D = 7.5$ mm, a beam waist of 3.9 mm and a transmitted pulse energy of 1 mJ is used. Other parameter values are stated in Sec. 4.2.

D (mm)	L_A (cm)	L_B (cm)	D (mm)	L_A (cm)	L_B (cm)
5.5	50 ± 1	59 ± 2	5.5	47 ± 2	54 ± 1
7.5	42 ± 1	53 ± 1	7.5	41 ± 1	52 ± 2

(a) (b)

Table 4.1: Offset values determined for two aperture diameters D by a fit to the data (a) shown in Fig. 4.8(a), and (b) shown in Fig. 4.8(b) (see text for details).

The pressure dependence is shown for a fixed chirp $\beta \approx 0 \text{ fs}^2$ of the input laser pulses. Keeping the pressure fixed at 1000 mbar, the dependence of the spike position on the chirp of the input pulses is investigated. The chirp is controlled by changing the separation of the compressor gratings in the amplifier system. The applied dispersion is determined from SPIDER measurements while the absolute chirp at the place of the experiment is measured by third harmonic generation in air (see Appendix A.5 for details). Figure 4.8(b) demonstrates that the pulses can be stretched by a positive or negative GDD of $\pm 1000 \text{ fs}^2$ to a duration of approximately⁴ 87 fs before the second spike B vanishes. The first spike A can be observed for an even wider range of chirp values. The lines in Fig. 4.8(b) show the spike positions z_A and z_B obtained using the beam-collapse model, Eq. (4.1), for the experimental parameters. Thereby, a change in the peak power of the pulse is assumed according to

$$P_{\text{peak}}(\beta) = \frac{P_{\text{peak}}(0)}{\sqrt{\tau_p^2 + (2\beta/\tau_p)^2}} \quad (4.2)$$

for an applied GDD value β with pulse duration $\tau_p = 35 \text{ fs}$ (see Appendix B.3 for a derivation). A good agreement of the model with the experimental data is obtained for both spikes. The corresponding fitted offset values are listed in Tab. 4.1(b). As expected from the model, one observes in the experiment a minimum spike position at a chirp value around $\beta = 0 \text{ fs}^2$ which does neither depend significantly on the aperture size nor on the pressure. In average over these parameters, the chirp value at the minimum is determined to $\beta_{\text{min,A}} = (-12 \pm 39) \text{ fs}^2$ for spike A, and to $\beta_{\text{min,B}} = (58 \pm 139) \text{ fs}^2$ for spike B. These values are not significantly different from zero dispersion and cause no considerable change of the pulse duration of the input pulses.

The spike intensity is investigated in dependence on the experimental parameters. Thereby, the spike intensity is evaluated from the power of the high-order harmonics that the spike generates (cf. Appendix A.4), and thus appears on a nonlinear scale. Figure 4.9 illustrates maps of the spike intensity versus pressure and chirp at different diameters of the aperture. The red crosses (\times) indicate the chirp value β_{max} of the

⁴Assuming a Gaussian pulse of 35 fs duration centered at wavelength 780 nm similar to the experiment.

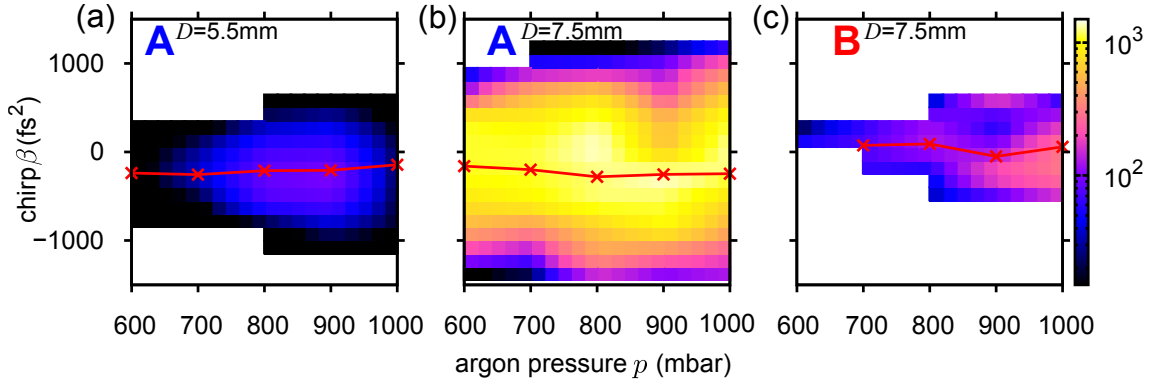


Figure 4.9: Spike intensity at different parameters. The spike intensity, encoded by the color, is determined from the maximum harmonic signal it gives rise to and thus, appears on a nonlinear scale (see text for details). (a)-(c) Maps of the spike intensity versus chirp and pressure at different diameters of the aperture for spike A and B as labeled. The red crosses (\times) show the chirp of the maximum intensity at a fixed pressure determined from a polynomial fit over the intensities versus chirp. The red solid lines serve as a guide to the eyes.

maximum intensity at a fixed pressure, where β_{\max} is determined by a polynomial fit to the spike intensities versus chirp. A chirp value of $\beta_{\max,A} = (-228 \pm 46) \text{ fs}^2$ is obtained which maximizes the intensity of the first spike A with marginal dependence on the pressure and on the diameter of the aperture. The optimal chirp value for the second spike B is determined to $\beta_{\max,B} = (-71 \pm 134) \text{ fs}^2$. A difference between the chirp values at the minimum spike position and at the maximum spike intensity can be observed for the first spike. The absolute intensity of the spike as well as the intensity ratio between the spikes can be adjusted by the diameter of the aperture as shown in Fig. 4.10(a). In the figure, the spike intensities are averaged over pressures in the range between 700 to 1000 mbar, since they exhibit similar values and characteristics as indicated by the error bars. At a small diameter $D \leq 5.5 \text{ mm}$ the intensity of the second spike B exceeds the intensity of the first spike A, while the ratio inverts at diameters $D > 5.5 \text{ mm}$. Note that in addition to the beam profile, the pulse energy changes with the diameter of the aperture as indicated on the abscissa on top of the graph in Fig. 4.10(a). Thus, the origin of the effects cannot be assigned to either the different pulse energy or the different focusing conditions from a changed beam profile. For further investigations, Fig. 4.10(b) shows the spike intensity at a fixed diameter of the aperture while only the pulse energy is varied. The intensity of the second spike B increases rapidly when raising the pulse energy. In contrast, the first spike A changes only marginally. The ratio of the spike intensities increases in favor of the second spike with increasing energy. This differs significantly from the behavior shown in Fig. 4.10(a) when raising the pulse energy by the diameter of the aperture. The rapid intensity enhancement of the second spike for an increased pulse

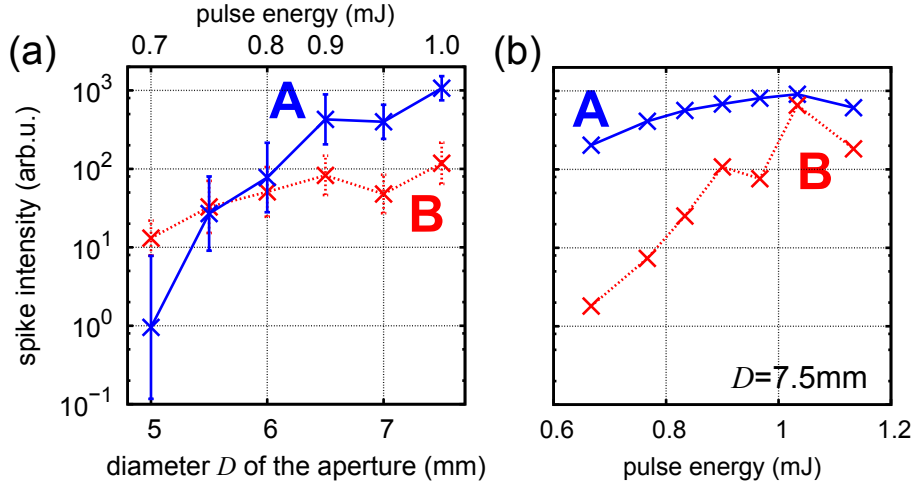


Figure 4.10: Spike intensity versus aperture size and input pulse energy. (a) Spike intensity versus diameter of the aperture for spike A and spike B averaged over different pressures. The error bars indicate the standard deviation from the pressure average. (b) Spike intensity versus energy of the input pulses at an aperture size of 7.5 mm and a pressure of 900 mbar. In both plots, the lines serve as a guide to the eyes and the chirp is set to approximately 0 fs^2 .

energy (Fig. 4.10(b)) can be explained by a higher energy content in the reservoir surrounding the filament. While the first spike is marginally influenced, the filament sustains longer by the greater available energy flux from the reservoir. Thus, at the position z_B of the second spike more energy is available to be refocused onto the axis. Decreasing the diameter D of the aperture (Fig. 4.10(a)), on the one hand, reduces the pulse energy. On the other hand, the focusing becomes less sharp and the beam quality improves. Both the looser focusing conditions and the improved beam quality lead to an enhanced length of the filament as was shown in recent studies [Gei10, Rob09]. These effects agree with the above observations with the same argument that the longer filament provides more energy for the second spike.

In summary, the control of the two measured intensity spikes was demonstrated by variation of experimental parameters, such as the chirp, the energy, and the beam profile of the input pulse, and the pressure of the nonlinear medium. The position of the spikes was investigated versus chirp and pressure, and could be described by a simple model based on self-focusing theory. It was also shown that the absolute intensity as well as the relative intensity between the spikes can be controlled by the stated experimental parameters. The presented results demonstrate that the intensity spikes occur robustly over a wide range of parameter values. Moreover, the high-order harmonic radiation generated from these spikes constitutes a novel method for the investigation of femtosecond filaments.

4.3 Conclusion

The generation of high-order harmonics directly within a filament has been demonstrated. This was attributed to the formation of intensity spikes exceeding the equilibrium intensity of filamentation, which was believed to constitute an upper limit, the *clamping intensity*. One of these spikes occurs on an ultra-short sub-pulse which produces a continuous harmonic structure with little variation for different CEO phases. Numerical simulations are in excellent agreement with the measurements and predict the emergence of IAPs from the continuous XUV spectrum. The spikes appear over wide value ranges of experimental parameters as the beam diameter, the energy and initial chirp of the pulse as well as the pressure of the nonlinear medium. The control of both the spike positions and spike intensities was demonstrated by adjustment of these parameters. The behavior could be explained by a simple model based on self-focusing theory. The presented method provides an ideal tool for the investigation of the spatio-temporal dynamics inside a femtosecond filament. Moreover, the results suggest a new route to IAP production with a simple and compact setup.

Chapter 5

Conclusion and outlook

In this work, high-order harmonic generation (HHG) in a semi-infinite gas cell (SIGC) has been systematically investigated. The optimal phase-matching conditions in xenon and helium have been analyzed on an experimental basis by variation of several parameters, such as focus position and gas pressure. Conditions for a good conversion efficiency of high-order harmonics were identified. For example, placing the focus inside the SIGC close to the exit pinhole enhances the generation of high orders, while low orders are generated efficiently also for a focus position outside the SIGC. A good agreement with numerical simulations allowed for the interpretation of the observed experimental behavior. Absorption in xenon was identified as a limiting factor for efficient HHG and causes a decrease of the harmonic yield for an increasing xenon pressure. The spatial profile of the harmonic radiation has been studied and shows an on-axis and off-axis contribution. By measurements of the coherence time in these two regions, the on-axis contribution was attributed to originate from the short electron trajectory and the outer region was assigned to the long trajectory contributing to HHG. Finally, the spectral splitting and blue shift of harmonic spectral profiles has been investigated at a higher laser intensity. Both adiabatic as well as non-adiabatic splitting was observed using two different experimental setups. The dependence of the adiabatic effect on the focus position, the pressure, and the laser intensity was studied. The non-adiabatic effect was presented for contributions from the long trajectories in comparison to contributions from the short trajectories at different laser intensities. The performed characterization of the SIGC provides a basis for further applications of this geometry. Moreover, the observed spatial separation of contributions from different quantum paths allows for their individual usage or investigation. On the one hand, this could be exploited for the experimental determination of the intensity dependence of the phase slope factors in the single-atom response. On the other hand, the spatial separation of both contributions permits a compensation of the harmonic chirp which is necessary for

the generation of short IAP [Mai03].

After the characterization of HHG and its phase matching in the SIGC geometry, few-cycle driver pulses has been applied to HHG. Therefore, multi-cycle pulses were compressed in argon by spectral broadening in a filament with subsequent dispersion management. Few-cycle driver pulses of 7 fs were obtained which were applied to HHG in different noble gases. The generated harmonic spectrum features spectral broadening and blue shift, which was investigated for different pulse durations. In neon, an XUV super-continuum was obtained with a cutoff at 124 eV. This cutoff energy is well comparable to the cutoff energies of about 120 eV from setups using hollow-core fibers [Gou08, Sch07]. Simulations on the single-atom response has been performed and reproduce the experimental characteristics. The presented results are a promising basis for a generation of IAPs with durations below 250 as after spectral filtering in the cutoff region. Thus, the filamentation setup may provide a simple alternative to the hollow-core fiber technique which is commonly applied to IAP production [Gou08, Hen01, Sch07]. Two color filamentation [Béj08] might be used to enhance the energy content in the high-frequency part of the spectrum allowing for shorter driver pulses for HHG. Moreover, circularly polarized light could be used to enhance the pulse energy after the filament [Var09] which might serve as a high power IAP source for attosecond pump-probe spectroscopy or nonlinear attosecond physics.

Finally, the generation of high-order harmonics directly within a filament has been demonstrated. HHG was attributed to the formation of intensity spikes exceeding the equilibrium intensity of filamentation [Gaa09], in contradiction to traditional filamentation models with clamped intensity [Bra95, Mle98]. One of these spikes produced a continuous harmonic spectrum suggesting that it occurred on an ultra-short sub-pulse. Little variations in the single-shot harmonic spectra generated by this spike suggest that the CEO phase of the spike depends only marginally on the CEO phase of the input pulse. Numerical simulations are in excellent agreement with the measurements supporting the interpretation with regard to the intensity spikes and predict the emergence of IAPs with durations of about 500 as from the continuous XUV spectrum. It was demonstrated that the occurrence of the intensity spikes is robust on a wide range of experimental parameter values. The influence of the beam diameter, the pulse energy, and the initial chirp of the laser-pulses was investigated and explained by a simple model based on self-focusing theory. The presented setup provides an ideal tool for the experimental investigation of femtosecond filamentation, where both the nonlinear yield from HHG as well as the light of the truncated filament can be exploited for analysis. Also lower harmonic orders such as the third harmonic can be used for an investigation. The method permits direct studies of the complex spatio-temporal dynamics inside a filament on

an experimental basis which is so far only possible in numerical calculations. For example, the spectral broadening which occur during the propagation of the IR pulses in the filament can be analyzed [Sch11]. Also the investigation of the CEO phase of the intensity spikes in dependence on the initial CEO phase can be target for future experiments. In the simulations, a dependence of the time structure of the generated attosecond pulses on the initial CEO phase is recognized at different intensities or pressures than used in the experiment. For this purpose, single-shot measurements of the CEO phase [Wit09] of the IR pulses after the truncating pinhole could be performed to study the CEO phase dependence. Further, single-shot measurements of the harmonic spectrum could be performed with a systematic variation of the intensity or pressure. With this issue resolved, the filamentation setup for HHG suggests a simple and compact route to IAP production. Thereby, in dependence on the experimental parameters, such as the position of the truncating pinhole, the source could produce either an IAP or a train of attosecond pulses with an adjustable energy. The CEO-phase dependence might be exploited to even shape the temporal structure of the emerging pulses. Using noble gases with a high ionization potential, the cutoff could be extended and the XUV bandwidth might be increased allowing for shorter IAPs. Thereby, also mixtures of gases are a promising method to tune the generated XUV spectrum by balancing the medium for stable filamentation and optimal HHG. Using two-color co-filamentation [Béj08, Wu09] might be another promising scheme to control the filament with possible influence on IAP production [Ban10].

The attosecond pulses produced inside the filament still need to be characterized. Therefore, a time-of-flight electron spectrometer will be applied in a future experiment to record the kinetic energy of electrons which are released by an attosecond pulse in the presence of the IR field of the driving laser. The existence of both attosecond pulse trains and IAPs can be verified from this measurement by the RABITT¹ technique [Mul02] or by the FROG-CRAB² technique [Mai05] under simultaneous characterization of their temporal shape. A similar setup could then be applied for attosecond pump-probe experiments [Hen01].

¹reconstruction of attosecond beating by interference of two-photon transitions

²frequency-resolved optical gating for complete reconstruction of attosecond bursts

Appendix A

Experimental methods

A.1 The laser system

The laser amplifier system, used throughout in this work, is a commercial system (DragonTM, Kapteyn-Murnane Laboratories, Inc.) which is based on the chirped-pulse amplification technique [Str85]. An Titanium-Sapphire (Ti:Sa) oscillator delivers ultra-short pulses of 15 fs pulse duration and 6 nJ pulse energy generated by mode-locking. The dispersion within the oscillator is controlled via a prism sequence. The nanojoule pulses are stretched within the amplifier to about 200 ps applying a grating stretcher [Mar87]. A pockels-cell samples the 80 MHz repetition rate of the oscillator pulses down to 3 kHz by picking pulses via an electro-optical effect. After fifteen passes through a Ti:Sa-crystal in the amplifier ring, the pulse energy is scaled up by a factor of one million. A grating compressor [Tre69] reverses the dispersion of the stretcher, and yields pulses with energy between 1 and 1.3 mJ and duration of about 35 fs. The beam quality of the output beam is measured to have a $M^2 \approx 1.3$ [Sch09a].

A.2 Spatially resolved measurement of the coherence time

In order to identify the contributions from the different trajectories in the SIGC setup, measurements of the coherence time $T_{\text{coh}} \propto 1/\alpha$ are performed in the on-axis and off-axis spatial regions, respectively (cf. Sec. 2.4.3.1). Therefore, two phase-locked harmonic sources with adjustable time delay are realized in the SIGC by installing an interferometer before the focusing lens (cf. Sec. 3.1.1), where one

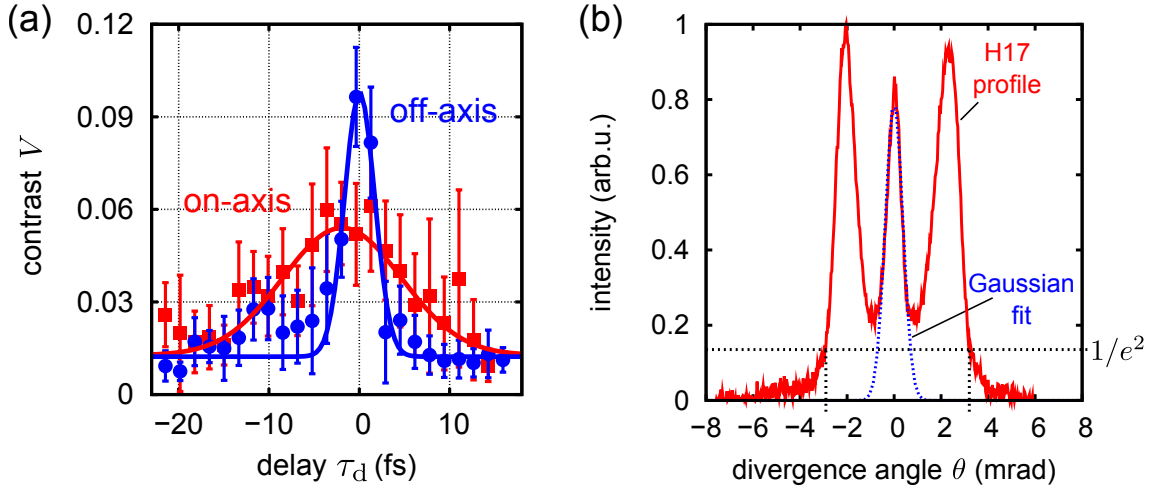


Figure A.1: (a) Intensity contrast of the spatial interference fringes for the 17th harmonic versus the delay between the interferometer arms at a focus position $z_f = -10$ mm and a pressure of 20 mbar (see text for details). The contrast V is determined for the on-axis (■) and off-axis (●) region, respectively (cf. Fig. 3.9). The error bars indicate the standard deviation of the contrast evaluated over multiple measurements. The solid lines illustrate a fit to a Gaussian function to determine the coherence time via the FWHM. (b) Intensity profile (red solid line) of the 17th harmonic in 20 mbar xenon at a focus position $z_f = -10$ mm. The blue dashed line is a Gaussian fit to the center part of the profile.

arm has been misaligned in order to generate a double focus. The harmonic radiation from both harmonic sources interfere in the far field behind the spectrometer with the emergence of interference fringes in the spatial profile of the individual harmonic orders. These fringes are analyzed by their intensity contrast $V = (I_{\max} - I_{\min}) / (I_{\max} + I_{\min})$. The contrast is evaluated for different delays τ_d between the two arms of the interferometer, which yields the coherence time T_{coh} by the FWHM of the contrast function $V(\tau_d)$ (cf. Sec. 2.4.3.1). Figure A.1(a) illustrates the contrast V of the 17th harmonic versus delay τ_d measured in the on-axis and off-axis region, respectively. From a Gaussian fit to the contrast $V(\tau_d)$, the coherence time T_{coh} is determined to (15.5 ± 2.9) fs in the on-axis region and to (3.9 ± 0.6) fs in the off-axis region.

From the measured harmonic profile of the 17th harmonic in 20 mbar xenon (cf. Fig. A.1(b)), the divergence angle is estimated via the $1/e^2$ -radius to $\theta_{\text{short}} \approx 0.74$ mrad and $\theta_{\text{long}} \approx 3.05$ mrad of the on-axis and off-axis radiation, respectively. The larger divergence of the long trajectory contribution is in accordance with the relation $\theta \propto \alpha$, derived in a geometrical optics approximation [Gaa99]. The ratio $\nu_\theta = \theta_{\text{long}} / \theta_{\text{short}}$ is determined to $\nu \approx 4.1$.

A.3 Single-shot measurements

Since the CEO phase of the laser system is not stabilized, measurements of XUV spectra generated from a single laser shot need to be performed. Since the phosphor screen of the McPherson spectrometer has a decline time of about 10 ms, spectra are averaged over 30 laser shots at a laser repetition rate of 3 kHz even when reducing the integration time below 10 ms. In contrast, the MCP of the spectrometer can be switched rapidly by gating the high voltage. Therefore, a pulse generator (PVX-4140, Directed Energy, Inc.) is applied, which is triggered by the fraction of the laser repetition rate to ensure that a delay of 10 ms is maintained between two recorded shots. The pulse generator switches between two high-voltage sources (PS350/5000V-25W, Stanford Research Systems, Inc.), one at a high voltage level (≈ 2.3 kV) to be sensitive to the harmonic radiation, and the other at a level of 50% with no contributions to the signal.

A.4 Analysis of the intensity spikes

In this section, the analysis method of the systematic investigation of the intensity spikes in Sec. 4.2.4 is introduced. The two intensity spikes A and B can be identified by their harmonic structure, since the first spike A generates well resolved harmonics while the second spike B generates a continuum. This observation is valid for all tested parameters where both spikes are visible.

XUV spectra are recorded versus focus position as shown for example in Fig. A.2(a) and also in Fig. 4.3(a). Each recorded XUV spectrum is evaluated in the Fourier domain for the strength of the peak structure and is tagged as either discrete or continuous. Figure A.2(b) shows the Fourier transform of the data in Fig. A.2(a) versus wavelength. The green rectangle marks the region of interest where it is decided whether a single spectrum is considered discrete or continuous. Above a certain threshold, the spectrum is considered as discrete and attributed to spike A. Furthermore, the integrated spectra are analyzed versus the focus position for each spike regarding their center of gravity and their maximum integrated yield as shown in Fig. A.2(c). Thus, the location of the spike as well as its maximum intensity is obtained.

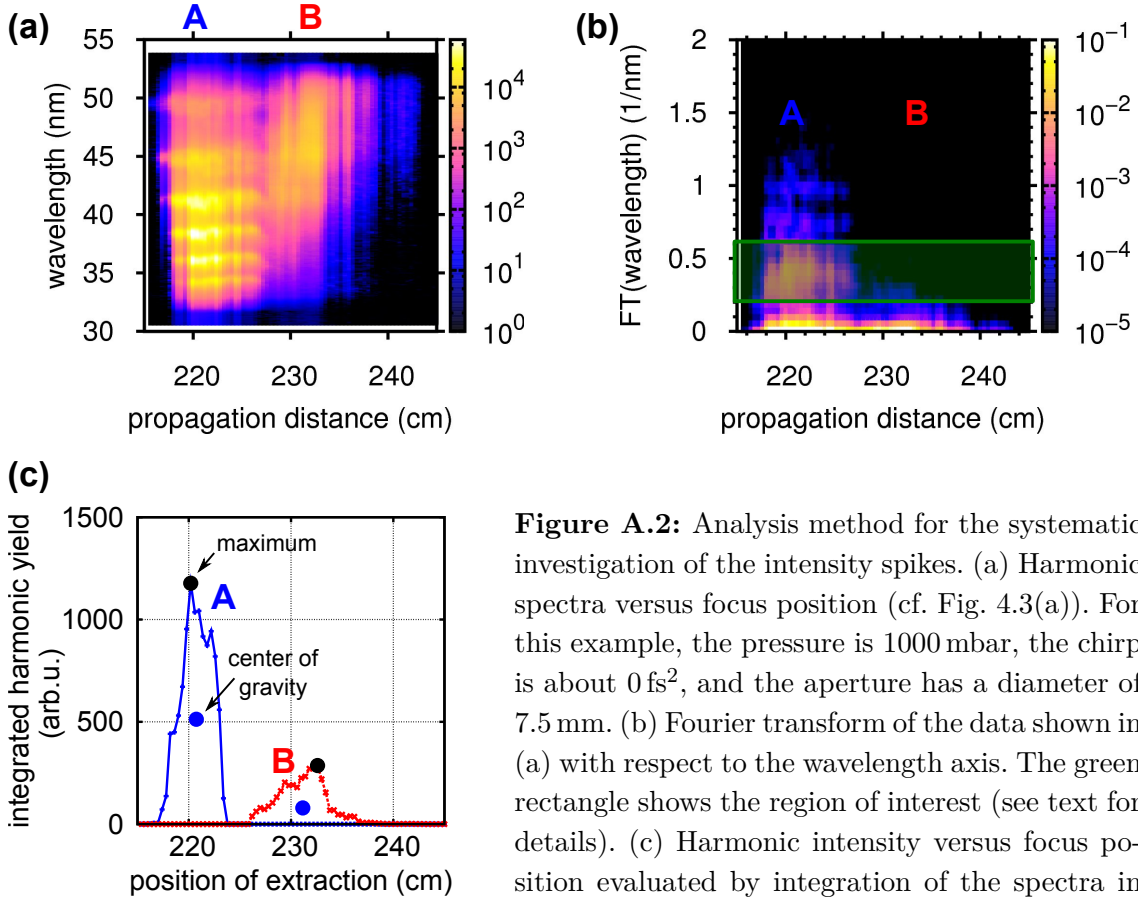


Figure A.2: Analysis method for the systematic investigation of the intensity spikes. (a) Harmonic spectra versus focus position (cf. Fig. 4.3(a)). For this example, the pressure is 1000 mbar, the chirp is about 0 fs^2 , and the aperture has a diameter of 7.5 mm. (b) Fourier transform of the data shown in (a) with respect to the wavelength axis. The green rectangle shows the region of interest (see text for details). (c) Harmonic intensity versus focus position evaluated by integration of the spectra in (a) over the wavelength (divided by the number of points). The spectra of each spike A and B are considered separately and are analyzed regarding maximum and center of gravity.

A.5 Calibration of the absolute chirp

The initial chirp of the pulses are controlled by the separation of the gratings in the compressor of the CPA-system. From SPIDER measurements at different compressor settings, the linear dependence between the separation of the gratings and the average GDD which is applied to the pulses is calibrated (Fig. A.3(a)). A calibration factor of $(3.00 \pm 0.05) \text{ fs}^2/\mu\text{m}$ was determined by a linear fit up to a relative grating position of $400 \mu\text{m}$. The simulated curve shows the linear dependence of a compressor with gratings of 1250 lines/mm placed in an angle of incidence of 38° .

The position of the zero chirp is determined behind the entrance window of the SIGC. Therefore, a curved mirror ($f \approx 50 \text{ mm}$) is used to focus the pulses in air. The generated third harmonic radiation is recorded by a spectrometer (Avantes) behind two mirrors with high reflectivity for the third harmonic and low reflectivity

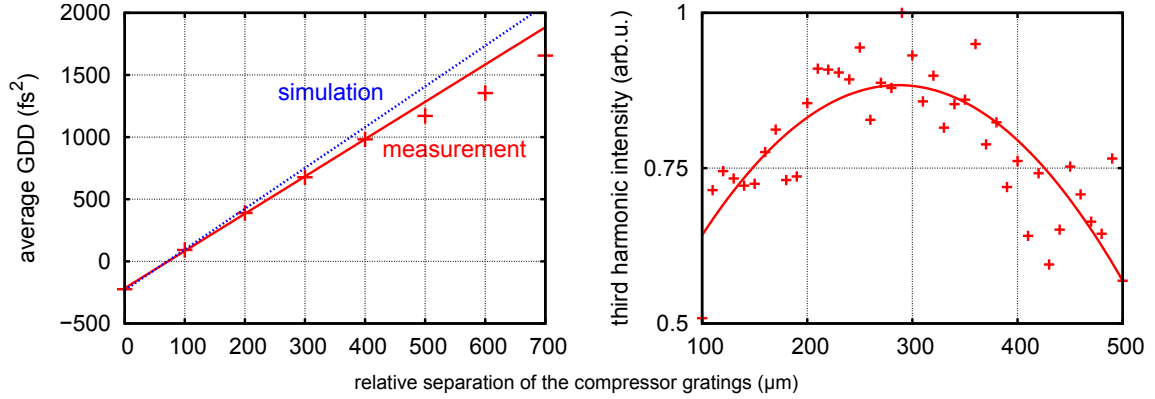


Figure A.3: Calibration of the chirp of the laser pulses from the relative separation of the compressor gratings. (a) Calibration of the linear dependency. The red solid line shows a linear fit to the measured data. The blue dotted line indicates simulated data with estimated values of the grating. (b) Calibration of the absolute chirp value behind the entrance window to the SIGC from the third harmonic conversion efficiency in air.

for the fundamental. The pulse energy is reduced by an attenuator to assure, that no blue shift is observed in the spectra. The integrated spectra versus separation of the compressor gratings is plotted in Fig. A.3(b). By a parabolic fit, the position of highest conversion to the third harmonic is estimated to $(287 \pm 7) \mu\text{m}$. This is defined as the *zero* separation yielding an initial chirp of the pulses of 0 fs^2 .

Appendix B

Calculations

B.1 Genetic fitting algorithm

The simulations are performed with parameter sets mimicking the experimental conditions. For achieving optimal matching between experiment and simulation results, a genetic fitting algorithm [Bar54, Hol75] is applied that allows for the optimization of certain parameters of the set.

The principle of a genetic algorithm is sketched in Fig. B.1. Starting from an initial parameter set (generation 0), a certain number of children parameter sets are created on the basis of the initial parameter set (*reproduction*) by adding a Gaussian random number to every parameter value of the set (*mutation*). The new sets of parameters (generation 1) are evaluated, which means here to run the phase-matching simulation and evaluate the distance to the experimental values. This distance is a measure of the so called *fitness* of a parameter set, and should be optimized by the fitting algorithm. Only the fittest parameter sets are kept as parents for the next generation (*selection*). Thereby, also the parent from the previous generation is considered as a new parent depending on its fitness. The new parameter sets (generation 2) are created each by crossing two parameter sets from the parents. This is realized by randomly choosing two parent parameter sets, and, for each parameter of the new child set, taking the (mutated) value from either the one set or the other. The new children are again evaluated and the procedure of selection and reproduction starts over again. The fitting algorithm can be aborted when the best fitness of the generations converges.

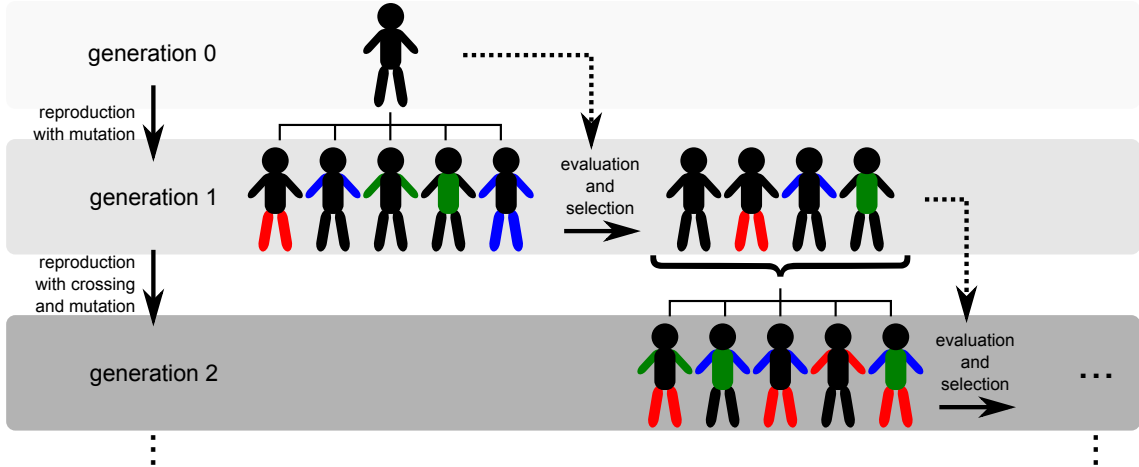


Figure B.1: Principle of a genetic fitting algorithm (see text for details).

B.2 Numerical simulations of harmonic generation in a filament

The numerical calculations for generation of high-order harmonics within a filament (cf. Sec. 4) were performed by Arnaud Couairon and Mette B. Gaarde as described in the following [Ste11]. The coupled Maxwell wave equation and the time-dependent Schrödinger equation are solved with a resolution below an optical cycle of the fundamental field. The wave equation is transformed into a unidirectional propagation equation, which is first order in the propagation coordinate and is solved via space-marching in the frequency domain (see [Gaa08, Gaa09] for details). Thereby, all frequencies are considered comprising the laser and harmonic spectra. For each plane in the propagation direction, the time-dependent laser electric field is computed via inverse transform of its spectrum and used to calculate the (time-dependent) nonlinear source terms as described below. The source terms are Fourier transformed back into the frequency domain and used to propagate the laser and harmonic frequencies to the next plane in the propagation direction. For the laser field, the nonlinear terms include the third order response, described by the third-order susceptibility $\chi^{(3)}$, and the ionization driven terms, which are evaluated using intensity-dependent ionization rates calculated as described in [Ilk92]. The ionization terms include the nonlinear absorption via multiphoton ionization, and the ionization-driven plasma refractive index. For the harmonic field the source term is given by the time-dependent dipole moment, calculated using the strong-field approximation [Lew94], multiplied by the atomic density. Absorption (for frequencies above the ionization threshold) and linear dispersion are treated with frequency-dependent coefficients taken from [Hen93, L'H90]. The temporal structure of the

emerging harmonic radiation is ensured to no change in its shape when applying a pressure gradient over 1 cm as in the experimental setup.

B.3 Peak-power reduction caused by dispersion

In this section, the influence of a GDD on the pulse peak power is computed. The result below is used in Sec. 4.2.4 as input for the collapsing beam model.

Assuming a Gaussian pulse with envelope power function

$$\frac{1}{2}nc\varepsilon_0 |\mathcal{E}(t)|^2 = \frac{P_{\text{peak}}}{\sqrt{\frac{\pi}{2}} \tau_p} e^{-2t^2/\tau_p^2} \quad (\text{B.1})$$

with pulse duration of τ_p and peak power of P_{peak} . The corresponding power spectrum reads

$$\frac{1}{2}nc\varepsilon_0 |\mathcal{E}(\omega)|^2 = \frac{P_{\text{peak}}\tau_p}{\sqrt{2\pi}} e^{-\omega^2\tau_p^2/2}, \quad (\text{B.2})$$

where the carrier frequency has been omitted for simplicity. Applying a constant GDD value β , an additional quadratic phase in the electric field is obtained:

$$\phi_2(\omega) = -\frac{\beta}{2}\omega^2. \quad (\text{B.3})$$

Back transforming the spectral electric field $\mathcal{E}(\omega)e^{i\phi_2}$ into the time domain yields

$$\frac{1}{2}nc\varepsilon_0 |\mathcal{E}(t, \beta)|^2 = \frac{P_{\text{peak}}}{\sqrt{\frac{\pi}{2}} \tilde{\tau}_p} e^{-2t^2/\tilde{\tau}_p^2} \quad (\text{B.4})$$

with the effective pulse duration

$$\tilde{\tau}_p = \sqrt{\tau_p^2 + \left(\frac{2\beta}{\tau_p}\right)^2}. \quad (\text{B.5})$$

Thus, the peak power of the chirped pulse is reduced according to

$$P_{\text{peak}}(\beta) = \frac{P_{\text{peak}}(0)}{\sqrt{\tau_p^2 + \left(\frac{2\beta}{\tau_p}\right)^2}}. \quad (\text{B.6})$$

Bibliography

- [Ago04] P. Agostini and L. F. DiMauro. The physics of attosecond light pulses. *Rep. Prog. Phys.*, 67: 813–855, 2004.
- [Alt96] C. Altucci, T. Starczewski, E. Mevel, C.-G. Wahlström, B. Carré, and A. L’Huillier. Influence of atomic density in high-order harmonic generation. *J. Opt. Soc. Am. B*, 13: 148, 1996.
- [Alt98] C. Altucci, C. Delfin, L. Roos, M. B. Gaarde, A. L’Huillier, I. Mercer, T. Starczewski, and C.-G. Wahlström. Frequency-resolved time-gated high-order harmonics. *Phys. Rev. A*, 58(5): 3934–3941, Nov 1998.
- [Alt99] C. Altucci, R. Bruzzese, C. de Lisio, M. Nisoli, S. Stagira, S. De Silvestri, O. Svelto, A. Boscolo, P. Ceccherini, L. Poletto, G. Tondello, and P. Villoresi. Tunable soft-x-ray radiation by high-order harmonic generation. *Phys. Rev. A*, 61: 021801(R), 1999.
- [Alt08] C. Altucci, R. Esposito, V. Tosa, and R. Velotta. Single isolated attosecond pulse from multicycle lasers. *Opt. Lett.*, 33(24): 2943–2945, 2008.
- [Amm86] M. V. Ammosov, N. B. Delone, and V. P. Krainov. Tunnel ionization of complex atoms and of atomic ions in an alternating electromagnetic field. *Sov. Phys. JETP*, 64: 1191, 1986.
- [Bak06] S. Baker, J. S. Robinson, C. A. Haworth, H. Teng, R. A. Smith, C. C. Chirila, M. Lein, J. W. G. Tisch, and J. P. Marangos. Probing proton dynamics in molecules on an attosecond time scale. *Science*, 312(5772): 424–427, 2006.
- [Bal97] P. Balcou, P. Salières, A. L’Huillier, and M. Lewenstein. Generalized phase-matching conditions for high harmonics: The role of field-gradient forces. *Phys. Rev. A*, 55(4): 3204–3210, Apr 1997.

- [Ban10] H. C. Bandulet, D. Comtois, E. Bisson, A. Fleischer, H. Pépin, J. C. Kieffer, P. B. Corkum, and D. M. Villeneuve. Gating attosecond pulse train generation using multicolor laser fields. *Phys. Rev. A*, 81(1): 013803, Jan 2010.
- [Bar54] N. A. Barricelli. Esempi numerici di processi di evoluzione. *Methodos*, pages 45–68, 1954.
- [Bec01] A. Becker, N. Aközbek, K. Vijayalakshmi, E. Oral, C. Bowden, and S. Chin. Intensity clamping and re-focusing of intense femtosecond laser pulses in nitrogen molecular gas. *Appl. Phys. B*, 73(3): 287–290, 2001.
- [Béj08] P. Béjot, J. Kasparian, and J.-P. Wolf. Dual-color co-filamentation in Argon. *Opt. Express*, 16(18): 14115–14127, Sep 2008.
- [Bel98] M. Bellini, C. Lyngå, A. Tozzi, M. B. Gaarde, T. W. Hänsch, A. L’Huillier, and C.-G. Wahlström. Temporal Coherence of Ultrashort High-Order Harmonic Pulses. *Phys. Rev. Lett.*, 81(2): 297–300, Jul 1998.
- [Bel01] M. Bellini, C. Corsi, and M. C. Gambino. Neutral depletion and beam defocusing in harmonic generation from strongly ionized media. *Phys. Rev. A*, 64: 023411, 2001.
- [Bör10] Á. Börzsönyi, Z. Heiner, A. Kovács, M. P. Kalashnikov, and K. Osvay. Measurement of pressure dependent nonlinear refractive index of inert gases. *Opt. Exp.*, 18(25): 25847–25854, Dec 2010.
- [Bra95] A. Braun, G. Korn, X. Liu, D. Du, J. Squier, and G. Mourou. Self-channeling of high-peak-power femtosecond laser pulses in air. *Opt. Lett.*, 20(1): 73–75, Jan 1995.
- [Bra00] T. Brabec and F. Krausz. Intense few-cycle laser fields: Frontiers of nonlinear optics. *Rev. Mod. Phys.*, 72(2): 545–591, 2000.
- [Bri09] J.-P. Brichta, M. C. H. Wong, J. B. Bertrand, H.-C. Bandulet, D. M. Rayner, and V. R. Bhardwaj. Comparison and real-time monitoring of high-order harmonic generation in different sources. *Phys. Rev. A*, 79: 033404, 2009.
- [Bru08] E. Brunetti, R. Issac, and D. A. Jaroszynski. Quantum path contribution to high-order harmonic spectra. *Phys. Lett. A*, 77: 023422, 2008.
- [Cav07] A. L. Cavalieri, E. Goulielmakis, B. Horvath, W. Helml, M. Schultze, M. Fieß, V. Pervak, L. Veisz, V. S. Yakovlev, M. Uiberacker, A. Apolonski, F. Krausz, and R. Kienberger. Intense 1.5-cycle near infrared laser waveforms and their use for the generation of ultra-broadband soft-x-ray harmonic continua. *New J. Phys.*, 9: 242, 2007.

- [Cha06] H. S. Chakraborty, M. B. Gaarde, and A. Couairon. Single attosecond pulses from high harmonics driven by self-compressed filaments. *Opt. Lett.*, 31(24): 3662, 2006.
- [Chi64] R. Y. Chiao, E. Garmire, and C. H. Townes. Self-Trapping of Optical Beams. *Phys. Rev. Lett.*, 13(15): 479–482, Oct 1964.
- [Con99] E. Constant, D. Garzella, P. Breger, E. Mevel, C. Dorrer, C. Le Blanc, F. Salin, and P. Agostini. Optimizing High Harmonic Generation in Absorbing Gases: Model and Experiment. *Phys. Rev. Lett.*, 82(8): 1668, 1999.
- [Cor93] P. B. Corkum. Plasma Perspective on Strong-Field Multiphoton Ionization. *Phys. Rev. Lett.*, 71(13): 1994–1997, 1993.
- [Cou05] A. Couairon, M. Franco, A. Mysyrowicz, J. Biegert, and U. Keller. Pulse self-compression to the single-cycle limit by filamentation in a gas with a pressure gradient. *Opt. Lett.*, 30(19): 2657–2659, Oct 2005.
- [Cou06] A. Couairon, J. Biegert, C. P. Hauri, W. Kornelis, F. W. Helbing, U. Keller, and A. Mysyrowicz. Self-compression of ultra-short laser pulses down to one optical cycle by filamentation. *J. Mod. Opt.*, 53(1): 75–85, 2006.
- [Cou07] A. Couairon and A. Mysyrowicz. Femtosecond filamentation in transparent media. *Physics Reports*, 441(2-4): 47 – 189, 2007.
- [Cou08] A. Couairon, H. S. Chakraborty, and M. B. Gaarde. From single-cycle self-compressed filaments to isolated attosecond pulses in noble gases. *Phys. Rev. A*, 77: 053814, 2008.
- [Eck08] P. Eckle, A. N. Pfeiffer, C. Cirelli, A. Staudte, R. Dörner, H. G. Muller, M. Büttiker, and U. Keller. Attosecond Ionization and Tunneling Delay Time Measurements in Helium. *Science*, 322(5907): 1525–1529, 2008.
- [Ede04] J. Eden. High-order harmonic generation and other intense optical field-matter interactions: review of recent experimental and theoretical advances. *Prog. Quant. Electron.*, 28: 197–246, 2004.
- [Fan02] Z. Fangchuan, L. Zhong, Z. Zhinan, Z. Zhengquan, L. Ruxin, and X. Zhizhan. Spectral splitting of high-order harmonic emissions from ionizing gases. *Phys. Rev. A*, 65: 033808, 2002.
- [Fer88] M. Ferray, A. L’Huillier, X. F. Li, L. A. Lompre, G. Mainfray, and C. Manus. Multiple-harmonic conversion of 1064 nm radiation in rare gases. *J. Phys. B: At. Mol. Opt. Phys.*, 21(3): L31–L35, Feb 14 1988.

- [Gaa99] M. B. Gaarde, F. Salin, E. Constant, P. Balcou, K. J. Schafer, K. C. Kulander, and A. L’Huillier. Spatiotemporal separation of high harmonic radiation into two quantum path components. *Phys. Rev. A*, 59(2): 1367–1373, Feb 1999.
- [Gaa02] M. B. Gaarde and K. J. Schafer. Quantum path distributions for high-order harmonics in rare gas atoms. *Phys. Rev. A*, 65(3): 031406, Mar 2002.
- [Gaa08] M. B. Gaarde, J. L. Tate, and K. J. Schafer. Macroscopic aspects of attosecond pulse generation. *J. Phys. B: At. Mol. Opt. Phys.*, 41: 132001, 2008.
- [Gaa09] M. Gaarde and A. Couairon. Intensity Spikes in Laser Filamentation: Diagnostics and Application. *Phys. Rev. Lett.*, 103: 043901, 2009.
- [Gaa11] M. B. Gaarde, C. Buth, J. L. Tate, and K. J. Schafer. Transient absorption and reshaping of ultrafast XUV light by laser-dressed helium. *Phys. Rev. A*, 83(1): 013419, Jan 2011.
- [Gei10] Y. Geints and A. Zemlyanov. Self-focusing of a focused femtosecond laser pulse in air. *Appl. Phys. B*, 101: 735–742, 2010.
- [Goh05] C. Gohle, T. Udem, M. Herrmann, J. Rauschenberger, R. Holzwarth, H. A. Schuessler, F. Krausz, and T. W. Hänsch. A frequency comb in the extreme ultraviolet. *Nature*, 436: 234–237, 2005.
- [Gou08] E. Goulielmakis, M. Schultze, M. Hofstetter, V. S. Yakovlev, J. Gagnon, M. Uiberacker, A. L. Aquila, E. M. Gullikson, D. T. Attwood, R. Kienberger, F. Krausz, and U. Kleineberg. Single-Cycle Nonlinear Optics. *Science*, 320: 1614, 2008.
- [Hau04] C. P. Hauri, W. Kornelis, F. W. Helbing, A. Couairon, A. Mysyrowicz, J. Biegert, and U. Keller. Generation of intense carrier-envelope phase-locked few-cycle laser pulses through filamentation. *Appl. Phys. B*, 79: 673–677, 2004.
- [Hen93] B. Henke, E. Gullikson, and J. Davis. X-ray interactions: photoabsorption, scattering, transmission, and reflection at $E=50\text{--}30000$ eV, $Z=1\text{--}92$. *Atomic Data and Nuclear Data Tables*, 54(2): 181 – 342, July 1993.
- [Hen01] M. Hentschel, R. Kienberger, C. Spielmann, G. A. Reider, N. Milosevic, T. Brabec, P. Corkum, U. Heinzmann, and M. Drescher. Attosecond metrology. *Nature*, 414: 509–513, 2001.

- [Her02] J.-F. Hergott, M. Kovacev, H. Merdji, C. Hubert, Y. Mairesse, E. Jean, P. Breger, P. Agostini, B. Carré, and P. Salières. Extreme-ultraviolet high-order harmonic pulses in the microjoule range. *Phys. Rev. A*, 66: 021801(R), 2002.
- [Hol75] J. H. Holland. *Adaptation in Natural and Artificial Systems*. University of Michigan Press, Ann Arbor, 1975.
- [Iac98] C. Iaconis and I. Walmsley. Spectral phase interferometry for direct electric-field reconstruction of ultrashort optical pulses. *Opt. Lett.*, 23(10): 792–794, May 1998.
- [Ilk92] F. A. Ilkov, J. E. Decker, and S. L. Chin. Ionization of atoms in the tunnelling regime with experimental evidence using Hg atoms. *J. Phys. B: At. Mol. Opt. Phys.*, 25(19): 4005, 1992.
- [Ita04] J. Itatani, J. Levesque, D. Zeidler, H. Niikura, H. Pépin, J. C. Kieffer, P. B. Corkum, and D. M. Villeneuve. Tomographic imaging of molecular orbitals. *Nature*, 432(7019): 867–871, 2004.
- [Kan95] C. Kan, C. E. Capjack, R. Rankin, and N. H. Burnett. Spectral and temporal structure in high harmonic emission from ionizing atomic gases. *Phys. Rev. A*, 52(6): R4336, 1995.
- [Kär01] F. X. Kärtner, U. Morgner, R. Ell, T. Schibli, J. G. Fujimoto, E. P. Ippen, V. Scheuer, G. Angelow, and T. Tschudi. Ultrabroadband double-chirped mirror pairs for generation of octave spectra. *J. Opt. Soc. Am. B*, 18: 882–885, 2001.
- [Kaz02] S. Kazamias, F. Weihe, D. Douillet, C. Valentin, T. Planchon, S. Sebban, G. Grillon, F. Audebert, D. Hulin, and P. Balcou. High order harmonic generation optimization with an apertured laser beam. *Eur. Phys. J. D*, 21(3): 353–359, Dec 2002.
- [Kel65] L. V. Keldysh. Ionization in the field of a strong electromagnetic wave. *Sov. Phys. JETP*, 20: 1307–1314, 1965.
- [Kra92] J. L. Krause, K. J. Schafer, and K. C. Kulander. High-Order Harmonic Generation from Atoms and Ions in the High Intensity Regime. *Phys. Rev. Lett.*, 68(24): 3535–3538, 1992.
- [Kra09] F. Krausz and M. Ivanov. Attosecond physics. *Rev. Mod. Phys.*, 81(1): 163–234, Feb 2009.
- [Kre11] M. Kretschmar. Elektronentrajektorien bei der Erzeugung hoher harmonischer Strahlung. Master’s thesis, University of Hanover, Institute of Quantum Optics, 2011.

- [Lan98] H. R. Lange, A. Chiron, J.-F. Ripoche, A. Mysyrowicz, P. Breger, and P. Agostini. High-Order Harmonic Generation and Quasiphase Matching in Xenon Using Self-Guided Femtosecond Pulses. *Phys. Rev. Lett.*, 81(8): 1611–1613, Aug 1998.
- [Lee09] J.-H. Lee, Y. Lee, J. Park, J. Park, D. Kim, T. Yu, and C. Nam. Implementation of the direct locking method for long-term carrier-envelope-phase stabilization of a grating-based kHz femtosecond laser. *Applied Physics B: Lasers and Optics*, 96: 287–291, 2009.
- [Lew94] M. Lewenstein, P. Balcou, M. Y. Ivanov, A. L’Huillier, and P. B. Corkum. Theory of high-harmonic generation by low-frequency laser fields. *Phys. Rev. A*, 49(3): 2117–2132, 1994.
- [Lew95] M. Lewenstein, P. Salières, and A. L’Huillier. Phase of the atomic polarization in high-order harmonic generation. *Phys. Rev. A*, 52(6): 4747–4754, 1995.
- [L’H90] A. L’Huillier, X. F. Li, and L. A. Lompre. Propagation effects in high-order harmonic generation in rare gases. *J. Opt. Soc. Am. B*, 7: 527, 1990.
- [L’H91] A. L’Huillier, K. H. Schafer, and K. C. Kulander. Theoretical aspects of intense field harmonic generation. *J. Phys. B: At. Mol. Opt. Phys.*, 24: 3315–3341, 1991.
- [L’H92] A. L’Huillier, P. Balcou, S. Candel, K. J. Schafer, and K. C. Kulander. Calculations of high-order harmonic-generation processes in xenon at 1064 nm. *Phys. Rev. A*, 46(5): 2778–2790, 1992.
- [L’H93] A. L’Huillier, M. Lewenstein, P. Salieres, P. Balcou, M. Y. Ivanov, J. Larsson, and C. Wahlström. High-order harmonic-generation cutoff. *Phys. Rev. A*, 48: R3433, 1993.
- [L’H03] A. L’Huillier, D. Descamps, A. J. A, J. Norin, J. Mauritsson, and C.-G. Wahlström. Applications of high-order harmonics. *Eur. Phys. J. D*, 26(1): 91–98, 2003.
- [Li08] W. Li, X. Zhou, R. Lock, S. Patchkovskii, A. Stolow, H. C. Kapteyn, and M. M. Murnane. Time-Resolved Dynamics in N₂O₄ Probed Using High Harmonic Generation. *Science*, 322(5905): 1207–1211, 2008.
- [Lyn99] C. Lyngå, M. B. Gaarde, C. Delfin, M. Bellini, T. W. Hänsch, A. L’Huillier, and C.-G. Wahlström. Temporal coherence of high-order harmonics. *Phys. Rev. A*, 60(6): 4823–4830, Dec 1999.

- [Mai03] Y. Mairesse, A. de Bohan, L. J. Frasinski, H. Merdji, L. C. Dinu, P. Monchicourt, P. Breger, M. Kovacev, R. T. B. Carre, H. G. Muller, P. Agostini, and P. Salieres. Attosecond Synchronization of High-Harmonic Soft X-rays. *Science*, 302: 1540, 2003.
- [Mai05] Y. Mairesse and F. Quéré. Frequency-resolved optical gating for complete reconstruction of attosecond bursts. *Phys. Rev. A*, 71(1): 011401, Jan 2005.
- [Mar75] J. Marburger. Self-focusing: Theory. *Prog. Quant. Electr.*, 4(Part 1): 35 – 110, 1975.
- [Mar87] O. Martinez. 3000 times grating compressor with positive group velocity dispersion: Application to fiber compensation in 1.3-1.6 μm region. *IEEE J. Quantum. Electron.*, 23(1): 59 – 64, Jan 1987.
- [Mar10] W. Martin, A. Musgrove, S. Kotochigova, and J. Sansonetti. Ground Levels and Ionization Energies for the Neutral Atoms. National Institute of Standards and Technology (NIST), July 2010.
- [Mas08] H. Mashiko, S. Gilbertson, C. Li, S. D. Khan, M. M. Shakya, E. Moon, and Z. Chang. Double Optical Gating of High-Order Harmonic Generation with Carrier-Envelope Phase Stabilized Lasers. *Phys. Rev. Lett.*, 100: 103906, 2008.
- [McP87] A. McPherson, G. Gibson, H. Jara, U. Johann, T. S. Luk, I. A. McIntyre, K. Boyer, and C. K. Rhodes. Studies of multiphoton production of vacuum-ultraviolet radiation in the rare gases. *J. Opt. Soc. Am. B*, 4(4): 595–601, 1987.
- [Méc04] G. Méchain, A. Couairon, Y.-B. André, C. D’Amico, M. Franco, B. Prade, S. Tzortzakis, A. Mysyrowicz, and R. Sauerbrey. Long-range self-channeling of infrared laser pulses in air: a new propagation regime without ionization. *Appl. Phys. B*, 79: 379–382, 2004.
- [Mle98] M. Mlejnek, E. M. Wright, and J. V. Moloney. Dynamic spatial replenishment of femtosecond pulses propagating in air. *Opt. Lett.*, 23(5): 382–384, Mar 1998.
- [Mon92] P. Monot, T. Auguste, L. A. Lompré, G. Mainfray, and C. Manus. Focusing limits of a terawatt laser in an underdense plasma. *J. Opt. Soc. Am. B*, 9(9): 1579–1584, 1992.
- [Mul02] H. Muller. Reconstruction of attosecond harmonic beating by interference of two-photon transitions. *Appl. Phys. B: Lasers Opt.*, 74: s17–s21, 2002.

- [Nam59a] T. Namioka. Theory of the Concave Grating. *J. Opt. Soc. Am.*, 49(5): 446–460, May 1959a.
- [Nam59b] T. Namioka. Theory of the Concave Grating. II. Application of the Theory to the Off—Plane Eagle Mounting in a Vacuum Spectrograph. *J. Opt. Soc. Am.*, 49(5): 460–465, May 1959b.
- [Nam59c] T. Namioka. Theory of the Concave Grating. III. Seya-Namioka Monochromator. *J. Opt. Soc. Am.*, 49(10): 951–959, Oct 1959c.
- [Nib96] E. T. J. Nibbering, P. F. Curley, G. Grillon, B. S. Prade, M. A. Franco, F. Salin, and A. Mysyrowicz. Conical emission from self-guided femtosecond pulses in air. *Opt. Lett.*, 21: 62–65, 1996.
- [Nis97] M. Nisoli, S. de Silvestri, O. Svelto, R. Szipöecs, K. Ferencz, C. Spielmann, S. Sartania, and F. Krausz. Compression of high-energy laser pulses below 5 fs. *Opt. Lett.*, 22: 522–524, 1997.
- [Pan89] L. Pan, K. T. Taylor, and C. W. Clark. High-harmonic generation in hydrogenic ions. *Phys. Rev. A*, 39(9): 4894–4897, May 1989.
- [Pap01] N. Papadogiannis, C. Kalpouzou, E. Goulielmakis, G. Nersisyan, D. Charalambidis, F. Augé, F. Weihe, and P. Balcou. Kilohertz extreme-ultraviolet light source based on femtosecond high-order harmonic generation from noble gases. *Appl. Phys. B*, 73: 687–692, 2001.
- [Pau01] P. M. Paul, E. S. Toma, P. Breger, G. Mullot, F. Augé, P. Balcou, H. G. Muller, and P. Agostini. Observation of a Train of Attosecond Pulses from High Harmonic Generation. *Science*, 292(5522): 1689–1692, 2001.
- [Pea04] J. Peatross, J. R. Miller, K. R. Smith, S. E. Rhynard, and B. W. Pratt. Phase matching of high-order harmonic generation in helium- and neon-filled gas cells. *J. Mod. Opt.*, 51(16): 2675–2683, 2004.
- [Per07] V. Pervak, A. Tikhonravov, M. Trubetskov, S. Naumov, F. Krausz, and A. Apolonski. 1.5-octave chirped mirror for pulse compression down to sub-3 fs. *Appl. Phys. B*, 87(1): 5–12, 2007.
- [Pfe06] T. Pfeifer, C. Spielmann, and G. Gerber. Femtosecond x-ray science. *Rep. Prog. Phys.*, 69(2): 443, 2006.
- [Pro97] M. Protopapas, C. H. Keitel, and P. L. Knight. Atomic physics with super-high intensity lasers. *Rep. Prog. Phys.*, 60(4): 389, 1997.
- [Ran91] R. Rankin, C. E. Capjack, N. H. Burnett, and P. B. Corkum. Refraction effects associated with multiphoton ionization and ultrashort-pulse laser propagation in plasma waveguides. *Opt. Lett.*, 16(11): 835–837, 1991.

- [Rob09] A. Roberts, N. Shivaram, L. Xu, and A. Sandhu. Optimization of few-cycle pulse generation: Spatial size, mode quality and focal volume effects in filamentation based pulse compression. *Opt. Exp.*, 17(26): 23894–23902, Dec 2009.
- [Sal94] P. Salières, T. Ditmire, K. S. Budil, M. D. Perry, and A. L’Huillier. Spatial profiles of high-order harmonics generated by a femtosecond Cr:LiSAF laser. *J. Phys. B: At. Mol. Opt. Phys.*, 27(9): L217, 1994.
- [Sal95] P. Salières, A. L’Huillier, and M. Lewenstein. Coherence Control of High-Order Harmonics. *Phys. Rev. Lett.*, 74(19): 3776, 1995.
- [Sal96] P. Salières, T. Ditmire, M. D. Perry, A. L’Huillier, and M. Lewenstein. Angular distributions of high-order harmonics generated by a femtosecond laser. *J. Phys. B: At. Mol. Opt. Phys.*, 29(20): 4771, 1996.
- [Sal97] P. Salières, A. L’Huillier, P. Antoine, and M. Lewenstein. Study of the spatial and temporal coherence of high order harmonics. *arXiv:quant-ph*, 9710060v1, 1997.
- [Sal98] P. Salières, P. Antoine, A. de Bohan, and M. Lewenstein. Temporal and Spectral Tailoring of High-Order Harmonics. *Phys. Rev. Lett.*, 81(25): 5544–5547, Dec 1998.
- [San06b] G. Sansone, E. Benedetti, F. Calegari, C. Vozzi, L. Avaldi, R. Flammini, L. Poletto, P. Villoresi, C. Altucci, R. Velotta, S. Stagira, S. D. Silvestri, and M. Nisoli. Isolated Single-Cycle Attosecond Pulses. *Science*, 314(5798): 443–446, 2006b.
- [San06a] A. S. Sandhu, E. Gagnon, A. Paul, I. Thomann, A. Lytle, T. Keep, M. M. Murnane, H. C. Kapteyn, and I. P. Christov. Generation of sub-optical-cycle, carrier-envelope-phase-insensitive, extreme-uv pulses via nonlinear stabilization in a waveguide. *Phys. Rev. A*, 74: 061803, 2006a.
- [Sch07] M. Schultze, E. Goulielmakis, M. Uiberacker, M. Hofstetter, J. Kim, D. Kim, F. Krausz, and U. Kleineberg. Powerful 170-attosecond XUV pulses generated with few-cycle laser pulses and broadband multilayer optics. *New J. Phys.*, 9: 243, 2007.
- [Sch09b] E. Schulz, T. Binhammer, D. S. Steingrube, S. Rausch, M. Kovačev, and U. Morgner. Intense few-cycle laser pulses from self-compression in a self-guiding filament. *Appl. Phys. B*, 95: 269–272, 2009b.
- [Sch09a] N. Scharnhorst. Strahlcharakterisierung eines Hochleistungslasersystems. Bachelor thesis, Universität Hannover, 2009a.

- [Sch11] E. Schulz, D. S. Steingrube, T. Binhammer, M. B. Gaarde, A. Couairon, U. Morgner, and M. Kovačev. Tracking spectral shapes and temporal dynamics along a femtosecond filament. *Phys. Rev. A*, 2011. submitted.
- [Scr06] A. Scrinzi, M. Y. Ivanov, R. Kienberger, and D. M. Villeneuve. Attosecond physics. *J. Phys. B: At. Mol. Opt. Phys.*, 39: R1–R37, 2006.
- [She71] Y. R. Shen and M. M. T. Loy. Theoretical Interpretation of Small-Scale Filaments of Light Originating from Moving Focal Spots. *Phys. Rev. A*, 3(6): 2099–2105, Jun 1971.
- [Shi99] H. J. Shin, D. G. Lee, Y. H. Cha, K. H. Hong, and C. H. Nam. Generation of Nonadiabatic Blueshift of High Harmonics in an Intense Femtosecond Laser Field. *Phys. Rev. Lett.*, 83(13): 2544–2547, 1999.
- [Sol06] I. J. Sola, E. Mevel, L. Elouga, E. Constant, V. Strelkov, L. Poletto, P. Villoresi, E. Benedetti, J. P. Caumes, S. Stagira, C. Vozzi, G. Sansone, and M. Nisoli. Controlling attosecond electron dynamics by phase-stabilized polarization gating. *Nat. Phys.*, 2(5): 319–322, 2006.
- [Sta07] A. Staudte, D. Pavičić, S. Chelkowski, D. Zeidler, M. Meckel, H. Niikura, M. Schöffler, S. Schössler, B. Ulrich, P. P. Rajeev, T. Weber, T. Jahnke, D. M. Villeneuve, A. D. Bandrauk, C. L. Cocke, P. B. Corkum, and R. Dörner. Attosecond Strobing of Two-Surface Population Dynamics in Dissociating H_2^+ . *Phys. Rev. Lett.*, 98(7): 073003, Feb 2007.
- [Ste09a] D. S. Steingrube, E. Schulz, T. Binhammer, T. Vockerodt, U. Morgner, and M. Kovačev. Generation of high-order harmonics with ultra-short pulses from filamentation. *Opt. Exp.*, 17(18): 16177–16182, 2009a.
- [Ste09b] D. S. Steingrube, T. Vockerodt, E. Schulz, U. Morgner, and M. Kovačev. Phase-matching of high-order harmonics in a semi-infinite gas cell. *Phys. Rev. A*, 80: 043819, 2009b.
- [Ste11] D. S. Steingrube, E. Schulz, T. Binhammer, M. B. Gaarde, A. Couairon, U. Morgner, and M. Kovačev. High-order harmonic generation directly from a filament. *New J. Phys.*, 13(4): 043022, 2011.
- [Str85] D. Strickland and G. Mourou. Compression of amplified chirped optical pulses. *Opt. Commun.*, 55(6): 447 – 449, 1985.
- [Sut04] J. Sutherland, E. Christensen, N. Powers, S. Rhynard, J. Painter, and J. Peatross. High harmonic generation in a semi-infinite gas cell. *Opt. Exp.*, 12(19): 4430–4436, Sep 2004.

- [Tak02] E. Takahashi, Y. Nabekawa, T. Otsuka, M. Obara, and K. Midorikawa. Generation of highly coherent submicrojoule soft x rays by high-order harmonics. *Phys. Rev. A*, 66(2): 021802, Aug 2002.
- [Tak04] E. J. Takahashi, Y. Nabekawa, and K. Midorikawa. Low-divergence coherent soft x-ray source at 13 nm by high-order harmonics. *Appl. Phys. Lett.*, 84: 4, 2004.
- [Tei09] S. Teichmann, P. Hannaford, and L. Van Dao. Phase-matched emission of few high-harmonic orders from a helium gas cell. *Appl. Phys. Lett.*, 94(17): 171111, Apr 27 2009.
- [Tho09] I. Thomann, A. Bahabad, X. Liu, R. Trebino, M. M. Murnane, and H. C. Kapteyn. Characterizing isolated attosecond pulses from hollow-core waveguides using multi-cycle driving pulses. *Opt. Exp.*, 17: 4611, 2009.
- [Tre69] E. Treacy. Optical pulse compression with diffraction gratings. *IEEE J. Quantum. Electron.*, 5(9): 454 – 458, Sep 1969.
- [Tza07] P. Tzallas, E. Skantzakis, C. Kalpouzos, E. P. Benis, G. D. Tsakiris, and D. Charalambidis. Generation of intense continuum extreme-ultraviolet radiation by many-cycle laser fields. *Nat. Phys.*, 3: 846–850, 2007.
- [Var09] O. Varela, A. Zair, J. S. Román, B. Alonso, I. nigo Juan Sola, C. Prieto, and L. Roso. Above-millijoule super-continuum generation using polarisation dependent filamentation in atoms and molecules. *Opt. Exp.*, 17(5): 3630–3639, Mar 2009.
- [VD08] L. Van Dao, S. Teichmann, and P. Hannaford. Phase-matching for generation of few high order harmonics in a semi-infinite gas cell. *Phys. Lett. A*, 372(31): 5254–5257, Jul 28 2008.
- [Wag04] N. L. Wagner, E. A. Gibson, T. Popmintchev, I. P. Christov, M. M. Murnane, and H. C. Kapteyn. Self-Compression of Ultrashort Pulses through Ionization-Induced Spatiotemporal Reshaping. *Phys. Rev. Lett.*, 93: 173902, 2004.
- [Wah93] C.-G. Wahlström, J. Larsson, A. Persson, T. Starczewski, S. Svanberg, P. Salières, P. Balcou, and A. L’Huillier. High-order harmonic generation in rare gases with an intense short-pulse laser. *Phys. Rev. A*, 48(6): 4709–4720, 1993.
- [Wan00] Y. Wang, Y. Liu, X. Yang, and Z. Xu. Spectral splitting in high-order harmonic generation. *Phys. Rev. A*, 62: 063806, 2000.

- [Wit09] T. Wittmann, B. Horvath, W. Helml, M. G. Schatzel, X. Gu, A. L. Cavalieri, G. G. Paulus, and R. Kienberger. Single-shot carrier-envelope phase measurement of few-cycle laser pulses. *Nat. Phys.*, 5(5): 357–362, 2009.
- [Wör10] H. J. Wörner, J. B. Bertrand, D. V. Kartashov, P. B. Corkum, and D. M. Villeneuve. Following a chemical reaction using high-harmonic interferometry. *Nature*, 466(7306): 604–607, 2010.
- [Wu09] J. Wu, Y. Tong, X. Yang, H. Cai, P. Lu, H. Pan, and H. Zeng. Interaction of two parallel femtosecond filaments at different wavelengths in air. *Opt. Lett.*, 34(20): 3211–3213, Oct 2009.
- [Zai07] A. Zair, A. Guandalini, F. Schapper, M. Holler, J. Biegert, L. Gallmann, A. Couairon, M. Franco, A. Mysyrowicz, and U. Keller. Spatio-temporal characterization of few-cycle pulses obtained by filamentation. *Opt. Exp.*, 15(9): 5394–5404, Apr 2007.
- [Zho00] F. Zhong, J. Deng, X. Hu, Z. Li, Z. Zhang, and Z. Xu. The effect of ionization of gases on the high harmonic splitting. *Phys. Lett. A*, 278: 35–43, 2000.

Acknowledgments

Ich möchte mich an dieser Stelle bei all denjenigen bedanken, die mich während dieser Arbeit unterstützt haben.

Zunächst gilt mein Dank meinem Doktorvater Uwe Morgner und meinem Gruppenleiter Milutin Kovačev für Möglichkeit, dass ich meine Promotion in diesem sehr interessanten Themengebiet in ihrer Arbeitsgruppe durchführen durfte, für das Vertrauen, die Anregungen und die Unterstützung während der Arbeit und beim Schreiben der Paper.

Weiterhin möchte ich meinen Kollegen für das gute Arbeitsklima, die gute Zusammenarbeit und die interessanten Diskussionen danken. Dabei gilt mein Dank im Besonderen Emilia Schulz für die vielen gemeinsamen Stunden im Labor, die ausgiebigen Diskussionen und die gelungene Zusammenarbeit, und Thomas Binhammer für die große Hilfsbereitschaft und das immer offene Ohr. Ich danke auch meinen ehemaligen Diplomanden Tobias Vockerodt, Heiko Kurz und Martin Kretschmar. An dieser Stelle möchte ich mich bei allen bedanken, die diese Arbeit Korrektur gelesen haben und damit zu ihrer Verbesserung beigetragen haben.

Neben allen Kollegen aus der Arbeitsgruppe Morgner, möchte ich mich beim Sekretariat und der Werkstatt bedanken. Des Weiteren gilt mein Dank dem Exzellenzcluster QUEST für die finanzielle Unterstützung.

Mein Dank geht auch an Mette B. Gaarde und Arnaud Couairon für die theoretische Unterstützung und die intensive Zusammenarbeit beim Schreiben des entsprechenden Manuskripts. Manfred Lein möchte ich für die Diskussionen zu den Elektronentrajektorien und meinen Simulationen und für die Übernahme des Zweitgutachtens danken. Prof. Dr. Michael Oestreich danke ich für die Übernahme des Prüfungsvorsitz.

Nicht zuletzt danke ich meiner lieben Frau Silke, meinen Eltern, Christiane und Andreas, und meiner restlichen Familie, die mich während meines Studiums und meiner gesamten Promotion unterstützt haben.

Vielen Dank!

ACKNOWLEDGMENTS

Curriculum Vitae

Name: Daniel Sebastian Steingrube
E-Mail: steingrube@iqa.uni-hannover.de
Geburtsdatum: 27. 06. 1982
Geburtsort: Göttingen
Staatsangehörigkeit: deutsch
Familienstand: verheiratet

Schulische Ausbildung:

1988-1992	Grundschule Lenglern	Bovenden-Lenglern
1992-1994	Orientierungsstufe Bovenden	Bovenden
1994-2001	Otto-Hahn-Gymnasium Abitur (1.5)	Göttingen

Zivildienst

Sep. 2001 - Jun. 2002	Christopherus-Schule	Göttingen
--------------------------	-----------------------------	------------------

Hochschulausbildung

Okt. 2002 - Sep. 2007	Georg-August-Universität Studium mit Abschluss Diplom in Physik (mit Auszeichnung)	Göttingen
Jun 2006 - Jul 2007	Bernstein Center for Computational Neuroscience Diplomarbeit in Physik in der Gruppe von Prof. Florentin Wörgötter: <i>Investigation of collective properties in adaptive systems with many elements.</i>	Göttingen

Praktika

Feb 1999	LMS Skalar Instruments GmbH Schulpraktikum in der Software-Entwicklung.	Göttingen
----------	-----------------------------------------------------------------------------------	------------------

CURRICULUM VITAE

Aug 2001	Lambda Physik AG	Göttingen
	Praktikum in der Entwicklung und Forschung von Lithographie-Lasern. Entwicklung von Software.	
Jun 2002	Laser Laboratorium Göttingen e.V. (LLG)	Göttingen
	Entwicklung von Software für Kalorimetrie von optischen Komponenten.	
Jul 2002	Sartorius AG	Göttingen
	Praktikum in der Entwicklung und Forschung von Feuchtemesstechnik.	
Sep 2004 - Feb 2005	Coherent Inc.	Santa Clara, California, USA
	Praktikum in der Entwicklung und Forschung. Entwicklung von kleinen optisch gepumpten Hochleistungs-Halbleiterlasern.	
Beruflicher Werdegang		
Nov 2002 - Jan 2004	Abies IT GmbH	Göttingen
	Entwicklung von Verwaltungssoftware für Golf-Plätze.	
Seit Nov 2007	Institut für Quantenoptik und QUEST	Hannover
	Wissenschaftlicher Mitarbeiter Promotion: <i>High-order harmonic generation with ultra-short pulses from filamentation.</i>	

Publications

Scientific Publications

1. Hunziker, L.E.; Ihli, C.; Steingrube, D.S.; Reed, E. and Hodgson, N.
Size-scaling of TEM00 mode optically-pumped semiconductor lasers
Solid State Lasers XV: Technology and Devices **6100**, 610001 (2006)
2. Hunziker, L.E.; Ihli, C. and Steingrube, D.S.
Miniaturization and Power Scaling of Fundamental Mode Optically Pumped Semiconductor Lasers
IEEE J. Sel. Topics in Quantum Electron. **13**, 610-618 (2007)
3. Schulz, E.; Binhammer, T.; Steingrube, D.S.; Rausch, S.; Kovačev, M. and Morgner, U.
Intense few-cycle laser pulses from self-compression in a self-guiding filament
Appl. Phys. B: Lasers Opt. **95**, 269-272 (2009)
4. Steingrube, D.S.; Vockerodt, T.; Schulz, E.; Morgner, U. and Kovačev, M.
Phase matching of high-order harmonics in a semi-infinite gas cell
Physical Review A **80**, 043819 (2009)
5. Steingrube, D.S.; Vockerodt, T.; Morgner, U. and Kovačev, M.
Phase-matching high-order harmonics in a semi-infinite gas cell geometry
Proc. Lasers and Electro-Optics 2009 and the European Quantum Electronics Conference, 1 (2009)
6. Steingrube, D.S.; Schulz, E.; Binhammer, T.; Vockerodt, T.; Morgner, U. and Kovačev, M.
Generation of high-order harmonics with ultra-short pulses from filamentation
Optics Express **17**, 16177-16182 (2009)
7. Steingrube, S.; Steingrube, D.S.; Brendel, R. and Altermatt, P.P.
Comprehensive model for recombination at a-Si:H/c-Si interfaces based on amphoteric defects
physica status solidi (c) **7**, 276-279 (2010)

8. Steingrube, S.; Altermatt, P.P.; Steingrube, D.S.; Schmidt, J. and Brendel, R.
Interpretation of recombination at c-Si/SiNx interfaces by surface damage
Journal of Applied Physics **108**, 014506 (2010)
9. Steingrube, D.S.; Schulz, E.; Binhammer, T.; Vockerodt, T.; Morgner, U. and Kovačev, M.
High-Order Harmonic Generation by Few-Cycle Pulses from Filamentation
International Conference on Ultrafast Phenomena, OSA Technical Digest (CD) (2010), paper ThE26.
10. Palmer, G.; Schultze, M.; Emons, M.; Lindemann, A.L.; Pospiech, M.; Steingrube, D.; Lederer, M. and Morgner, U.
12 MW peak power from a two-crystal Yb:KYW chirped-pulse oscillator with cavity-dumping
Optics Express **18**, 19095-19100 (2010)
11. Steingrube, D.S.; Schulz, E.; Binhammer, T.; Gaarde, M.B.; Couairon, A.; Morgner, U. and Kovačev, M.
High-order harmonic generation directly from a filament
New Journal of Physics **13**, 043022 (2011)
12. Schulz, E.; Steingrube, D.S.; Vockerodt, T.; Binhammer, T.; Morgner, U. and Kovačev, M.
Efficient on-axis third harmonic generation in a light filament
CLEO/Europe and EQEC 2011 Conference Digest, OSA Technical Digest (CD) (Optical Society of America, 2011), paper CG2_4.
13. Winkler, C.; Steingrube, D.S.; Altermann, W.; Schlaf, G.; Max, D.; Kewitz, S.; Emmer, A.; Kornhuber, M.; Banning-Eichenseer, U. and Staeger, M.S.
Hodgkin's lymphoma RNA-transfected dendritic cells induce cancer/testis antigen specific immune responses
Haematologica, *submitted* (2011)
14. Schulz, E.; Steingrube, D.S.; Binhammer, T.; Gaarde, M.B.; Couairon, A.; Morgner, U. and Kovačev, M.
Tracking spectral shapes and temporal dynamics along a femtosecond filament
Physical Review A, *submitted* (2011)

Contributions at international conferences

1. Conference on Solid State Lasers XV, 2006, San Jose, CA, USA
Oral: *Size-scaling of TEM00 mode optically-pumped semiconductor lasers*
Hunziker, L.E.; Ihli, C.; Steingrube, D.S.; Reed, E. and Hodgson, N.

2. International Symposium on Filamentation (COFIL), 2008, Paris, France
Poster: *Shortening of intense laser pulses by self-compression in a filament*
Schulz, E.; Binhammer, T.; Rausch, S.; Steingrube, D.S.; Kovačev, M. and Morgner, U.
3. International Conference on Multiphoton Processes (ICOMP), 2008, Heidelberg, Germany
Poster: *Enhancement of high-order harmonic generation by rare gas mixtures*
Steingrube, D.S.; Vockerodt, T.; Morgner, U. and Kovačev, M.
4. Conference on Lasers and Electro-Optics (CLEO), 2009, Munich, Germany
Poster: *Phase-matching high-order harmonics in a semi-infinite gas cell geometry*
Steingrube, D.S.; Vockerodt, T.; Morgner, U. and Kovačev, M.
5. International Conference on Attosecond Physics, 2009, Kansas, USA
Poster: *Generation of high-order harmonics with ultra-short pulses from filamentation*
Schulz, E.; Steingrube, D.S.; Binhammer, T.; Vockerodt, T.; Morgner, U. and Kovačev, M.
6. International Conference on Attosecond Physics, 2009, Kansas, USA
Poster: *Phase-matching of high-order harmonic generation in a semi-infinite gas cell geometry*
Steingrube, D.S.; Vockerodt, T.; Schulz, E.; Morgner, U. and Kovačev, M.
7. Advances in Strong-Field and Attosecond Physics, 2010, London, England
Poster: *Few-Cycle Pulses from a Filament Applied to High-Order Harmonic Generation*
Schulz, E.; Steingrube, D.S.; Binhammer, T.; Morgner, U. and Kovačev, M.
8. Advances in Strong-Field and Attosecond Physics, 2010, London, England
Poster: *High-Order Harmonic Generation Directly from a Filament*
Steingrube, D.S.; Schulz, E.; Binhammer, T.; Gaarde, M.B.; Couairon, A.; Morgner, U. and Kovačev, M.
9. 17th International Conference on Ultrafast Phenomena (UP), 2010, Snowmass, Colorado, USA
Poster: *High-order Harmonic Generation by Few-cycle Pulses from Filamentation*
Steingrube, D.S.; Schulz, E.; Binhammer, T.; Vockerodt, T.; Morgner, U. and Kovačev, M.
10. International Symposium on Filamentation (COFIL), 2010, Crete, Greece
Poster: *Few-cycle pulses from filamentation applied to high-order harmonic generation*
Steingrube, D.S.; Schulz, E.; Binhammer, T.; Vockerodt, T.; Morgner, U. and Kovačev, M.

11. International Symposium on Filamentation (COFIL), 2010, Crete, Greek
Poster: *Lateral investigation of a filament*
Steingrube, D.S.; Schulz, E.; Binhammer, T.; Morgner, U. and Kovačev, M.
12. Gordon Research Conference on Multiphoton Processes (MP-GRC), 2010, Tilton, NH, USA
Poster: *High-order harmonic generation within a filament*
Steingrube, D.S.; Schulz, E.; Binhammer, T.; Gaarde, M.B.; Couairon, A.; Morgner, U. and Kovačev, M.
13. Conference on Lasers and Electro-Optics (CLEO), 2011, Munich, Germany
Oral: *Efficient on-axis third harmonic generation in a light filament*
Schulz, E.; Steingrube, D.S.; Vockerodt, T.; Binhammer, T.; Morgner, U. and Kovačev, M.